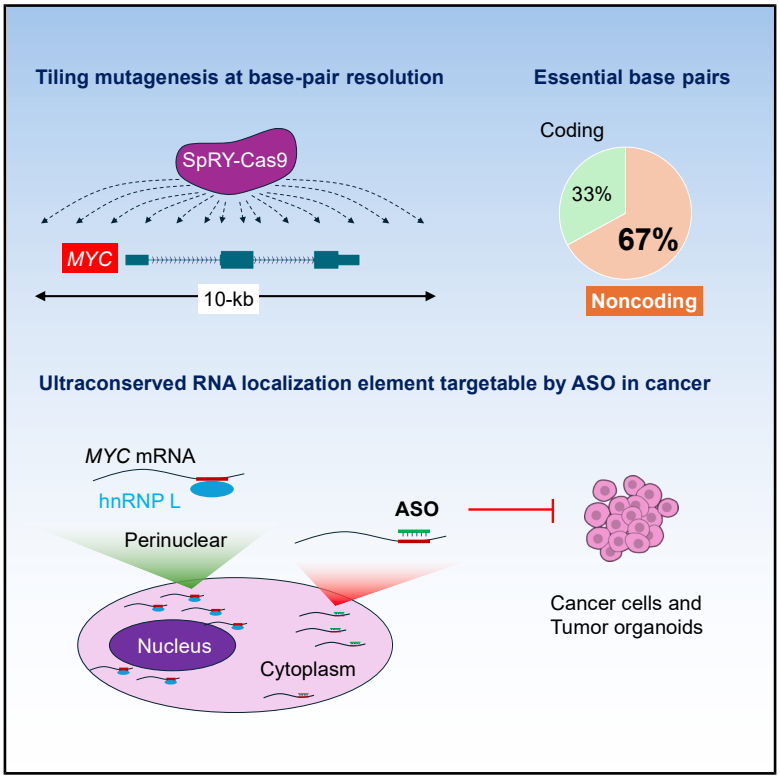
Cell

Article

CRISPR mutagenesis of the *MYC* locus reveals a druggable ultraconserved RNA element

Graphical abstract



Highlights

- CRISPR tiling mutagenesis maps the fitness landscape of the 10-kb *MYC* locus
- Noncoding sequences comprise 67% of the essential base pairs in the *MYC* locus
- An ultraconserved 3′ UTR element promotes MYC nuclear localization via hnRNP L
- ASOs targeting the 3′ UTR element suppress growth of MYC-addicted cancer cells

Authors

Peiguo Shi (时培果), Feiyue Yang (杨飞月), Tala FNU (塔拉), ..., Chaolin Zhang (张朝林), Jianwen Que (阙建文), Xuebing Wu (吴雪兵)

Correspondence

ps3008@cumc.columbia.edu (P.S.), jq2240@cumc.columbia.edu (J.Q.), xuebing.wu@columbia.edu (X.W.)

In brief

CRISPR tiling mutagenesis of the 10-kb human *MYC* locus mapped the fitness landscape of an entire human gene at base-pair resolution. This unbiased interrogation revealed that 67% of functionally essential base pairs are noncoding. An ultraconserved RNA regulatory element was identified that controls MYC localization and can be therapeutically targeted to suppress cancer cell growth in patient-derived tumor organoids.

Shi et al., 2027, Cell *190*, 1–20
January 7, 2027 © 2026 Elsevier Inc. All rights are reserved, including those for text and data mining, AI training, and similar technologies.
https://doi.org/10.1016/j.cell.2026.10.002

CellPress

Please cite this article in press as: Shi et al., CRISPR mutagenesis of the *MYC* locus reveals a druggable ultraconserved RNA element, Cell (2027), https://doi.org/10.1016/j.cell.2026.10.002

Cell

CellPress

Article

CRISPR mutagenesis of the *MYC* locus reveals a druggable ultraconserved RNA element

Peiguo Shi (时培果),[1,2,3,11,*] Feiyue Yang (杨飞月),[1,2,3,11] Tala FNU (塔拉),[3,4,11] Wesley Huang (黄亦杨),[1,2,3] Linqing Xing (邢琳晴),[1,2,3] Shah Alam,[2,5,6] Wangyang Dai (代王洋),[2,5,6] Alexis O. Aparicio,[1,2,3,10] Colin H. Kalicki,[1,2,3] Aditi Trehan,[1,2,3] Michael R. Murphy,[1,2,3] Esther R. Rotlevi,[1,2,3] Prajish Iyer,[7] Lili Wang (王莉莉),[7] Sara Zaccara,[2] Muredach P. Reilly,[1] Ya Cheng Liao (廖雅成),[5,8] Chaolin Zhang (张朝林),[2,5,6] Jianwen Que (阙建文),[3,4,9,*] and Xuebing Wu (吴雪兵)[1,2,3,12,*]

[1]Division of Cardiology, Department of Medicine, Vagelos College of Physicians and Surgeons, Columbia University Irving Medical Center, New York, NY 10032, USA

[2]Department of Systems Biology, Vagelos College of Physicians and Surgeons, Columbia University Irving Medical Center, New York, NY 10032, USA

[3]Herbert Irving Comprehensive Cancer Center, Vagelos College of Physicians and Surgeons, Columbia University Irving Medical Center, New York, NY 10032, USA

[4]Columbia Center for Human Development, Department of Medicine, Vagelos College of Physicians and Surgeons, Columbia University Irving Medical Center, New York, NY 10032, USA

[5]Department of Biochemistry & Molecular Biophysics, Vagelos College of Physicians and Surgeons, Columbia University Irving Medical Center, New York, NY 10032, USA

[6]Center for Motor Neuron Biology and Disease, Vagelos College of Physicians and Surgeons, Columbia University Irving Medical Center, New York, NY 10032, USA

[7]Division of Hematology and Oncology, Department of Medicine, Vagelos College of Physicians and Surgeons, Columbia University Irving Medical Center, New York, NY 10032, USA

[8]Taub Institute for Research on Alzheimer's Disease and the Aging Brain, Vagelos College of Physicians and Surgeons, Columbia University Irving Medical Center, New York, NY 10032, USA

[9]Division of Digestive and Liver Disease, Department of Medicine, Vagelos College of Physicians and Surgeons, Columbia University Irving Medical Center, New York, NY 10032, USA

[10]Present address: Renaissance School of Medicine at Stony Brook University, Stony Brook, NY 11794, USA

[11]These authors contributed equally

[12]Lead contact

*Correspondence: ps3008@cumc.columbia.edu (P.S.), jq2240@cumc.columbia.edu (J.Q.), xuebing.wu@columbia.edu (X.W.)

https://doi.org/10.1016/j.cell.2026.10.002

SUMMARY

Noncoding sequences comprise most of the human genome; however, their functional significance remains largely elusive. Using CRISPR tiling mutagenesis with near-PAMless, high-fidelity SpRY-Cas9, we mapped the fitness landscape of an entire human gene, the 10-kb *MYC* locus, at base-pair resolution. This unbiased interrogation revealed that 67% of functionally essential base pairs are noncoding. Essential noncoding base pairs are under strong constraint in the human population but show limited evolutionary conservation across species. Within this landscape, we identified an ultraconserved noncoding RNA element in the 3′ untranslated region (UTR) that promotes perinuclear localization of *MYC* mRNA and nuclear localization of MYC protein through interaction with hnRNP L. Steric-blocking antisense oligonucleotides (ASOs) targeting this element selectively eliminate diverse MYC-dependent cancer cells and inhibit growth of patient-derived tumor organoids. Together, these findings establish noncoding sequences as major carriers of functional genetic information and identify a therapeutically actionable RNA element whose targeting disrupts MYC-driven cancer.

INTRODUCTION

The vast noncoding expanse of the human genome represents one of the greatest remaining frontiers in understanding genome function.[1] Once dismissed as inert, noncoding sequences are now recognized as key regulators of gene expression at multiple levels, serving as promoters, enhancers, and silencers at the DNA level,[2] and governing splicing, polyadenylation, subcellular localization, translation, and decay at the RNA level.[3] Yet despite these advances, a comprehensive functional annotation of the noncoding genome at base-pair resolution remains lacking. This gap limits our understanding of the fundamental design principles of the genome, including the relative contributions of coding and noncoding sequences to the functional information it encodes.[4]

All rights are reserved, including those for text and data mining, AI training, and similar technologies.

Please cite this article in press as: Shi et al., CRISPR mutagenesis of the *MYC* locus reveals a druggable ultraconserved RNA element, Cell (2027), https://doi.org/10.1016/j.cell.2026.10.002

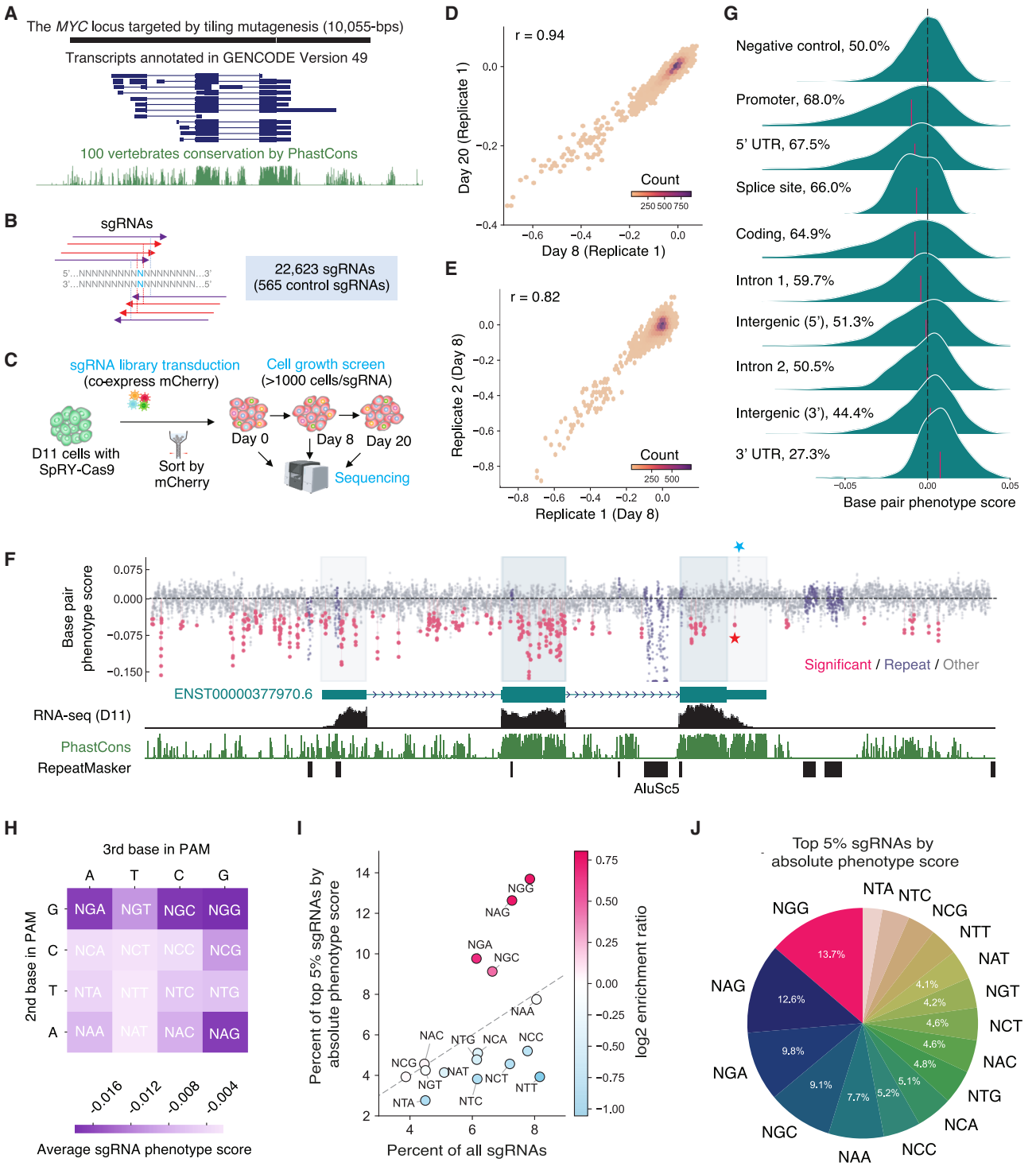


Figure 1. Mapping the fitness landscape of the *MYC* locus with CRISPR tiling mutagenesis

(A) Annotated *MYC* transcripts and conservation score across 100 vertebrate genomes.

(B) Each base pair (light blue) is targeted by eight sgRNAs (arrows) that induce Cas9 cleavage (dotted vertical lines) within ±1 bp.

(C) CRISPR tiling mutagenesis screen for cell proliferation.

(D) Scatterplot of base-pair level phenotype scores between day 8 and day 20 (replicate 1).

(E) Scatterplot of base-pair level phenotype scores between replicates (day 8 samples).

(legend continued on next page)

Please cite this article in press as: Shi et al., CRISPR mutagenesis of the *MYC* locus reveals a druggable ultraconserved RNA element, Cell (2027), https://doi.org/10.1016/j.cell.2026.10.002

Owing to their diverse mechanisms of action, noncoding sequences are far more challenging to dissect than coding sequences. Massively parallel reporter assays (MPRAs)[5] have been widely used to test the activity of individual elements at scale, including putative enhancers[6] and RNA elements regulating splicing,[7] polyadenylation,[8] stability,[9] or translation,[10] but their use of artificial reporter constructs lacks native genomic and transcript contexts and is often confounded by technical artifacts.[11,12] CRISPR-based approaches—including Cas9 tiling mutagenesis,[13–21] dCas9 tiling scans,[22–29] base editing,[19,30,31] and prime editing screens[32–34]—enable functional interrogation in endogenous genomic context[35] and have identified numerous noncoding elements, including a site in the *BCL11A* enhancer underlying the first FDA-approved CRISPR gene therapy.[21,36] However, their resolution and comprehensiveness remain limited, in part by the canonical NGG protospacer adjacent motif (PAM) requirement, which restricts targetable sites to roughly every 8–12 base pairs (bps).

MYC is a master regulator of cell proliferation and one of the most frequently dysregulated oncogenes, with aberrant expression observed in approximately 70% of cancers.[37,38] Many tumors exhibit "MYC addiction," relying on sustained MYC activity for proliferation and survival.[39,40] Despite decades of research, no approved therapy directly targeting the MYC protein exists,[41] due in part to its intrinsically disordered structure,[41] predominant nuclear localization,[42] and an incomplete understanding of its biology. A deeper characterization of MYC's regulation may therefore open new therapeutic avenues across a broad range of cancers.

Using the 10-kb *MYC* locus as a proof of principle, we conducted a base-pair resolution CRISPR tiling mutagenesis screen of an entire human protein-coding gene, enabled by a near-PAMless high-fidelity Cas9 variant (HF1-SpRY-Cas9).[43] By mapping the fitness landscape of the *MYC* locus, we seek to delineate the relative contributions of coding and noncoding sequences to MYC function and uncover regulatory elements and mechanisms that may provide new therapeutic opportunities in cancer.

RESULTS

CRISPR tiling mutagenesis screening of the *MYC* locus

To assess the phenotypic impact of each base pair within the 10,055-bp human *MYC* locus (Figure 1A), we performed a cell growth-based tiling mutagenesis screen using HF1-SpRY-Cas9 and a library of single-guide RNAs (sgRNAs) tiling both strands of the locus. Taking advantage of the near-PAMless activity of SpRY-Cas9, we designed sgRNAs for all possible 20-nt sequences, enabling each base pair to be interrogated by four sgRNAs that are expected to induce double-strand breaks immediately flanking it (red sgRNAs targeting the blue base pair in Figure 1B). In total, the library comprised 22,623 sgRNAs, including 565 negative controls.

We performed the screens in the human D11 multiple myeloma cell line, which lacks *MYC* gene amplification[44,45] and is dependent on MYC for proliferation.[46] Cells were stably integrated with HF1-SpRY-Cas9 and subsequently transduced with the sgRNA library at a low multiplicity of infection (MOI < 0.3), selected by mCherry sorting (co-expressed with sgRNAs), cultured while maintaining >1,000 cells per sgRNA, and harvested on day 8 and day 20 for sgRNA sequencing (Figure 1C). An independent biological replicate was performed starting from SpRY-Cas9 stable cell line generation. To preserve library complexity in the input (day 0) sample, we transduced cells at a high-MOI (8.7) and used this high-MOI day 0 sample as the reference for all downstream analyses (see STAR Methods).

Using model-based analysis of genome-wide CRISPR/Cas9 knockout (MAGeCK),[47] we calculated a phenotype score for each sgRNA as the $\log_2$ fold-change in abundance at days 8 or 20 relative to day 0, normalized by negative control sgRNAs (see sgRNA-level scores in Table S1). To validate the screen, we generated cell lines each stably expressing one of 12 strongly depleted sgRNAs and observed substantial indels at all target sites using amplicon sequencing (Figures S1A and S1B, corresponding oligos in Table S2). Six cell lines were further evaluated in competitive growth assays, and all exhibited reduced fitness compared with the negative control (Figure S1C). Four of six randomly selected sgRNAs targeting noncoding regions exhibited substantially higher indel frequencies than the control (Figure S1D).

Reproducible phenotypes at base-pair resolution

To quantify phenotypic effect at base-pair resolution, we applied MAGeCK's robust rank aggregation (RRA) algorithm[47] to integrate data from the eight sgRNAs predicted to cut within ±1 bp of each base pair (Figure 1B), as these guides are most likely to induce indels at that position. As in gene-based screens,[47] sgRNA aggregation mitigates variability in sgRNA efficiency, PAM compatibility, and off-target effects. Base-pair-level phenotype scores were highly correlated between day 8 and 20 samples within each replicate (Pearson correlation coefficient r = 0.94 for replicate 1, Figure 1D, r = 0.86 for replicate 2, Figure S1E). Across replicates, correlations remained strong, with r = 0.82 for day 8 samples (Figure 1E) and r = 0.74 for day 20 samples (Figure S1F). These results demonstrate the high reproducibility of our screening approach.

Given the strong agreement between replicates and time points, we combined all four samples (two replicates each with two time points) and calculated a composite phenotype score for each base pair by averaging across samples (Table S3). This analysis delineates the fitness landscape of the *MYC* locus

(F) Base-pair level phenotype scores averaged across four samples. Significant base pairs are highlighted in red and repeats in purple. Scores are truncated at the *AluSc5* repeat (see Figure S2 for the full range). Blue and red stars highlight 3′ UTR base pairs with the strongest positive and negative phenotype scores, respectively.

(G) Density plots of base-pair phenotype scores in various regions. The vertical red bar indicates median values. Also shown are the percentages of base pairs with a negative phenotype score.

(H) Average phenotype scores across four samples of all sgRNAs with the same PAM.

(I) Scatterplot showing PAM frequency for all sgRNAs (x axis) and the top 5% of sgRNAs (y axis). Color indicates log2 enrichment (y/x). Dashed line: y/x = 1.

(J) PAM frequency for top 5% sgRNAs by absolute sgRNA-level phenotype scores averaged across four samples.

Please cite this article in press as: Shi et al., CRISPR mutagenesis of the *MYC* locus reveals a druggable ultraconserved RNA element, Cell (2027), https://doi.org/10.1016/j.cell.2026.10.002

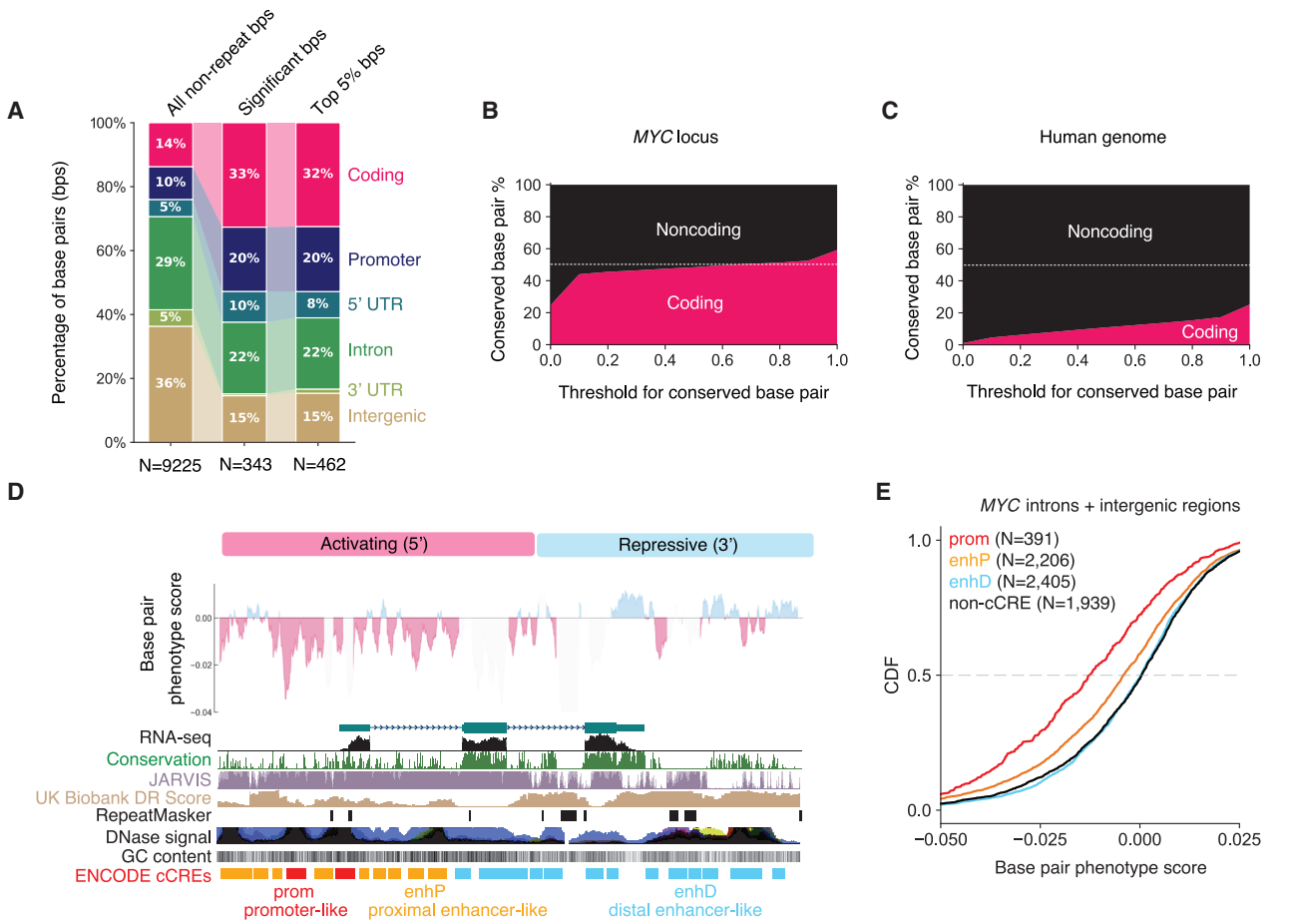


Figure 2. Noncoding regions account for the majority of functional base pairs in the *MYC* locus

(A) Distribution of base pairs (bps) in *MYC*, comparing those with significant phenotypes or within the top 5% by absolute phenotype scores to all non-repeat bps in the *MYC* locus.

(B and C) Relative percentage of coding and noncoding base pairs in *MYC* (ENST00000377970.6) (B) and the human genome (C) with conservation scores higher than a given phastCons score threshold.

(D) Phenotype scores of noncoding base pairs smoothed using a sliding window of 100 bp. Signals in coding regions (except the end of the CDS containing an RNA instability element) and repeats are masked to highlight noncoding regions. ENCODE DNase I signal range: 0–100.

(E) Cumulative distribution function (CDF) plot comparing phenotype scores of base pairs within ENCODE3 annotated cCREs (prom vs. non-cCRE: $p = 1.2 \times 10^{-19}$, enhP vs. non-cCRE: $p = 2.6 \times 10^{-10}$). The Kolmogorov-Smirnov test was used to compute the p values.

(F) CDF of conservation scores (phastCons) in 100 vertebrate species comparing significant and other noncoding base pairs.

(legend continued on next page)

Please cite this article in press as: Shi et al., CRISPR mutagenesis of the *MYC* locus reveals a druggable ultraconserved RNA element, Cell (2027), https://doi.org/10.1016/j.cell.2026.10.002

at base-pair resolution (Figure 1F). A base-pair position was considered to have a significant phenotype if it showed a false discovery rate (FDR) < 0.05 in at least two samples and exhibited a consistent directional trend in the remaining samples ($N = 343$, highlighted in red in Figure 1F).

Multiple lines of evidence support the validity of our screen. First, the strongest phenotype mapped to an intronic *Alu* repeat (Figure S2A), likely reflecting the extensive DNA double-strand breaks and nonspecific toxicity caused by targeting high-copy sequences.[48] Deletion of this *Alu* element from an 8.6-kb plasmid fragment containing the full *MYC* gene had no detectable effect on *MYC* mRNA splicing or abundance (Figures S2B–S2D). We therefore excluded *RepeatMasker*-annotated repeat regions from subsequent analyses unless otherwise noted (purple in Figure 1F), with strong correlations between time points and replicates maintained after exclusion (Figures S1G–S1J). Second, whereas targeting the promoter, 5′ UTR, splice sites, and coding region caused strong growth defects, targeting the 3′ UTR promoted cell growth (Figure 1G), consistent with the established role of the *MYC* 3′ UTR in promoting rapid mRNA degradation.[49] Third, the PAM efficiency of our screen recapitulated that reported for SpRY-Cas9,[43] with the highest activity at NGN and weaker activity at NTT and NAT (Figure 1H). Although NGG was slightly enriched among the top 5% of non-repeat sgRNAs (Figure 1I), 86.3% did not use NGG and would therefore have been missed by canonical SpCas9 (Figure 1J). Finally, observed phenotype scores significantly correlated with on-target efficiencies predicted by three widely used algorithms[50–52] (Figures S3A and S3B).

Negligible false positives linked to off-target effects

HF1-SpRY-Cas9 is a high-fidelity variant with negligible reported off-target activity.[43] In our library, 57% of non-repeat-targeting sgRNAs have no predicted off-target sites, allowing one mismatch (Figure S3C). Whereas repeat-targeting sgRNAs harbor $\sim 10^3$–10^6 predicted off-target sites and show increasing phenotypic effects with off-target burden (Figure S3D, purple), non-repeat-targeting sgRNAs generally have few predicted off-target sites, with no such relationship between phenotype and off-target counts (red, Figure S3D). This trend also holds when allowing two or three mismatches (Figures S3E–S3H). The lack of a strong phenotype in non-repeat-targeting sgRNAs with increasing numbers of off-target sites is likely explained by dilution and sequestration of Cas9 at predominantly nonessential off-target loci, coupled with reduced cleavage efficiency at mismatched sites. These analyses indicate that off-target activity, if present, is unlikely to substantially contribute to phenotypes or false positives among non-repeat-targeting sgRNAs.

Moreover, aggregating each base-pair phenotype across eight distinct sgRNAs (Figure 1B) minimizes the influence of individual off-target events, including those arising from sgRNA self-targeting.[53] We further excluded off-target contributions in subsequent mechanistic studies using targeted amplicon sequencing, complementary perturbation approaches, and rescue experiments. Finally, disruption of a neighboring gene is unlikely to explain the observed growth phenotype, as the nearest protein-coding gene is >300 kb away.

The majority of functional base pairs are noncoding

As expected, coding sequences were enriched for phenotypically impactful base pairs: although they comprise only 14% of the *MYC* locus interrogated (excluding repeats), they accounted for 33% of significant base pairs (Figure 2A), representing ~3-fold enrichment over noncoding sequences. Nevertheless, noncoding regions collectively contained the majority (67%) of functional base pairs (Figure 2A), a pattern similarly observed among the top 5% of base pairs ranked by absolute phenotypic score (Figure 2A).

These results were consistent with patterns of evolutionary conservation across 100 vertebrate species: across conservation score thresholds, ~50% of conserved *MYC* base pairs are noncoding (Figure 2B). Genome-wide, more than 70% of the most highly conserved base pairs are noncoding (Figure 2C), consistent with a previous estimate based on human-mouse sequence conservation.[4] These findings suggest that the majority of the genome's functional genetic information may be collectively encoded within noncoding sequences.

Intriguingly, noncoding sequences in the 5′ and 3′ halves of the *MYC* locus exhibited opposing phenotypic effects, as revealed by phenotype scores smoothed using a sliding window of 100-bp, excluding coding regions (Figure 2D). The 5′ half, which contains 84% of significant noncoding base pairs, was enriched for growth-suppressive perturbations (Figure 1F), indicating a role in promoting MYC expression and function. By contrast, perturbations in the 3′ half generally promoted growth (Figures 2D and 1G), although none reached statistical significance (Figure 1F). The scarcity of perturbations that significantly enhance cell growth is commonly observed for genome-wide gene loss-of-function screens.[54,55]

Notably, 79% of significant 5′ noncoding base pairs overlap ENCODE candidate *cis*-regulatory elements (cCREs)[56] bearing promoter-like (prom, 24%) or proximal enhancer-like (enhP, 54%) chromatin signatures (Figure 2D), suggesting that these sequences promote *MYC* transcription. Consistent with this, perturbations of these base pairs were more likely to reduce cell viability in our CRISPR screen (Figure 2E). Distal enhancer-like signatures, concentrated in the 3′ half (Figure 2D), showed little evidence of functional importance in this cell line (Figure 2E). Together, these findings identify the 5′ half of the *MYC* locus as a transcriptional activation hub that drives *MYC* expression.

The majority of growth-suppressing sequences (positive phenotype scores) cluster in the 3′ half of the locus, particularly within the highly conserved, AU-rich 3′ UTR that mediates rapid *MYC* mRNA degradation[49] (Figure 2D), as well as the C-terminal coding region that induces ribosome stalling and mRNA decay.[57] This includes the site with the strongest positive phenotype score across the entire locus (blue star, Figure 1F), which notably resides within the most conserved region of the 3′ UTR, the only 9-nt or longer sequence (AACTGCCTC) perfectly conserved across at least 82 consecutive vertebrate genomes in the UCSC 100-

(G) CDF of phenotype scores comparing conserved (phastCons ≥ 0.5) and non-conserved (phastCons < 0.5) noncoding base pairs.
(H) As in (G) for base pairs in the promoter.
(I) CDF of UK Biobank DR score comparing noncoding regions with and without significant CRISPR mutagenesis phenotypes.

Please cite this article in press as: Shi et al., CRISPR mutagenesis of the *MYC* locus reveals a druggable ultraconserved RNA element, Cell (2027), https://doi.org/10.1016/j.cell.2026.10.002

vertebrate alignment, up to the first mismatch (ultraconserved, Figure S4). Intriguingly, this 9-nt element contains overlapping seed matches, offset by one nucleotide, for the conserved tumor suppressor microRNAs let-7b and miR-34b (Figure S4D), both of which promote *MYC* mRNA degradation.[58–60]

Functional noncoding base pairs are constrained in humans

Unexpectedly, noncoding *MYC* base pairs with significant phenotypes were less conserved than those without significant phenotypes (Figure 2F, $p = 3.0 \times 10^{-6}$), regardless of whether conservation was evaluated using genomes of 100 vertebrates or 30 mammals (mostly primates), measured as phastCons or phyloP scores (Figure S5A). Although weak ($r = 0.12$, Figure S5B), this unexpected correlation was statistically significant ($p = 8.65 \times 10^{-29}$) and was not explained by GC content or predicted sgRNA efficiency (Figures S5C and S5D). Across the entire locus, conserved noncoding base pairs were associated with significantly weaker, rather than stronger, phenotypes (Figure 2G, $p = 2.0 \times 10^{-20}$, similar results using phyloP and different conservation thresholds in Figure S5E). This inverse relationship was most pronounced in the promoter (Figures 2H and S6) and extends to upstream and downstream 5′ UTR (Figure S5F), all enriching for transcriptional *cis*-regulatory elements (Figure 2D). These findings are consistent with the rapid evolutionary divergence of transcription factor binding sites between species[61] and the limited sequence conservation of most transcriptional *cis*-regulatory elements.[62]

The paradox highlights a key limitation of relying on cross-species sequence conservation to identify rapidly evolving functional elements in the noncoding genome. Supporting functional importance in the human lineage, base pairs exhibiting significant phenotypic effects in our tiling mutagenesis screens show markedly stronger constraint within the human population, as indicated by lower UK Biobank variant depletion rank (DR) scores[63] (Figure 2I) and higher "Junk" Annotation genome-wide Residual Variation Intolerance Score (JARVIS) values[64] (Figure S5G). However, both human constraint scores correlate only modestly with our phenotype score ($r = 0.52$ for DR and $r = -0.18$ for JARVIS, Figure S5H), highlighting the limited predictive power of constraint metrics alone and the need for unbiased, high-resolution experimental assays to resolve functional noncoding elements.

Reanalysis of a tiling mutagenesis screen targeting the promoter and 5′ UTR of the ribosomal protein gene *RPS19* in human K562 cells[19] similarly revealed reduced sequence conservation at base pairs with strong phenotypic effects (Figure S5I). Across human genes, we also observed a significant negative correlation between 3′ UTR conservation and mRNA half-life (Figure S5J), extending earlier observations limited to a few dozen mRNAs.[65,66] Together, these findings suggest that conserved 3′ UTRs broadly function as post-transcriptional repressive elements.

An ultraconserved 3′ UTR element indispensable for MYC-addicted cells

Within the largely repressive core 3′ UTR, we identified a single site essential for cell growth (red star in Figure 1F). The strongest sgRNA targeting this site, sg723, contains a GGT PAM and would have been missed by Cas9 variants with more restrictive PAMs (Figure 3A). In competitive growth assays, sg723-expressing cells were progressively depleted over 10 days when co-cultured with control cells (Figure 3B), validating the screen phenotype.

Sequencing revealed a predominant 8-nt CACAACCT deletion (Δ8) and a less frequent nested 2-nt CA deletion (Δ2), with the expected cleavage site after the first CA dinucleotide (Figure 3A). The same mutational spectrum was observed in both the wild-type (WT) (Figure 3A) and green fluorescent protein (GFP)-tagged alleles in the heterozygous D11 cells (Figure S7A) as well as the triple-negative breast cancer (TNBC) cell line MDA-MB-231 expressing WT *MYC* (Figure S7B).

Remarkably, the deleted sequence is ultraconserved, with the first 7-nt CACAACC perfectly conserved across at least 82 consecutive vertebrate genomes (Figure S4A). The let-7/miR-34 target site described earlier is the only other sequence with this level of conservation in the entire *MYC* locus. Intriguingly, these two ultraconserved sites are only 40-nt apart (red and blue stars in Figure 1F; see enlarged view in Figure S4), with the intervening sequence forming a highly conserved stem-loop structure with numerous covariations indicating strong evolutionary pressure in maintaining the RNA structure (Figures S4B and S4C).[67] The clustering of conserved sequence and structural elements with opposing phenotypic effects suggests possible combinatorial regulation.

We further derived two clonal D11 cell lines homozygous for the 8-nt CACAACCT deletion (Δ8), both of which exhibited significant growth defects (Figure 3C). To rule out the Cas9 off-target effects as a confounding factor, we cloned the entire *MYC* gene in 8.6-kb genomic DNA into a plasmid, including introns and UTRs, and generated constructs carrying either the Δ8 or Δ2 deletion identified in sg723-targeted cells (Figures 3D, S2B, and S2C). RNA sequencing (RNA-seq) confirmed the expression of *MYC* transcripts from the plasmid with splicing and polyadenylation patterns and efficiency similar to the endogenous transcript (Figure S2C). When transfected in HEK293T cells, only the WT construct significantly promoted cell growth, whereas neither mutant did so (Figure 3D), directly validating the essential role of the ultraconserved element.

To assess potential off-target effects of sg723, we used Cas-OFFinder[68] to predict genome-wide candidate off-target sites, identifying two with one mismatch and 13 with two mismatches (Table S4). Only one two-mismatch site overlapped a DepMap essential gene, *PIK3R5*, which is essential in ~1% of CRISPR screens. Targeted sequencing of the 12 highest-confidence sites, including *PIK3R5*, detected no mutations in SpRY-Cas9/sg723-expressing cells (Figure S8), indicating minimal off-target activity and supporting that the proliferation defects result from disruption of the targeted *MYC* 3′ UTR element.

To further exclude sg723-specific effects, we tested another sgRNA (sg1039) targeting the same element, which similarly caused a significant growth defect in a competitive cell proliferation assay (Figure S7C). Furthermore, adenine base editing with three independent sgRNAs targeting the element likewise significantly impaired cell growth (Figure S7D).

Together, these convergent observations from bulk-mutated populations, clonal cell lines, plasmid-expressed mutants, distinct sgRNAs, and complementary editing approaches validate the screen results and demonstrate that a highly conserved element within the *MYC* 3′ UTR is functionally required to promote cell proliferation.

Please cite this article in press as: Shi et al., CRISPR mutagenesis of the *MYC* locus reveals a druggable ultraconserved RNA element, Cell (2027), https://doi.org/10.1016/j.cell.2026.10.002

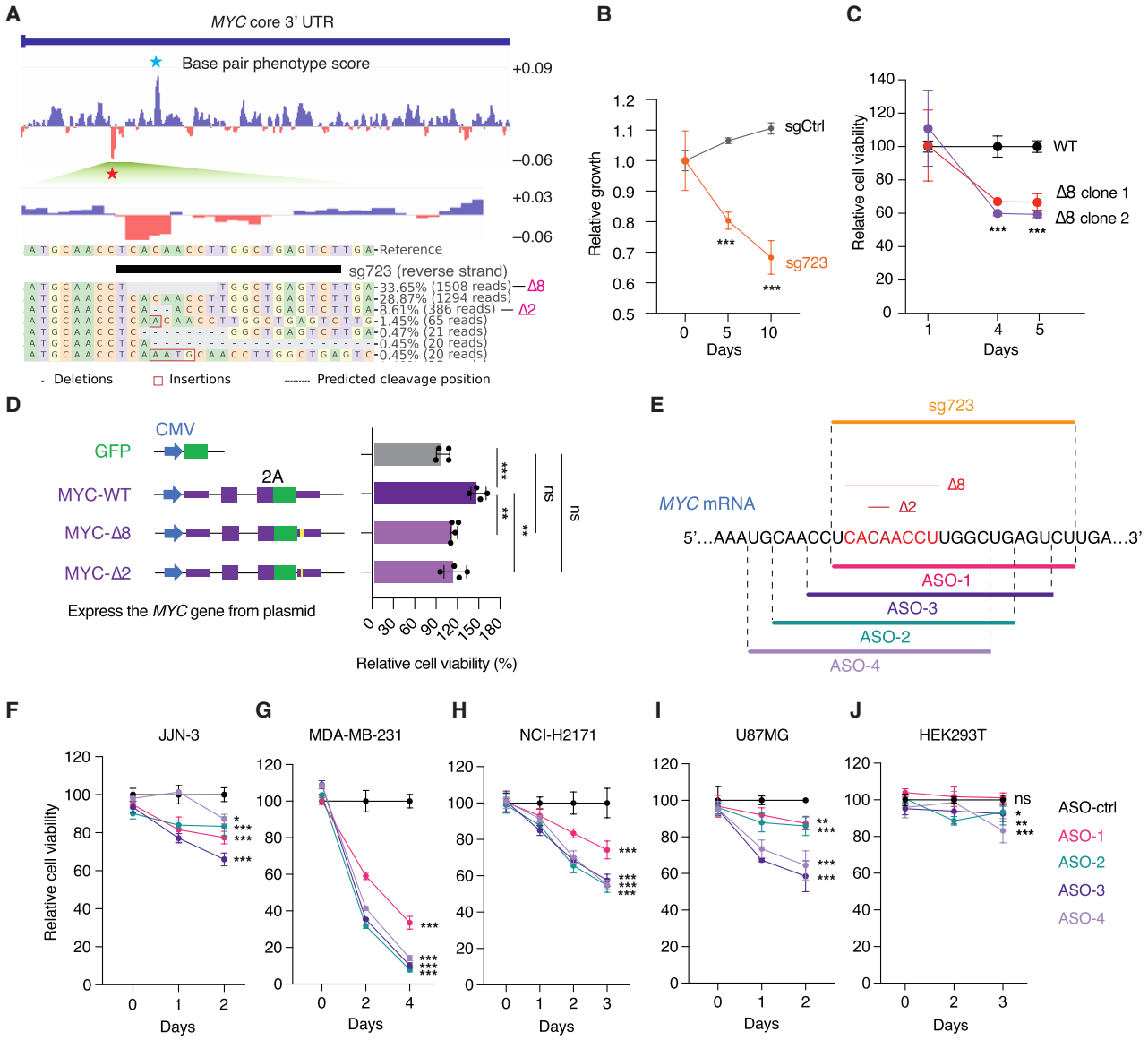


Figure 3. An ultraconserved 3′ UTR element required for MYC-dependent cell growth

(A) Base-pair phenotype scores of the 3′ UTR and zoom-in to the sg723 target site. Blue and red stars highlight base pairs with the strongest positive and negative phenotype scores, respectively. Amplicon sequencing reads indicating indels in D11 cells are also shown (frequency > 0.4% only).

(B) Competitive growth assay comparing HF1-SpRY-Cas9 D11 cells expressing sg723 or a non-targeting control sgRNA. Data were normalized to day 0.

(C) Relative cell viability (WST-1 assay) comparing two clonal cell lines, deleting the ultraconserved element, to a cell line targeted by a control sgRNA (WT). Data were normalized to WT.

(D) Relative cell viability (WST-1 assay) of HEK293T cells transfected with plasmids expressing GFP alone or full-length MYC constructs co-expressing d2GFP through a 2A sequence (MYC-WT, MYC-Δ8, or MYC-Δ2). Data were normalized to the GFP vector.

(E) Four ASOs targeting the ultraconserved element.

(F–J) Relative cell viability (WST-1 assay) in indicated cell lines transfected with a control ASO or one of four ASOs targeting the ultraconserved RNA element. Data were normalized to ASO-ctrl. Data are presented as mean ± standard deviation (SD). ns: not significant, $^{*}p < 0.05$, $^{**}p < 0.01$, $^{***}p < 0.001$.

3′ UTR-targeting ASOs inhibit MYC-dependent cancer cells

To explore therapeutic targeting of the 3′ UTR element, we designed four partially overlapping steric-blocking antisense oligonucleotides (ASOs) (Figure 3E and oligo sequences in Table S5). All ASOs were fully modified with 2′-O-methoxyethyl (2′-MOE) to enhance stability and binding affinity while reducing cytotoxicity by preventing RNase H-mediated target RNA cleavage or innate immune response to double-stranded RNAs (dsRNAs). Compared with a non-targeting control ASO (ASO-ctrl), all four ASOs significantly reduced the viability of JJN-3 cells (the parental cell line of D11, expressing WT MYC without a C-terminal GFP) (Figure 3F).

Please cite this article in press as: Shi et al., CRISPR mutagenesis of the *MYC* locus reveals a druggable ultraconserved RNA element, Cell (2027), https://doi.org/10.1016/j.cell.2026.10.002

The ASOs similarly reduced viability across diverse MYC-dependent cancer cell lines (Figures S9A and S9B), including MDA-MB-231 (TNBC, Figure 3G), NCI-H2171 (small cell lung cancer, Figure 3H), and U87MG (glioblastoma, Figure 3I), but had markedly weaker effects in HEK293T cells (Figure 3J), a non-malignant human cell line whose proliferation is independent of MYC, as efficient *MYC* knockdown by small interfering RNA (siRNA) (Figure S9A) does not affect HEK293T cell viability (Figure S9B). The markedly reduced growth defect in HEK293T cells upon ASO treatment also indicates that the observed phenotypes in other cells (Figures 3F–3I) are unlikely to result from ASO off-target effects or nonspecific toxicity. Consistent with this, the top predicted off-target candidates identified using established methods for steric-blocking ASOs[69,70] showed no detectable changes in either mRNA abundance or splicing in the RNA-seq data (Figures S10A–S10D). Furthermore, the cell viability defects caused by three distinct ASOs were significantly attenuated when the ultraconserved element was deleted from the endogenous *MYC* locus, both in bulk and clonal MYC-Δ8 cells (Figure S10E).

Together, these results establish the conserved 3′ UTR element as a selective therapeutic vulnerability of MYC-dependent cancer cells.

Controlling MYC activity without affecting abundance

Unexpectedly, despite the pronounced growth inhibition caused by targeting the 3′ UTR element, neither *MYC* mRNA (Figure 4A) nor protein (Figure 4B) abundance was significantly altered by sg723 in D11 cells. These findings were further supported by the lack of change in GFP levels, which is translated from the same *MYC* mRNA in these cells (Figure S11A). Similar results were observed in MDA-MB-231 cells (Figure S11B), confirmed using five different commercially available MYC antibodies (Figure S11C), and reproduced in MYC-Δ8 clonal cells (Figure S11D) and cells treated with ASOs targeting the element (Figure S11E).

To determine how the 3′ UTR element regulates cell growth independently of MYC abundance, we profiled transcriptomic changes in MDA-MB-231 cells transfected with three ASOs targeting the 3′ UTR element (ASO-1, ASO-2, and ASO-3; Figure 3E) vs. three control ASOs (Table S5). Differential expression analysis at 48 h (Table S6) and 72 h (Table S7) using DESeq2[72] confirmed that *MYC* expression remained unchanged (Figure 4C), with no alterations in *MYC* splicing, polyadenylation, or transcription start site usage (Figure S12). Remarkably, MYC target genes were significantly downregulated (Figure 4C). In fact, gene set enrichment analysis (GSEA) identified the MYC target gene set as the most significantly negatively enriched MSigDB hallmark pathway[73] (Figure 4D).

Consistent with MYC target gene downregulation, MYC chromatin immunoprecipitation sequencing (ChIP-seq) revealed globally reduced MYC occupancy at endogenous target sites following deletion of the ultraconserved element in two independent MYC-Δ8 clones or steric blockade with two distinct ASOs (Figures S13A and S13B). This trend is further supported by a global negative shift in peak read counts quantified by differential binding analysis with the *csaw* background-based normalization method[74] (Figures S13C and S13D). Furthermore, it is corroborated by reduced MYC binding at the promoters of individual genes previously shown to be bound by MYC[75] and significantly downregulated upon ASO treatment (Figure S13E). Transcriptomic changes induced by ASO treatment also correlated with those caused by *MYC* knockdown using siRNAs (Figure S13F, $r = 0.431$ at 48 h, Table S8, and $r = 0.303$ at 72 h, Table S9), with stronger concordance at the pathway level ($r = 0.840$ at 72 h, Figure 4E; $r = 0.547$ at 48 h, Figure S13G). Together, these findings demonstrate that disrupting the ultraconserved 3′ UTR element attenuates MYC transcriptional activity without altering MYC expression.

Consistent with the growth defects, cell cycle and metabolic programs were significantly negatively enriched, whereas apoptosis was positively enriched (Figure 4E). Annexin V (Figure 4F) and 7-Aminoactinomycin D (7-AAD) (Figure 4G) staining confirmed robust apoptosis induction, accompanied by increased autophagy following ASO treatment (Figure 4H). Intriguingly, the most positively enriched hallmark gene sets were dominated by interferon and innate immune responses (Figures 4D and 4E), suggesting a possible mechanism driving cellular apoptosis and autophagy (Figures 4F–4H). Remarkably, these pathway changes closely mirrored those induced by STING (Stimulator of Interferon Genes, encoded by *STING1*) in MDA-MB-436 cells ($r = 0.8$, Figure 4I),[71] consistent with *STING1* being a transcriptional target of MYC.[71,76] Accordingly, ASO treatment increased *STING1* mRNA (Figures 4C and S13H) and total and phosphorylated STING protein (Figure 4J). MYC has also been reported to suppress interferon-dependent genes through inhibiting TANK-binding kinase 1 (TBK1).[77,78] In line with this, phosphorylated TBK1 was also significantly upregulated following ASO treatment (Figure 4J).

To exclude the possibility that the observed interferon response was driven by dsRNA formation between ASOs and *MYC* mRNA, we tested two control ASOs targeting the *MYC* 3′ UTR outside the ultraconserved element (5 and 32 nt upstream, Table S5). Neither substantially reduced cell viability (Figure S13I), supporting the specificity of ASOs targeting the ultraconserved element and consistent with prior reports that 2′-MOE ASOs do not induce a dsRNA-mediated response.[79]

Together, these findings demonstrate that the 3′ UTR element is required for maintaining MYC's function as a transcription factor without affecting *MYC* mRNA and protein expression.

The 3′ UTR element promotes MYC protein nuclear localization

To elucidate how the 3′ UTR element regulates MYC function without altering its protein abundance, we examined MYC protein subcellular localization by immunofluorescence in MDA-MB-231 cells. Whereas MYC was predominantly nuclear in control cells (Figure 5A)—consistent with its role as a transcription factor—three independent ASOs targeting the ultraconserved element caused a marked redistribution of MYC to the cytoplasm and reduced nuclear MYC (Figure 5A, quantified in Figure 5B).

This altered localization was confirmed by orthogonal biochemical subcellular fractionation (Figure 5C). Blocking the CA-rich element with ASO-1 significantly reduced nuclear MYC without changing total MYC abundance. In the cytoplasm, MYC did not significantly increase in the soluble fraction but

Please cite this article in press as: Shi et al., CRISPR mutagenesis of the *MYC* locus reveals a druggable ultraconserved RNA element, Cell (2027), https://doi.org/10.1016/j.cell.2026.10.002

CellPress

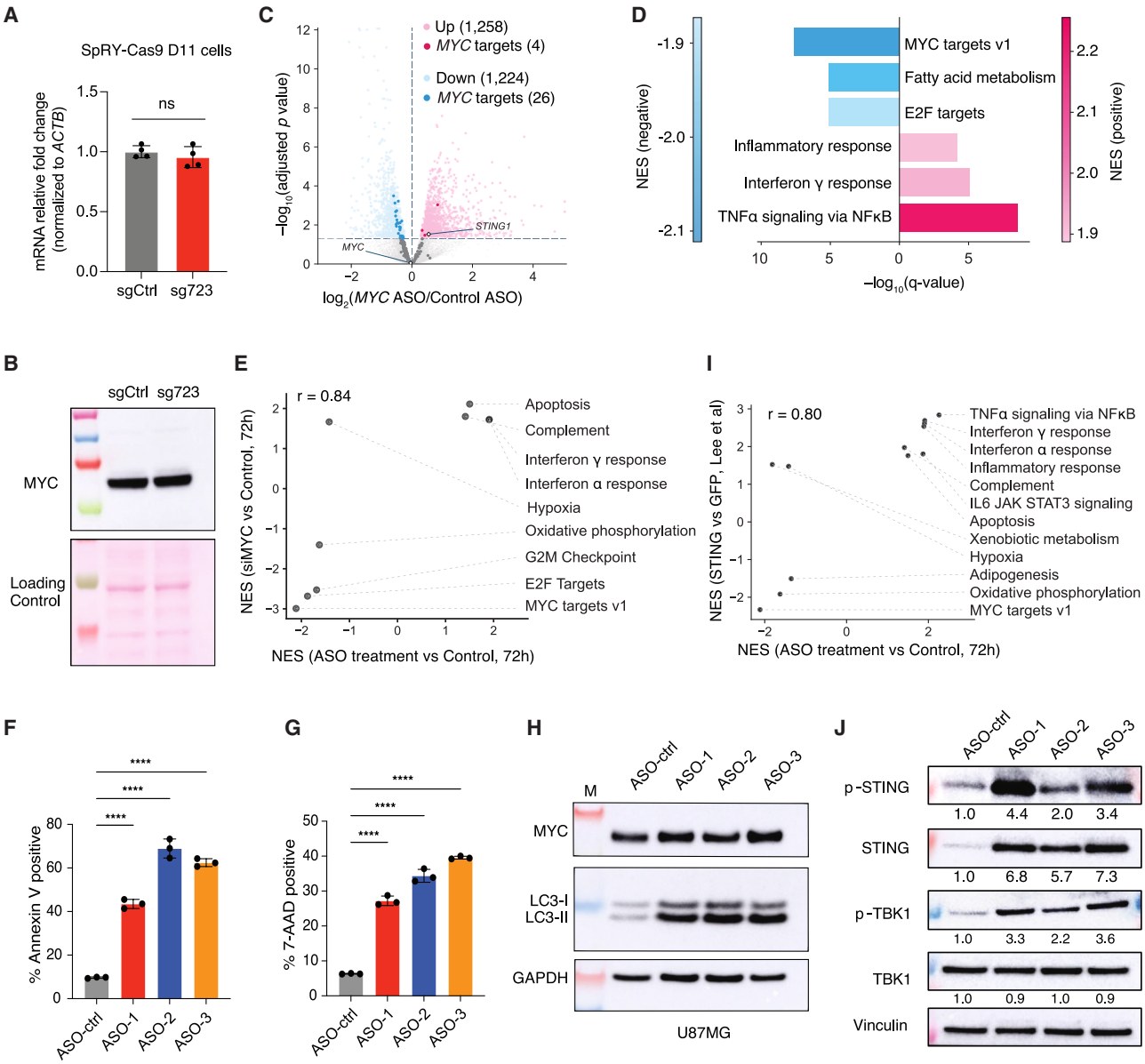


Figure 4. The ultraconserved 3′ UTR element controls MYC activity without affecting its abundance

(A) Quantitative reverse-transcription PCR (RT-qPCR) quantification of *MYC* mRNA in cells targeted by sg723 or a non-targeting control (sgCtrl) as in Figure 3B. Data were normalized to sgCtrl.

(B) As in (A) but for MYC protein. Ponceau S was used as a loading control.

(C) RNA-seq volcano plot showing ASO-induced gene expression change 72 h after ASO treatment ($N = 3$).

(D) Top three MSigDB hallmark gene sets significantly enriched among genes upregulated or downregulated in ASO-treated vs. ASO-control MDA-MB-231 cells at 72 h. NESs: normalized enrichment scores.

(E) Scatterplot of NES of MSigDB hallmark gene sets significantly affected (p.adjust < 0.05) by ASO treatment (x axis) and *MYC* siRNA knockdown (y axis) in MDA-MB-231 cells.

(F and G) Flow cytometric analysis of apoptosis in MDA-MB-231 cells 72 h after ASO treatment.

(H) Western blotting of MYC and LC3 in U87MG cells 48 h after ASO treatment. M: Marker.

(I) Scatterplot of NES of MSigDB hallmark gene sets significant (p.adjust < 0.05) in this study (x axis) and Lee et al.[71] (y axis).

(J) Western blotting of total and phosphorylated (p-) STING and TBK1 in MDA-MB-231 cells 72 h after ASO treatment. Data are presented as mean ± SD. ns: not significant, ****$p < 0.0001$.

Please cite this article in press as: Shi et al., CRISPR mutagenesis of the *MYC* locus reveals a druggable ultraconserved RNA element, Cell (2027), https://doi.org/10.1016/j.cell.2026.10.002

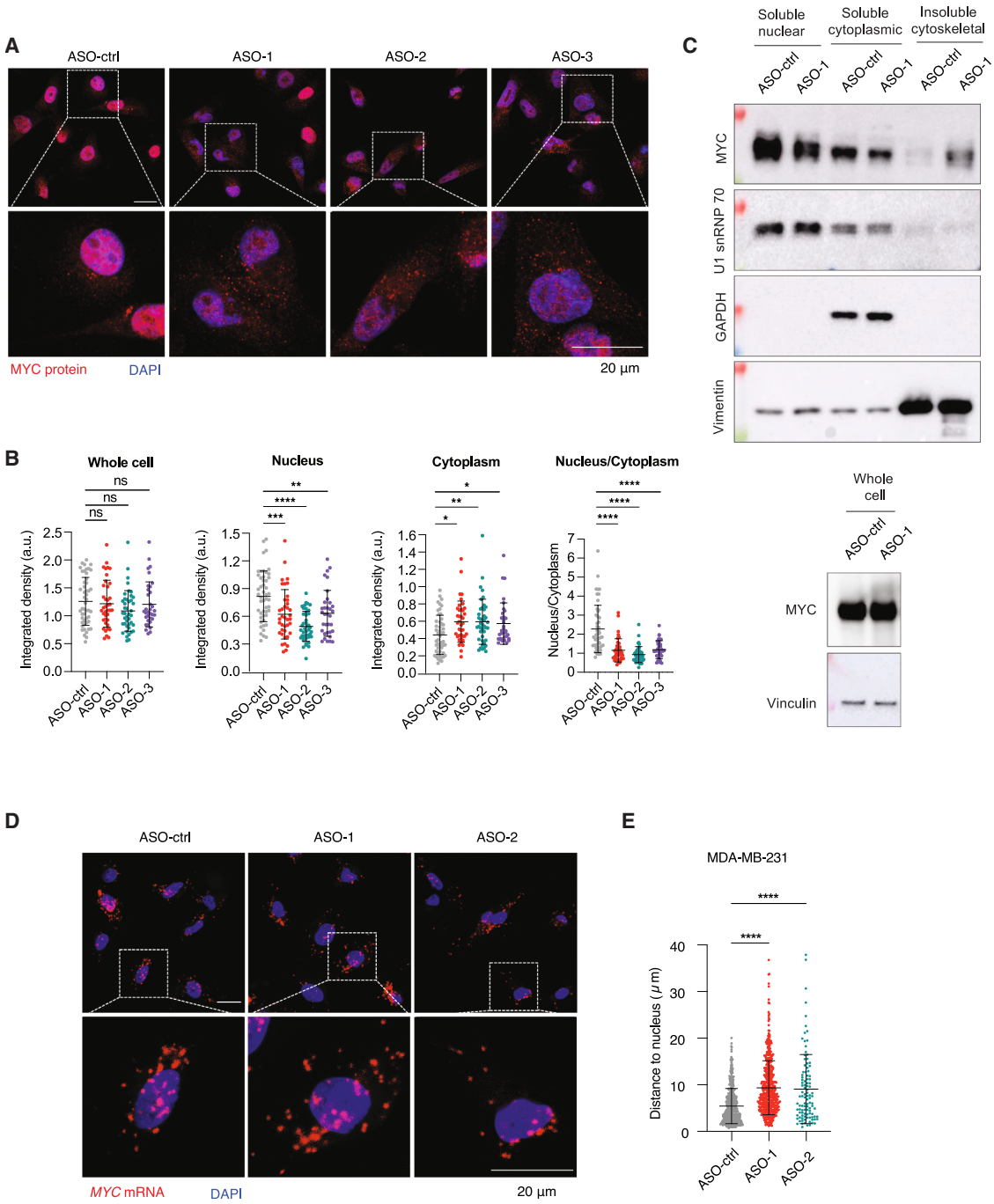


Figure 5. The ultraconserved 3′ UTR element facilitates *MYC* mRNA and protein localization

(A) Representative immunofluorescence images of MYC protein in MDA-MB-231 cells 48 h after transfection with ASO-ctrl or three targeting ASOs.

(B) Quantitative analysis of fluorescence shown in (A). ASO-ctrl: $N = 49$; ASO-1: $N = 39$; ASO-2: $N = 42$; ASO-3: $N = 34$.

(C) Subcellular fractionation of MDA-MB-231 cells treated with either ASO-ctrl or ASO-1 for 72 h, followed by Western blotting.

(D) Representative RNAscope images showing *MYC* mRNA localization in MDA-MB-231 cells treated with ASOs.

(E) Quantification of D with the distance of each *MYC* mRNA spot to the nearest nuclear boundary. ASO-ctrl, $N = 483$; ASO-1, $N = 500$; ASO-2, $N = 104$. a.u.: arbitrary units. Data are presented as mean ± SD. ns: not significant, $^{*}p < 0.05$, $^{**}p < 0.01$, $^{***}p < 0.001$, $^{****}p < 0.0001$. Scale bar: 20 μm.

Please cite this article in press as: Shi et al., CRISPR mutagenesis of the *MYC* locus reveals a druggable ultraconserved RNA element, Cell (2027), https://doi.org/10.1016/j.cell.2026.10.002

CellPress

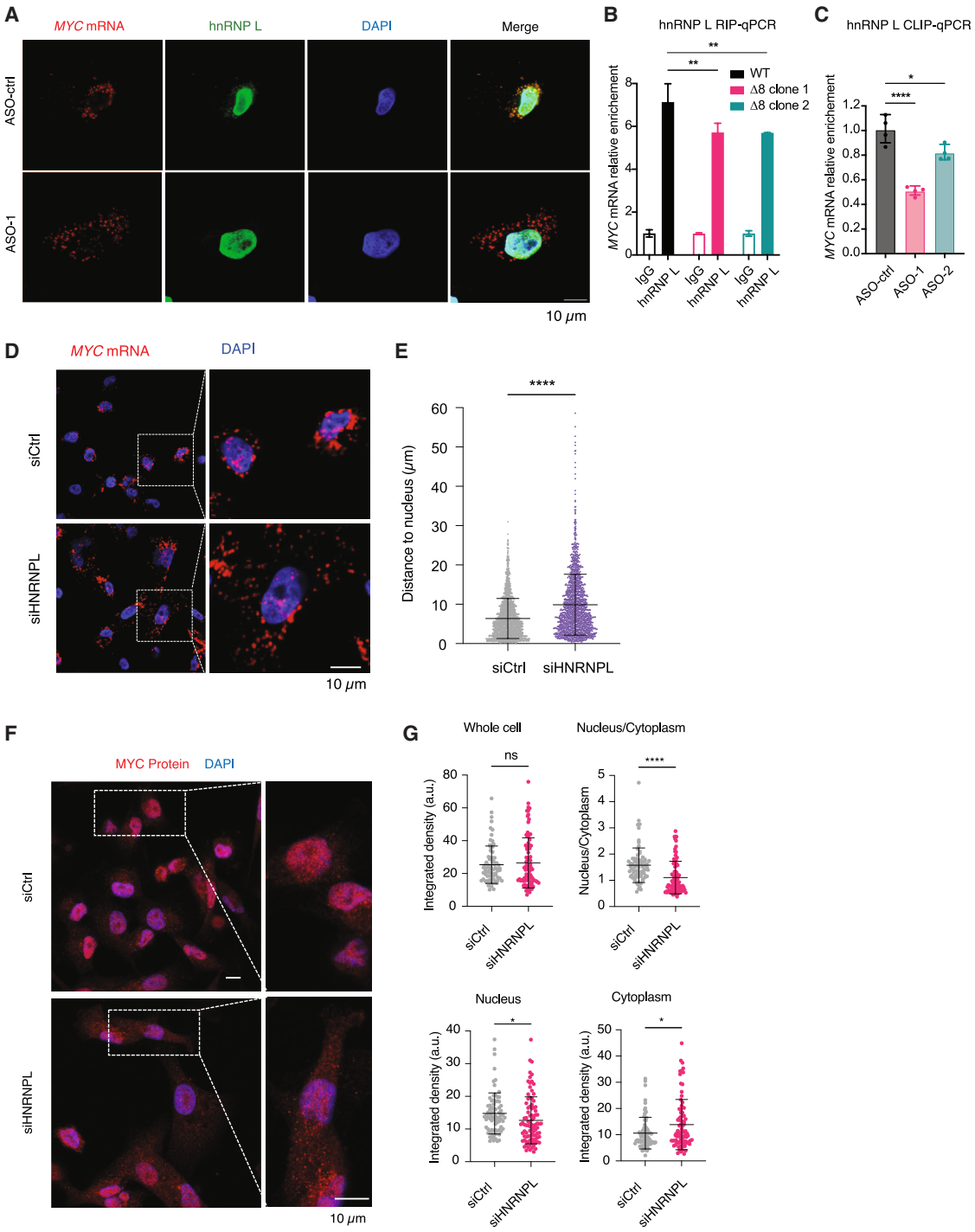


Figure 6. HnRNP L mediates perinuclear localization of *MYC* mRNA by the ultraconserved element

(A) Co-localization of hnRNP L protein and *MYC* mRNA in the cytoplasm is disrupted by ASO treatment (30 nM, 48 h) in MDA-MB-231 cells.

(B) Enrichment of *MYC* RNA in hnRNP L immunoprecipitation (IP) over immunoglobulin G (IgG) IP in UV-crosslinked wild-type (WT) or Δ8 cells. Data were normalized to the corresponding IgG control for each group.

(C) CLIP-qPCR analysis of hnRNP L-associated *MYC* mRNA following ASO treatment in MDA-MB-231 cells. Diluted total amplifiable libraries were used as internal control. Data were normalized to ASO-ctrl.

(D) Representative RNAscope images showing *MYC* mRNA (red) and nuclei (blue) in MDA-MB-231 cells transfected with either siCtrl or siHNRNPL after 5 days.

(legend continued on next page)

Please cite this article in press as: Shi et al., CRISPR mutagenesis of the *MYC* locus reveals a druggable ultraconserved RNA element, Cell (2027), https://doi.org/10.1016/j.cell.2026.10.002

accumulated substantially in the insoluble, cytoskeleton-enriched fraction, consistent with its intrinsically disordered, aggregation-prone nature and dependence on its 3′ UTR for proper folding.[80,81]

Three additional lines of evidence support a role for the 3′ UTR element in MYC protein nuclear import. First, whereas N-terminal HA-tagged MYC containing the WT 3′ UTR (MYC-WT) expressed from a plasmid was predominantly nuclear, deletion of the ultraconserved 3′ UTR element (MYC-Δ8 and MYC-Δ2 as in Figure 3D) caused pronounced cytoplasmic accumulation (Figures S14A–S14C). Second, Cas9/sg723-mediated disruption of the endogenous element similarly reduced nuclear localization of MYC (Figure S14D). Third, the growth defect caused by two independent ASOs was rescued by overexpressing MYC with two additional N-terminal nuclear localization signal (NLS) motifs that facilitate nuclear import and without its native 3′ UTR to escape ASO targeting (Figure S14E).

Together, these findings demonstrate that the ultraconserved 3′ UTR element promotes the nuclear localization of MYC protein, explaining the loss of MYC function when the element is disrupted or blocked.

The 3′ UTR element mediates *MYC* mRNA perinuclear localization via hnRNP L

We next investigated how the 3′ UTR element promotes MYC protein nuclear localization. *MYC* mRNAs have been shown to localize near the nuclear periphery,[82] enabling local translation and rapid nuclear import of nascent MYC protein,[82] a spatial coupling that is particularly important given MYC's short 20–30 min half-life, which is only slightly longer than the ∼6 to 15 min required for nuclear import through its NLS.[83,84] Consistent with this model, *MYC* mRNA was predominantly perinuclear in control ASO-treated cells but became more dispersed throughout the cytoplasm following treatment with two independent ASOs targeting the ultraconserved element (Figures 5D and 5E). The specificity of this effect is further validated using two additional control ASOs (Figures S14F and S14G). Digitonin fractionation confirmed a corresponding shift of *MYC* mRNA from the perinuclear membrane to cytoplasmic fraction upon ASO treatment (Figures S14H and S14I), while SpRY-Cas9/sg723-mediated disruption of the element produced a similar defect (Figure S14J). Together, these orthogonal imaging, biochemical, and genetic approaches demonstrate that the 3′ UTR element is required for perinuclear localization of *MYC* mRNA, providing a mechanistic explanation for its role in MYC protein localization.

The ultraconserved element (CACAACC) is CA-rich and closely resembles established binding motifs for the RNA-binding protein heterogeneous nuclear ribonucleoprotein L (hnRNP L).[85,86] Best known for its nuclear role in pre-mRNA splicing, hnRNP L also functions in the cytoplasm, where it regulates mRNA stability and translation[87–90] and notably mediates the perinuclear localization of *NOS2* mRNA in rat hepatocytes.[91] In MDA-MB-231 cells, hnRNP L was predominantly nuclear, but a distinct perinuclear pool was also detected (Figure 6A). Strikingly, this perinuclear hnRNP L exhibited near-complete colocalization with *MYC* mRNA (Figure 6A, additional examples in Figure S15) under super-resolution microscopy. Remarkably, this colocalization was completely abolished upon ASO-mediated blockade of the CA-rich element (Figures 6A and S15). Unexpectedly, ASO treatment also eliminated the perinuclear pool of hnRNP L protein without affecting *HNRNPL* mRNA levels (48 h: log2FC = 0.14, *p*.adjust = 0.67; 72 h: log2FC = −0.11, *p*.adjust = 0.62), indicating that the element is required for perinuclear localization of both *MYC* mRNA and hnRNP L protein. These findings were independently reproduced in U2OS cells (Figure S16A), a widely used osteosarcoma cell line that likewise exhibits reduced viability following ASO treatment (Figure S16B).

Analysis of published cross-linking and immunoprecipitation followed by sequencing (CLIP-seq) datasets revealed that hnRNP L directly binds this CA-rich ultraconserved element within *MYC* across multiple human cell types, including $CD4^+$ T cells, Jurkat/JSL1 T cells, and K562 cells[85,92] (Figures S17A and S17B). Using UV crosslinking followed by RNA immunoprecipitation (RIP) and qPCR, we show that *MYC* mRNA is bound by hnRNP L in D11 cells, and this binding is significantly reduced in MYC-Δ8 cells where the endogenous CA-rich element is deleted (Figure 6B). The loss of hnRNP L binding to the CA-rich element in MYC-Δ8 cells is further confirmed using CLIP-qPCR (Figure S17C). ASO treatment similarly reduced hnRNP L binding around the CA-rich element (CLIP-qPCR; Figure 6C). Together, these complementary results support that hnRNP L binds to *MYC* mRNA via the CA-rich element.

Phenocopying ASOs targeting the ultraconserved CA-rich element (Figures 3, 4, 5, and 6), siRNA-mediated knockdown of hnRNP L (Figure S17D) did not change total *MYC* mRNA abundance (Figure S17E), yet markedly reduced cell viability (Figure S17F), increased the distance between *MYC* mRNA and the nucleus (Figures 6D and 6E), and decreased nuclear accumulation of MYC protein (Figures 6F and 6G). RNA-seq analysis (Table S10) further showed that hnRNP L knockdown recapitulates ASO-induced pathway changes, including negative enrichment of MYC target genes and positive enrichment of innate immune response and apoptosis (Figure S17G). The sequencing data further confirmed that *MYC* mRNA splicing and polyadenylation remain unchanged upon hnRNP L knockdown (Figure S17H).

Together, these findings reveal that hnRNP L directs 3′ UTR element-dependent perinuclear localization of *MYC* mRNA, enabling MYC protein to function as a transcription factor driving cancer cell growth.

ASOs suppress tumor growth in patient-derived organoid models

To further assess the therapeutic efficacy of *MYC* 3′ UTR-targeting ASOs in clinically relevant systems, we evaluated these ASOs in two patient-derived organoid (PDO) models.[93] PDO

(E) Quantification of D with the distance of each *MYC* mRNA spot to the nearest nuclear boundary. siCtrl, $N = 1{,}891$. siHNRNPL, $N = 1{,}538$.
(F) Representative immunofluorescence images of MYC protein in MDA-MB-231 cells 5 days after transfection with siCtrl or siHNRNPL.
(G) Quantitative analysis of fluorescence shown in (F). siCtrl, $N = 76$. siHNRNPL, $N = 90$. a.u.: arbitrary units. Data are presented as mean ± SD. ns: not significant, $^*p < 0.05$, $^{**}p < 0.01$, and $^{****}p < 0.0001$. Scale bar: 10 μm.

Please cite this article in press as: Shi et al., CRISPR mutagenesis of the *MYC* locus reveals a druggable ultraconserved RNA element, Cell (2027), https://doi.org/10.1016/j.cell.2026.10.002

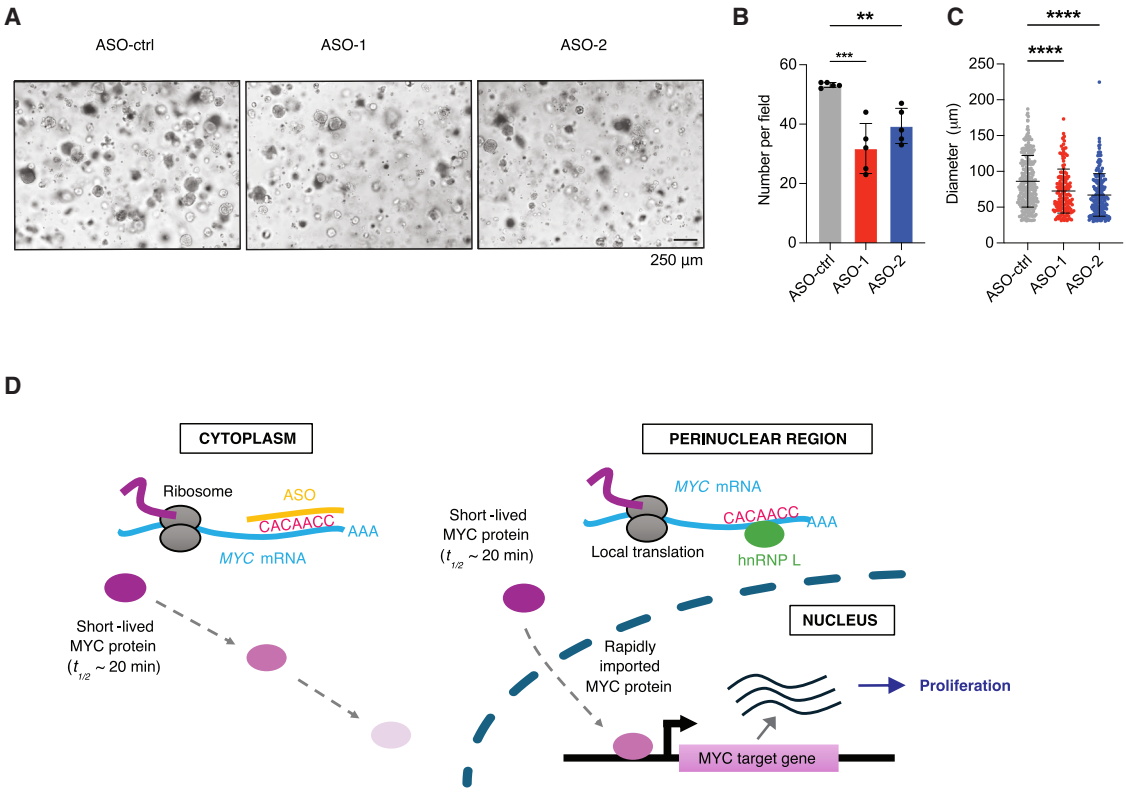


Figure 7. ASOs suppress tumor growth in patient-derived organoid models

(A) Representative images of head and neck cancer patient-derived organoids (PDOs) 9 days after treatment with ASO-ctrl or two ASOs targeting the 3′ UTR element.

(B) Quantitative analysis of the number of organoids per field. $N = 5$.

(C) Quantitative analysis of the diameter of organoids. ASO-ctrl, $N = 266$; ASO-1, $N = 159$; ASO-2, $N = 200$.

(D) Model for MYC regulation by an ultraconserved 3′ UTR element and hnRNP L. Data are presented as mean ± SD. $^{**}p < 0.01$, $^{***}p < 0.001$, and $^{****}p < 0.0001$. Scale bar: 250 μm.

models recapitulate tumor architecture, genetics, heterogeneity, and clinical treatment responses[93–97] and perform comparably to patient-derived xenografts (PDXs) in predicting matched patient responses.[98,99] Both ASO-1 and ASO-2 markedly suppressed organoid formation and growth relative to control ASO in a head and neck cancer PDO (Figures 7A–7C). Similar organoid formation suppression was observed in an esophageal adenocarcinoma (EAC) PDO model (Figure S18). These findings support the potent anti-tumor activity and translational potential of *MYC*-targeting ASOs in human cancer.

DISCUSSION

In this study, we mapped the fitness landscape of an entire human protein-coding gene at base-pair resolution in its native genomic context. Beyond revealing noncoding sequence as a major carrier of functional information, this systematic analysis uncovered an ultraconserved RNA regulatory element that is essential for MYC function and can be therapeutically targeted to suppress cancer cell growth (Figure 7D). Central to these discoveries is the ability of the high-fidelity, near-PAMless SpRY-Cas9 to target virtually every base pair with multiple sgRNAs, while mitigating the effects of individual sgRNA off-target activity and variability in on-target efficiency by aggregating signals across multiple sgRNAs targeting the same base pair.

Our unbiased analysis reveals a critical role of noncoding sequences in shaping the functional architecture of the *MYC* locus, accounting for approximately two-thirds of the base pairs with the strongest phenotypic effects (Figure 2A). This proportion is likely underestimated for two reasons. First, noncoding regulatory elements often function in a cell type- or condition-specific manner, whereas our analysis was performed in a single cell line and under unstimulated conditions. Second, many noncoding regions are AT-rich, especially the highly conserved 3′ UTR, resulting in enrichment of less efficient AT-rich PAMs (Figure 1H) and often exhibiting markedly reduced chromatin accessibility (low DNase signal in Figure 2D), both of which could impair Cas9 activity.

We also uncovered an ultraconserved 3′ UTR element that is essential for MYC-dependent cancer cells by recruiting hnRNP L to promote *MYC* mRNA perinuclear localization and subsequent nuclear import of locally translated short-lived MYC protein (Figure 7D). MYC proteins translated from more distal mRNAs may be less competent for nuclear import, as reported for *MT-1* mRNA,[100] or may simply require more time to reach

Please cite this article in press as: Shi et al., CRISPR mutagenesis of the *MYC* locus reveals a druggable ultraconserved RNA element, Cell (2027), https://doi.org/10.1016/j.cell.2026.10.002

the nucleus, reducing the fraction of their short lifetime available for target gene regulation (Figure 7D). Failure of nuclear import appears to also promote cytoplasmic aggregation of MYC protein (Figure 5C). Furthermore, recent studies have shown that disrupting *MYC* mRNA perinuclear localization and translation in the TIS granule[101] inhibits MYC activity by disrupting co-translational protein complex assembly,[102] which may also contribute to the growth defect resulting from disruption of the ultraconserved element.

We developed steric-blocking ASOs targeting the ultraconserved 3′ UTR element that selectively eliminate MYC-dependent cancer cells (Figure 3). RNA-targeting ASOs have transformed the treatment of rare and common diseases.[103,104] Previously developed *MYC*-targeting ASOs, such as INX-3280, INX-6295,[105] and MYCASO,[106] act via RNase H-mediated cleavage of *MYC* RNA, which are associated with widespread off-target RNA degradation and immunogenicity.[107,108] Similar limitations also apply to *MYC* RNA knockdown using siRNAs. By contrast, fully 2′-MOE-modified steric blocking ASOs, as used in this study, act without RNA cleavage and exhibit substantially reduced immunogenicity.[79,109] Although unintended RNA binding remains possible, it is generally less deleterious than cleavage-mediated degradation. Unlike protein-targeting drugs such as OMO-103,[110] RNA-targeting ASOs also offer the potential for efficient intracellular delivery without requiring nuclear entry. Given MYC's broad involvement in cancer, obesity,[111] cardiovascular diseases,[112–114] autoimmune diseases,[115,116] neurological disorders,[117] and aging,[118] our ASOs may have therapeutic potential beyond cancer.

Our work establishes a blueprint for unbiased, high-resolution interrogation of the genome. We anticipate that extending this approach to additional genes will collectively reveal fundamental design principles of gene structure and regulatory architecture while uncovering previously unrecognized layers of gene regulation. Our study also highlights the power of coupling unbiased functional screens with RNA-targeted modalities such as ASOs to accelerate translational applications, including the development of therapies against targets long considered "undruggable" by conventional approaches.

Limitations of the study

Several limitations warrant further investigation. Although SpRY-Cas9 substantially expanded targetable sequence space, T-rich PAMs remain relatively inefficient and may cause false negatives; Cas12 systems with T-rich PAM preferences may help address this limitation.[119] Beyond PAM-related biases, spacer-sequence-dependent differences in guide RNA activity, variable chromatin accessibility, and DNA repair outcomes can also introduce bias and obscure functional base pairs. Our tiling mutagenesis approach also lacked precise control over the mutations generated, which could be complemented by base- or prime-editing screens as editing efficiencies improve. Mechanistically, future studies should determine how the CA-rich element promotes perinuclear localization of hnRNP L and *MYC* mRNA and define the function of the conserved RNA stem-loop linking the two ultraconserved elements. Therapeutically, systematic *in vivo* studies are needed to evaluate the efficacy, biodistribution, and safety of *MYC* mRNA-targeting ASOs. Finally, extending this framework across additional genes and species will determine whether similar regulatory landscapes and RNA-mediated mechanisms are broadly conserved.

RESOURCE AVAILABILITY

Lead contact

Requests for resources and reagents should be directed to, and will be fulfilled by, the lead contact, Xuebing Wu (xuebing.wu@columbia.edu).

Materials availability

Unique reagents generated in this study are available from the lead contact with a completed materials transfer agreement.

Data and code availability

- Tiling mutagenesis data have been deposited in NCBI Gene Expression Omnibus (GEO; accession GEO: GSE317040). RNA-seq and ChIP-seq data have been deposited in NCBI GEO (GEO: GSE317096). All are publicly available as of the date of publication.
- Custom code used in this study is available on GitHub (10.5281/zenodo.22943190; https://github.com/FeiyueYang01/MYC-SpRY-Screening).
- All code is publicly available as of the date of publication.
- Any additional information required to reanalyze the data reported in this paper is available from the lead contact upon request.

ACKNOWLEDGMENTS

We thank members of the Wu, Zaccara, and Zhang groups and the Cardiometabolic Genomics Program at Columbia University for discussion; Dr. Jerry Pelletier and Dr. Francis Robert for sharing the D11 and JJN-3 cell lines; and Dr. Peter A. Sims for sharing the U87MG cell line. X.W. is supported by DP2GM140977, R01HL171664, the Pershing Square Sohn Cancer Prize, and the Pew-Stewart Scholars for Cancer Research. J.Q. is supported in part by R01HL179522, R35HL184263, R01DK144271, R01CA272901, P01CA268991, and AGA2024-32-03. C.Z. is supported in part by R35GM145279, R01HG014077, and R01HG012359. Y.C.L. is supported in part by R35GM157319. S.Z. is supported by DP2HD118273. This research was funded in part through the NIH/NCI Cancer Center Support grant P30CA013696 and used the Genomics and High Throughput Screening Shared Resource; the Molecular Pathology Shared Resource; the CCTI Flow Cytometry Core; and the CU-DLDRC and its CBRC, BIC, OCCC, and BSCAC cores via NIH grant P30DK132710. The CCTI Flow Cytometry Core is supported in part by the Office of the Director, National Institutes of Health, under awards S10OD030282 and S10OD020056.

AUTHOR CONTRIBUTIONS

P.S. and X.W. conceived the project. P.S. and T.F. performed most of the experiments. F.Y. performed most of the computational analyses. J.Q. supervised the experiments performed by T.F., including RT-qPCR, flow cytometry, immunofluorescence, RNAscope, plasmid generation, and organoid models. X.W. and S.Z. supervised the computational analyses performed by F.Y. W.H. assisted with ASO validation. L.X. assisted with subcellular fractionation assays. S.A. and W.D. performed CLIP supervised by C.Z. P.I. and L.W. assisted with ASO validation. A.O.A. assisted with plasmid generation and validation as well as confirmation of ASO function. C.H.K. assisted with computational analyses. A.T., M.R.M., C.Z., S.Z., M.P.R., E.R.R., L.W., and L.X. edited the manuscript and provided critical feedback. C.Z. assisted in identifying hnRNP L as the protein recognizing the ultraconserved element. Y.C.L. assisted and supervised hnRNP L localization analyses. P.S., F.Y., and X.W. wrote the manuscript with input from all authors.

DECLARATION OF INTERESTS

X.W. is a member of the Scientific Advisory Board for Epitor Therapeutics and has received speaking honoraria from Eli Lilly and Company. C.Z. is a co-founder of DAYI Therapeutics, Inc. P.S. and X.W. are named inventors on

Please cite this article in press as: Shi et al., CRISPR mutagenesis of the *MYC* locus reveals a druggable ultraconserved RNA element, Cell (2027), https://doi.org/10.1016/j.cell.2026.10.002

provisional US patent application (no. 63/875,602), filed by the Trustees of Columbia University in the City of New York.

STAR★METHODS

Detailed methods are provided in the online version of this paper and include the following:

- KEY RESOURCES TABLE
- EXPERIMENTAL MODEL AND STUDY PARTICIPANT DETAILS
  - Cell culture
  - Patient-derived organoids
  - Ethics statement
- METHOD DETAILS
  - Plasmid construction
  - Cloning the *MYC* locus on plasmids
  - sgRNA library design
  - sgRNA library cloning
  - CRISPR tiling mutagenesis screening
  - Competitive assay
  - Cell proliferation assays
  - Amplicon sequencing for on-target and off-target mutation analysis
  - ASO transfection
  - siRNA transfection
  - Quantitative reverse transcription PCR
  - Western blot
  - Subcellular fractionation
  - Immunofluorescence
  - 2×NLS-MYC rescue assay
  - RNAscope
  - Super-resolution analysis of *MYC* mRNA and hnRNP L colocalization
  - Apoptosis analysis by Annexin V/7-AAD staining
  - Single-cell cloning and genotyping
  - RNA-seq
  - ChIP-seq
  - UV-crosslinked RNA immunoprecipitation followed by RT-qPCR
  - hnRNP L CLIP-qPCR
  - Digitonin-based RNA fractionation and RT-qPCR
  - ASO transfection in patient-derived organoid
- QUANTIFICATION AND STATISTICAL ANALYSIS
  - sgRNA phenotype score calculation
  - Base-pair phenotype score calculation
  - Gene and feature annotations
  - Off-target and target efficiency prediction
  - Conservation-function correlation
  - 3′ UTR conservation and mRNA half-life
  - Visualization with UCSC Genome Browser
  - Covariation
  - RNA-seq analysis
  - ChIP-seq analysis
  - Statistics and reproducibility

SUPPLEMENTAL INFORMATION

Supplemental information can be found online at https://doi.org/10.1016/j.cell.2026.10.002.

Received: March 31, 2026
Revised: August 28, 2026
Accepted: October 1, 2026

REFERENCES

1. The ENCODE Project Consortium (2012). An Integrated Encyclopedia of DNA Elements in the Human Genome. Nature *489*, 57–74. https://doi.org/10.1038/nature11247.
2. Elkon, R., and Agami, R. (2017). Characterization of noncoding regulatory DNA in the human genome. Nat. Biotechnol. *35*, 732–746. https://doi.org/10.1038/nbt.3863.
3. Cech, T.R., and Steitz, J.A. (2014). The Noncoding RNA Revolution—Trashing Old Rules to Forge New Ones. Cell *157*, 77–94. https://doi.org/10.1016/j.cell.2014.03.008.
4. Leypold, N.A., and Speicher, M.R. (2021). Evolutionary conservation in noncoding genomic regions. Trends Genet. *37*, 903–918. https://doi.org/10.1016/j.tig.2021.06.007.
5. La Fleur, A., Shi, Y., and Seelig, G. (2024). Decoding biology with massively parallel reporter assays and machine learning. Genes Dev. *38*, 843–865. https://doi.org/10.1101/gad.351800.124.
6. Arnold, C.D., Gerlach, D., Stelzer, C., Boryń, Ł.M., Rath, M., and Stark, A. (2013). Genome-Wide Quantitative Enhancer Activity Maps Identified by STARR-seq. Science *339*, 1074–1077. https://doi.org/10.1126/science.1232542.
7. Rosenberg, A.B., Patwardhan, R.P., Shendure, J., and Seelig, G. (2015). Learning the sequence determinants of alternative splicing from millions of random sequences. Cell *163*, 698–711. https://doi.org/10.1016/j.cell.2015.09.054.
8. Bogard, N., Linder, J., Rosenberg, A.B., and Seelig, G. (2019). A Deep Neural Network for Predicting and Engineering Alternative Polyadenylation. Cell *178*, 91–106.e23. https://doi.org/10.1016/j.cell.2019.04.046.
9. Zhao, W., Pollack, J.L., Blagev, D.P., Zaitlen, N., McManus, M.T., and Erle, D.J. (2014). Massively parallel functional annotation of 3′ untranslated regions. Nat. Biotechnol. *32*, 387–391. https://doi.org/10.1038/nbt.2851.
10. Sample, P.J., Wang, B., Reid, D.W., Presnyak, V., McFadyen, I.J., Morris, D.R., and Seelig, G. (2019). Human 5′ UTR design and variant effect prediction from a massively parallel translation assay. Nat. Biotechnol. *37*, 803–809. https://doi.org/10.1038/s41587-019-0164-5.
11. Zhang, J., Leung, A.K.-Y., Zhu, Y., Yao, L., Willis, A., Pan, X., Ozer, A., Zhou, Z., Siklenka, K., Barrera, A., et al. (2025). Comprehensive evaluation of diverse massively parallel reporter assays to functionally characterize human enhancers genome-wide. Genome Biol. *26*, 378. https://doi.org/10.1186/s13059-025-03828-8.
12. Dao, K., Jungers, C.F., Djuranovic, S., and Mustoe, A.M. (2025). U-rich elements drive pervasive cryptic splicing in 3′ UTR massively parallel reporter assays. Nat. Commun. *16*, 6844. https://doi.org/10.1038/s41467-025-62000-9.
13. Canver, M.C., Lessard, S., Pinello, L., Wu, Y., Ilboudo, Y., Stern, E.N., Needleman, A.J., Galactéros, F., Brugnara, C., Kutlar, A., et al. (2017). Variant-aware saturating mutagenesis using multiple Cas9 nucleases identifies regulatory elements at trait-associated loci. Nat. Genet. *49*, 625–634. https://doi.org/10.1038/ng.3793.
14. Sanjana, N.E., Wright, J., Zheng, K., Shalem, O., Fontanillas, P., Joung, J., Cheng, C., Regev, A., and Zhang, F. (2016). High-resolution interrogation of functional elements in the noncoding genome. Science *353*, 1545–1549. https://doi.org/10.1126/science.aaf7613.
15. Korkmaz, G., Lopes, R., Ugalde, A.P., Nevedomskaya, E., Han, R., Myacheva, K., Zwart, W., Elkon, R., and Agami, R. (2016). Functional genetic screens for enhancer elements in the human genome using CRISPR-Cas9. Nat. Biotechnol. *34*, 192–198. https://doi.org/10.1038/nbt.3450.
16. Rajagopal, N., Srinivasan, S., Kooshesh, K., Guo, Y., Edwards, M.D., Banerjee, B., Syed, T., Emons, B.J.M., Gifford, D.K., and Sherwood, R.I. (2016). High-throughput mapping of regulatory DNA. Nat. Biotechnol. *34*, 167–174. https://doi.org/10.1038/nbt.3468.
17. Diao, Y., Li, B., Meng, Z., Jung, I., Lee, A.Y., Dixon, J., Maliskova, L., Guan, K.-L., Shen, Y., and Ren, B. (2016). A new class of temporarily phenotypic enhancers identified by CRISPR/Cas9-mediated genetic screening. Genome Res. *26*, 397–405. https://doi.org/10.1101/gr.197152.115.

18. Diao, Y., Fang, R., Li, B., Meng, Z., Yu, J., Qiu, Y., Lin, K.C., Huang, H., Liu, T., Marina, R.J., et al. (2017). A tiling-deletion-based genetic screen for cis-regulatory element identification in mammalian cells. Nat. Methods *14*, 629–635. https://doi.org/10.1038/nmeth.4264.

19. Yao, Y., Zhou, Z., Wang, X., Liu, Z., Zhai, Y., Chi, X., Du, J., Luo, L., Zhao, Z., Wang, X., et al. (2024). SpRY-mediated screens facilitate functional dissection of non-coding sequences at single-base resolution. Cell Genomics *4*, 100583. https://doi.org/10.1016/j.xgen.2024.100583.

20. Hsu, J.Y., Fulco, C.P., Cole, M.A., Canver, M.C., Pellin, D., Sher, F., Farouni, R., Clement, K., Guo, J.A., Biasco, L., et al. (2018). CRISPR-SURF: discovering regulatory elements by deconvolution of CRISPR tiling screen data. Nat. Methods *15*, 992–993. https://doi.org/10.1038/s41592-018-0225-6.

21. Canver, M.C., Smith, E.C., Sher, F., Pinello, L., Sanjana, N.E., Shalem, O., Chen, D.D., Schupp, P.G., Vinjamur, D.S., Garcia, S.P., et al. (2015). BCL11A enhancer dissection by Cas9-mediated in situ saturating mutagenesis. Nature *527*, 192–197. https://doi.org/10.1038/nature15521.

22. Klann, T.S., Black, J.B., Chellappan, M., Safi, A., Song, L., Hilton, I.B., Crawford, G.E., Reddy, T.E., and Gersbach, C.A. (2017). CRISPR-Cas9 epigenome editing enables high-throughput screening for functional regulatory elements in the human genome. Nat. Biotechnol. *35*, 561–568. https://doi.org/10.1038/nbt.3853.

23. Fulco, C.P., Munschauer, M., Anyoha, R., Munson, G., Grossman, S.R., Perez, E.M., Kane, M., Cleary, B., Lander, E.S., and Engreitz, J.M. (2016). Systematic mapping of functional enhancer–promoter connections with CRISPR interference. Science *354*, 769–773. https://doi.org/10.1126/science.aag2445.

24. Xie, S., Duan, J., Li, B., Zhou, P., and Hon, G.C. (2017). Multiplexed Engineering and Analysis of Combinatorial Enhancer Activity in Single Cells. Mol. Cell *66*, 285–299.e5. https://doi.org/10.1016/j.molcel.2017.03.007.

25. Simeonov, D.R., Gowen, B.G., Boontanrart, M., Roth, T.L., Gagnon, J.D., Mumbach, M.R., Satpathy, A.T., Lee, Y., Bray, N.L., Chan, A.Y., et al. (2017). Discovery of stimulation-responsive immune enhancers with CRISPR activation. Nature *549*, 111–115. https://doi.org/10.1038/nature23875.

26. Reilly, S.K., Gosai, S.J., Gutierrez, A., Mackay-Smith, A., Ulirsch, J.C., Kanai, M., Mouri, K., Berenzy, D., Kales, S., Butler, G.M., et al. (2021). Direct characterization of cis-regulatory elements and functional dissection of complex genetic associations using HCR-FlowFISH. Nat. Genet. *53*, 1166–1176. https://doi.org/10.1038/s41588-021-00900-4.

27. Lopes, R., Sprouffske, K., Sheng, C., Uijttewaal, E.C.H., Wesdorp, A.E., Dahinden, J., Wengert, S., Diaz-Miyar, J., Yildiz, U., Bleu, M., et al. (2021). Systematic dissection of transcriptional regulatory networks by genome-scale and single-cell CRISPR screens. Sci. Adv. *7*, eabf5733. https://doi.org/10.1126/sciadv.abf5733.

28. Wünnemann, F., Fotsing Tadjo, T., Beaudoin, M., Lalonde, S., Lo, K.S., Kleinstiver, B.P., and Lettre, G. (2023). Multimodal CRISPR perturbations of GWAS loci associated with coronary artery disease in vascular endothelial cells. PLoS Genet. *19*, e1010680. https://doi.org/10.1371/journal.pgen.1010680.

29. Chen, Z., Javed, N., Moore, M., Wu, J., Sun, G., Vinyard, M., Collins, A., Pinello, L., Najm, F.J., and Bernstein, B.E. (2023). Integrative dissection of gene regulatory elements at base resolution. Cell Genomics *3*, 100318. https://doi.org/10.1016/j.xgen.2023.100318.

30. Martin-Rufino, J.D., Castano, N., Pang, M., Grody, E.I., Joubran, S., Caulier, A., Wahlster, L., Li, T., Qiu, X., Riera-Escandell, A.M., et al. (2023). Massively parallel base editing to map variant effects in human hematopoiesis. Cell *186*, 2456–2474.e24. https://doi.org/10.1016/j.cell.2023.03.035.

31. Cheng, L., Li, Y., Qi, Q., Xu, P., Feng, R., Palmer, L., Chen, J., Wu, R., Yee, T., Zhang, J., et al. (2021). Single-nucleotide-level mapping of DNA regulatory elements that control fetal hemoglobin expression. Nat. Genet. *53*, 869–880. https://doi.org/10.1038/s41588-021-00861-8.

32. Ren, X., Yang, H., Nierenberg, J.L., Sun, Y., Chen, J., Beaman, C., Pham, T., Nobuhara, M., Takagi, M.A., Narayan, V., et al. (2023). High-throughput PRIME-editing screens identify functional DNA variants in the human genome. Mol. Cell *83*, 4633–4645.e9. https://doi.org/10.1016/j.molcel.2023.11.021.

33. Herger, M., Kajba, C.M., Buckley, M., Cunha, A., Strom, M., and Findlay, G.M. (2025). High-throughput screening of human genetic variants by pooled prime editing. Cell Genomics *5*, 100814. https://doi.org/10.1016/j.xgen.2025.100814.

34. Martyn, G.E., Montgomery, M.T., Jones, H., Guo, K., Doughty, B.R., Linder, J., Bisht, D., Xia, F., Cai, X.S., Chen, Z., et al. (2025). Rewriting regulatory DNA to dissect and reprogram gene expression. Cell *188*, 3349–3366.e23. https://doi.org/10.1016/j.cell.2025.03.034.

35. Montalbano, A., Canver, M.C., and Sanjana, N.E. (2017). High-Throughput Approaches to Pinpoint Function within the Noncoding Genome. Mol. Cell *68*, 44–59. https://doi.org/10.1016/j.molcel.2017.09.017.

36. Singh, A., Irfan, H., Fatima, E., Nazir, Z., Verma, A., and Akilimali, A. (2024). Revolutionary breakthrough: FDA approves CASGEVY, the first CRISPR/Cas9 gene therapy for sickle cell disease. Ann. Med. Surg. (Lond) *86*, 4555–4559. https://doi.org/10.1097/MS9.0000000000002146.

37. Dang, C.V. (2012). MYC on the Path to Cancer. Cell *149*, 22–35. https://doi.org/10.1016/j.cell.2012.03.003.

38. Madden, S.K., de Araujo, A.D., Gerhardt, M., Fairlie, D.P., and Mason, J.M. (2021). Taking the Myc out of cancer: toward therapeutic strategies to directly inhibit c-Myc. Mol. Cancer *20*, 3. https://doi.org/10.1186/s12943-020-01291-6.

39. Gabay, M., Li, Y., and Felsher, D.W. (2014). MYC Activation Is a Hallmark of Cancer Initiation and Maintenance. Cold Spring Harb. Perspect. Med. *4*, a014241. https://doi.org/10.1101/cshperspect.a014241.

40. Weinstein, I.B. (2002). Cancer. Addiction to oncogenes–the Achilles heal of cancer. Science *297*, 63–64. https://doi.org/10.1126/science.1073096.

41. Whitfield, J.R., and Soucek, L. (2025). MYC in cancer: from undruggable target to clinical trials. Nat. Rev. Drug Discov. *24*, 445–457. https://doi.org/10.1038/s41573-025-01143-2.

42. Wallbillich, N.J., and Lu, H. (2023). Role of c-Myc in lung cancer: Progress, challenges, and prospects. Chin. Med. J. Pulm. Crit. Care Med. *1*, 129–138. https://doi.org/10.1016/j.pccm.2023.07.001.

43. Walton, R.T., Christie, K.A., Whittaker, M.N., and Kleinstiver, B.P. (2020). Unconstrained genome targeting with near-PAMless engineered CRISPR-Cas9 variants. Science *368*, 290–296. https://doi.org/10.1126/science.aba8853.

44. Shou, Y., Martelli, M.L., Gabrea, A., Qi, Y., Brents, L.A., Roschke, A., Dewald, G., Kirsch, I.R., Bergsagel, P.L., and Kuehl, W.M. (2000). Diverse karyotypic abnormalities of the c-myc locus associated with c-myc dysregulation and tumor progression in multiple myeloma. Proc. Natl. Acad. Sci. USA *97*, 228–233. https://doi.org/10.1073/pnas.97.1.228.

45. Steinberger, J., Robert, F., Hallé, M., Williams, D.E., Cencic, R., Sawhney, N., Pelletier, D., Williams, P., Igarashi, Y., Porco, J.A., et al. (2019). Tracing MYC Expression for Small Molecule Discovery. Cell Chem. Biol. *26*, 699–710.e6. https://doi.org/10.1016/j.chembiol.2019.02.007.

46. Holien, T., Våtsveen, T.K., Hella, H., Waage, A., and Sundan, A. (2012). Addiction to c-MYC in multiple myeloma. Blood *120*, 2450–2453. https://doi.org/10.1182/blood-2011-08-371567.

47. Li, W., Xu, H., Xiao, T., Cong, L., Love, M.I., Zhang, F., Irizarry, R.A., Liu, J.S., Brown, M., and Liu, X.S. (2014). MAGeCK enables robust identification of essential genes from genome-scale CRISPR/Cas9 knockout screens. Genome Biol. *15*, 554. https://doi.org/10.1186/s13059-014-0554-4.

48. Munoz, D.M., Cassiani, P.J., Li, L., Billy, E., Korn, J.M., Jones, M.D., Golji, J., Ruddy, D.A., Yu, K., McAllister, G., et al. (2016). CRISPR Screens Provide a Comprehensive Assessment of Cancer Vulnerabilities but Generate False-Positive Hits for Highly Amplified Genomic Regions. Cancer Discov. *6*, 900–913. https://doi.org/10.1158/2159-8290.CD-16-0178.

Please cite this article in press as: Shi et al., CRISPR mutagenesis of the *MYC* locus reveals a druggable ultraconserved RNA element, Cell (2027), https://doi.org/10.1016/j.cell.2026.10.002

49. Jones, T.R., and Cole, M.D. (1987). Rapid Cytoplasmic Turnover of c-myc mRNA: Requirement of the 3′ Untranslated Sequences. Mol. Cell. Biol. *7*, 4513–4521. https://doi.org/10.1128/mcb.7.12.4513-4521.1987.

50. Doench, J.G., Fusi, N., Sullender, M., Hegde, M., Vaimberg, E.W., Donovan, K.F., Smith, I., Tothova, Z., Wilen, C., Orchard, R., et al. (2016). Optimized sgRNA design to maximize activity and minimize off-target effects of CRISPR-Cas9. Nat. Biotechnol. *34*, 184–191. https://doi.org/10.1038/nbt.3437.

51. Kim, H.K., Kim, Y., Lee, S., Min, S., Bae, J.Y., Choi, J.W., Park, J., Jung, D., Yoon, S., and Kim, H.H. (2019). SpCas9 activity prediction by DeepSpCas9, a deep learning-based model with high generalization performance. Sci. Adv. *5*, eaax9249. https://doi.org/10.1126/sciadv.aax9249.

52. Anthon, C., Corsi, G.I., and Gorodkin, J. (2022). CRISPRon/off: CRISPR/Cas9 on- and off-target gRNA design. Bioinformatics *38*, 5437–5439. https://doi.org/10.1093/bioinformatics/btac697.

53. Ren, Q., Sretenovic, S., Liu, S., Tang, X., Huang, L., He, Y., Liu, L., Guo, Y., Zhong, Z., Liu, G., et al. (2021). PAM-less plant genome editing using a CRISPR–SpRY toolbox. Nat. Plants *7*, 25–33. https://doi.org/10.1038/s41477-020-00827-4.

54. Shalem, O., Sanjana, N.E., Hartenian, E., Shi, X., Scott, D.A., Mikkelson, T.S., Heckl, D., Ebert, B.L., Root, D.E., Doench, J.G., et al. (2014). Genome-scale CRISPR-Cas9 knockout screening in human cells. Science *343*, 84–87. https://doi.org/10.1126/science.1247005.

55. Wang, T., Wei, J.J., Sabatini, D.M., and Lander, E.S. (2014). Genetic screens in human cells using the CRISPR-Cas9 system. Science *343*, 80–84. https://doi.org/10.1126/science.1246981.

56. ENCODE Project Consortium, Moore, J.E., Purcaro, M.J., Pratt, H.E., Epstein, C.B., Shoresh, N., Adrian, J., Kawli, T., Davis, C.A., Dobin, A., et al. (2020). Expanded encyclopaedias of DNA elements in the human and mouse genomes. Nature *583*, 699–710. https://doi.org/10.1038/s41586-020-2493-4.

57. Wisdom, R., and Lee, W. (1991). The protein-coding region of c-myc mRNA contains a sequence that specifies rapid mRNA turnover and induction by protein synthesis inhibitors. Genes Dev. *5*, 232–243. https://doi.org/10.1101/gad.5.2.232.

58. Kim, H.H., Kuwano, Y., Srikantan, S., Lee, E.K., Martindale, J.L., and Gorospe, M. (2009). HuR recruits let-7/RISC to repress c-Myc expression. Genes Dev. *23*, 1743–1748. https://doi.org/10.1101/gad.1812509.

59. Lujambio, A., Calin, G.A., Villanueva, A., Ropero, S., Sánchez-Céspedes, M., Blanco, D., Montuenga, L.M., Rossi, S., Nicoloso, M.S., Faller, W.J., et al. (2008). A microRNA DNA methylation signature for human cancer metastasis. Proc. Natl. Acad. Sci. USA *105*, 13556–13561. https://doi.org/10.1073/pnas.0803055105.

60. Hermeking, H. (2010). The miR-34 family in cancer and apoptosis. Cell Death Differ. *17*, 193–199. https://doi.org/10.1038/cdd.2009.56.

61. Schmidt, D., Wilson, M.D., Ballester, B., Schwalie, P.C., Brown, G.D., Marshall, A., Kutter, C., Watt, S., Martinez-Jimenez, C.P., Mackay, S., et al. (2010). Five-vertebrate ChIP-seq reveals the evolutionary dynamics of transcription factor binding. Science *328*, 1036–1040. https://doi.org/10.1126/science.1186176.

62. Phan, M.H.Q., Zehnder, T., Puntieri, F., Magg, A., Majchrzycka, B., Antonović, M., Wieler, H., Lo, B.-W., Baranasic, D., Lenhard, B., et al. (2025). Conservation of regulatory elements with highly diverged sequences across large evolutionary distances. Nat. Genet. *57*, 1524–1534. https://doi.org/10.1038/s41588-025-02202-5.

63. Halldorsson, B.V., Eggertsson, H.P., Moore, K.H.S., Hauswedell, H., Eiriksson, O., Ulfarsson, M.O., Palsson, G., Hardarson, M.T., Oddsson, A., Jensson, B.O., et al. (2022). The sequences of 150,119 genomes in the UK Biobank. Nature *607*, 732–740. https://doi.org/10.1038/s41586-022-04965-x.

64. Vitsios, D., Dhindsa, R.S., Middleton, L., Gussow, A.B., and Petrovski, S. (2021). Prioritizing non-coding regions based on human genomic constraint and sequence context with deep learning. Nat. Commun. *12*, 1504. https://doi.org/10.1038/s41467-021-21790-4.

65. Spicher, A., Guicherit, O.M., Duret, L., Aslanian, A., Sanjines, E.M., Denko, N.C., Giaccia, A.J., and Blau, H.M. (1998). Highly conserved RNA sequences that are sensors of environmental stress. Mol. Cell. Biol. *18*, 7371–7382. https://doi.org/10.1128/MCB.18.12.7371.

66. Duret, L., Dorkeld, F., and Gautier, C. (1993). Strong conservation of non-coding sequences during vertebrates evolution: potential involvement in post-transcriptional regulation of gene expression. Nucleic Acids Res. *21*, 2315–2322. https://doi.org/10.1093/nar/21.10.2315.

67. O'Leary, C.A., Andrews, R.J., Tompkins, V.S., Chen, J.L., Childs-Disney, J.L., Disney, M.D., and Moss, W.N. (2019). RNA structural analysis of the MYC mRNA reveals conserved motifs that affect gene expression. PLoS One *14*, e0213758. https://doi.org/10.1371/journal.pone.0213758.

68. Bae, S., Park, J., and Kim, J.-S. (2014). Cas-OFFinder: a fast and versatile algorithm that searches for potential off-target sites of Cas9 RNA-guided endonucleases. Bioinformatics *30*, 1473–1475. https://doi.org/10.1093/bioinformatics/btu048.

69. Scharner, J., Ma, W.K., Zhang, Q., Lin, K.-T., Rigo, F., Bennett, C.F., and Krainer, A.R. (2020). Hybridization-mediated off-target effects of splice-switching antisense oligonucleotides. Nucleic Acids Res. *48*, 802–816. https://doi.org/10.1093/nar/gkz1132.

70. Krüger, J., and Rehmsmeier, M. (2006). RNAhybrid: microRNA target prediction easy, fast and flexible. Nucleic Acids Res. *34*, W451–W454. https://doi.org/10.1093/nar/gkl243.

71. Lee, K.-M., Lin, C.-C., Servetto, A., Bae, J., Kandagatla, V., Ye, D., Kim, G., Sudhan, D.R., Mendiratta, S., González Ericsson, P.I., et al. (2022). Epigenetic repression of STING by MYC promotes immune evasion and resistance to immune checkpoint inhibitors in triple-negative breast cancer. Cancer Immunol. Res. *10*, 829–843. https://doi.org/10.1158/2326-6066.CIR-21-0826.

72. Love, M.I., Huber, W., and Anders, S. (2014). Moderated estimation of fold change and dispersion for RNA-seq data with DESeq2. Genome Biol. *15*, 550. https://doi.org/10.1186/s13059-014-0550-8.

73. Liberzon, A., Birger, C., Thorvaldsdóttir, H., Ghandi, M., Mesirov, J.P., and Tamayo, P. (2015). The Molecular Signatures Database (MSigDB) Hallmark Gene Set Collection. Cell Syst. *1*, 417–425. https://doi.org/10.1016/j.cels.2015.12.004.

74. Lun, A.T.L., and Smyth, G.K. (2016). csaw: a Bioconductor package for differential binding analysis of ChIP-seq data using sliding windows. Nucleic Acids Res. *44*, e45. https://doi.org/10.1093/nar/gkv1191.

75. Jakobsen, S.T., Jensen, R.A.M., Madsen, M.S., Ravnsborg, T., Vaagenso, C.S., Siersbæk, M.S., Einarsson, H., Andersson, R., Jensen, O.N., and Siersbæk, R. (2024). MYC activity at enhancers drives prognostic transcriptional programs through an epigenetic switch. Nat. Genet. *56*, 663–674. https://doi.org/10.1038/s41588-024-01676-z.

76. Linstra, R., Stappenbelt, C., Bakker, F.J., Everts, M., Bhattacharya, A., Yu, S., van Bergen, S.D., van der Vegt, B., Wisman, G.B.A., Fehrmann, R.S.N., et al. (2025). MYC controls STING levels to downregulate inflammatory signaling in breast cancer cells upon DNA damage. J. Biol. Chem. *301*, 108560. https://doi.org/10.1016/j.jbc.2025.108560.

77. Krenz, B., Gebhardt-Wolf, A., Ade, C.P., Gaballa, A., Roehrig, F., Vendelova, E., Baluapuri, A., Eilers, U., Gallant, P., D'Artista, L., et al. (2021). MYC- and MIZ1-Dependent Vesicular Transport of Double-Strand RNA Controls Immune Evasion in Pancreatic Ductal Adenocarcinoma. Cancer Res. *81*, 4242–4256. https://doi.org/10.1158/0008-5472.CAN-21-1677.

78. Uhl, L., Aziba, A., Löbbert, S., Russell, T., Krenz, B., Montesinos, F., Kannan, T., Valanju, O.R., Schülein-Völk, C., de Martines, T., et al. (2026). MYC binding to nascent RNA suppresses innate immune signaling by R-loop-derived RNA-DNA hybrids. Cell *189*, 1371–1388.e29. https://doi.org/10.1016/j.cell.2025.12.019.

79. Chitrakar, A., Solorio-Kirpichyan, K., Prangley, E., Rath, S., Du, J., and Korennykh, A. (2021). Introns encode dsRNAs undetected by RIG-I/

Please cite this article in press as: Shi et al., CRISPR mutagenesis of the *MYC* locus reveals a druggable ultraconserved RNA element, Cell (2027), https://doi.org/10.1016/j.cell.2026.10.002

MDA5/interferons and sensed via RNase L. Proc. Natl. Acad. Sci. USA *118*, e2102134118. https://doi.org/10.1073/pnas.2102134118.

80. Luo, Y., Zhong, Y., Basu, S., Wu, M.-C., and Mayr, C. (2026). mRNA 3′ UTRs chaperone intrinsically disordered regions to control protein activity. Cell *189*, 4619–4636.e16. https://doi.org/10.1016/j.cell.2026.05.017.
81. Lin, L., Chuang, K.-H., and Dai, C. (2026). c-MYC is an aggregation-prone, amyloidogenic protein. Preprint at bioRxiv. https://doi.org/10.64898/2026.03.12.711438.
82. Dalgleish, G.D., Veyrune, J.L., Accornero, N., Blanchard, J.M., and Hesketh, J.E. (1999). Localisation of a reporter transcript by the c-myc 3′-UTR is linked to translation. Nucleic Acids Res. *27*, 4363–4368. https://doi.org/10.1093/nar/27.22.4363.
83. Dang, C.V., and Lee, W.M. (1988). Identification of the human c-myc protein nuclear translocation signal. Mol. Cell. Biol. *8*, 4048–4054. https://doi.org/10.1128/mcb.8.10.4048-4054.1988.
84. Ray, M., Tang, R., Jiang, Z., and Rotello, V.M. (2015). Quantitative tracking of protein trafficking to the nucleus using cytosolic protein delivery by nanoparticle-stabilized nanocapsules. Bioconjug. Chem. *26*, 1004–1007. https://doi.org/10.1021/acs.bioconjchem.5b00141.
85. Van Nostrand, E.L., Freese, P., Pratt, G.A., Wang, X., Wei, X., Xiao, R., Blue, S.M., Chen, J.-Y., Cody, N.A.L., Dominguez, D., et al. (2020). A large-scale binding and functional map of human RNA-binding proteins. Nature *583*, 711–719. https://doi.org/10.1038/s41586-020-2077-3.
86. Hui, J., Hung, L.H., Heiner, M., Schreiner, S., Neumüller, N., Reither, G., Haas, S.A., and Bindereif, A. (2005). Intronic CA-repeat and CA-rich elements: a new class of regulators of mammalian alternative splicing. EMBO J. *24*, 1988–1998. https://doi.org/10.1038/sj.emboj.7600677.
87. Jafarifar, F., Yao, P., Eswarappa, S.M., and Fox, P.L. (2011). Repression of VEGFA by CA-rich element-binding microRNAs is modulated by hnRNP L. EMBO J. *30*, 1324–1334. https://doi.org/10.1038/emboj.2011.38.
88. Venkata Subbaiah, K.C., Wu, J., Potdar, A., and Yao, P. (2019). hnRNP L-mediated RNA switches function as a hypoxia-induced translational regulon. Biochem. Biophys. Res. Commun. *516*, 753–759. https://doi.org/10.1016/j.bbrc.2019.06.106.
89. Ray, P.S., Jia, J., Yao, P., Majumder, M., Hatzoglou, M., and Fox, P.L. (2009). A stress-responsive RNA switch regulates VEGFA expression. Nature *457*, 915–919. https://doi.org/10.1038/nature07598.
90. Rossbach, O., Hung, L.-H., Khrameeva, E., Schreiner, S., König, J., Curk, T., Zupan, B., Ule, J., Gelfand, M.S., and Bindereif, A. (2014). Crosslinking-immunoprecipitation (iCLIP) analysis reveals global regulatory roles of hnRNP L. RNA Biol. *11*, 146–155. https://doi.org/10.4161/rna.27991.
91. Matsui, K., Nishizawa, M., Ozaki, T., Kimura, T., Hashimoto, I., Yamada, M., Kaibori, M., Kamiyama, Y., Ito, S., and Okumura, T. (2008). Natural antisense transcript stabilizes inducible nitric oxide synthase messenger RNA in rat hepatocytes. Hepatology *47*, 686–697. https://doi.org/10.1002/hep.22036.
92. Shankarling, G., Cole, B.S., Mallory, M.J., and Lynch, K.W. (2014). Transcriptome-wide RNA interaction profiling reveals physical and functional targets of hnRNP L in human T cells. Mol. Cell. Biol. *34*, 71–83. https://doi.org/10.1128/MCB.00740-13.
93. Karakasheva, T.A., Gabre, J.T., Sachdeva, U.M., Cruz-Acuña, R., Lin, E.W., DeMarshall, M., Falk, G.W., Ginsberg, G.G., Yang, Z., Kim, M.M., et al. (2021). Patient-derived organoids as a platform for modeling a patient's response to chemoradiotherapy in esophageal cancer. Sci. Rep. *11*, 21304. https://doi.org/10.1038/s41598-021-00706-8.
94. Vlachogiannis, G., Hedayat, S., Vatsiou, A., Jamin, Y., Fernández-Mateos, J., Khan, K., Lampis, A., Eason, K., Huntingford, I., Burke, R., et al. (2018). Patient-derived organoids model treatment response of metastatic gastrointestinal cancers. Science *359*, 920–926. https://doi.org/10.1126/science.aao2774.
95. Logun, M., Wang, X., Sun, Y., Bagley, S.J., Li, N., Desai, A., Zhang, D.Y., Nasrallah, M.P., Pai, E.L.-L., Oner, B.S., et al. (2025). Patient-derived glioblastoma organoids as real-time avatars for assessing responses to clinical CAR-T cell therapy. Cell Stem Cell *32*, 181–190.e4. https://doi.org/10.1016/j.stem.2024.11.010.
96. Dayton, T.L., Alcala, N., Moonen, L., den Hartigh, L., Geurts, V., Mangiante, L., Lap, L., Dost, A.F.M., Beumer, J., Levy, S., et al. (2023). Druggable growth dependencies and tumor evolution analysis in patient-derived organoids of neuroendocrine neoplasms from multiple body sites. Cancer Cell *41*, 2083–2099.e9. https://doi.org/10.1016/j.ccell.2023.11.007.
97. Lee, S.H., Hu, W., Matulay, J.T., Silva, M.V., Owczarek, T.B., Kim, K., Chua, C.W., Barlow, L.J., Kandoth, C., Williams, A.B., et al. (2018). Tumor Evolution and Drug Response in Patient-Derived Organoid Models of Bladder Cancer. Cell *173*, 515–528.e17. https://doi.org/10.1016/j.cell.2018.03.017.
98. Zhao, Y., Li, S., Zhu, L., Huang, M., Xie, Y., Song, X., Chen, Z., Lau, H.C.-H., Sung, J.J.-Y., Xu, L., et al. (2024). Personalized drug screening using patient-derived organoid and its clinical relevance in gastric cancer. Cell Rep. Med. *5*, 101627. https://doi.org/10.1016/j.xcrm.2024.101627.
99. Romero, J.M., Magrill, J., Kalashnikov, N., Luo, Y.Z., Chen, O.J., Busque, S., Ma, R., Atallah, A., Lazaratos, A.-M., Mendelson, D., et al. (2026). Comparative analysis of patient-derived organoids and patient-derived xenografts as avatar models for predicting response to anti-cancer therapy. Cancer Treat. Rev. *149*, 103190. https://doi.org/10.1016/j.ctrv.2026.103190.
100. Levadoux, M., Mahon, C., Beattie, J.H., Wallace, H.M., and Hesketh, J.E. (1999). Nuclear Import of Metallothionein Requires Its mRNA to Be Associated with the Perinuclear Cytoskeleton. J. Biol. Chem. *274*, 34961–34966. https://doi.org/10.1074/jbc.274.49.34961.
101. Ma, W., and Mayr, C. (2018). A Membraneless Organelle Associated with the Endoplasmic Reticulum Enables 3′UTR-Mediated Protein-Protein Interactions. Cell *175*, 1492–1506.e19. https://doi.org/10.1016/j.cell.2018.10.007.
102. Luo, Y., Pratihar, S., Horste, E.H., Mitschka, S., Mey, A.S.J.S., Al-Hashimi, H.M., and Mayr, C. (2023). mRNA interactions with disordered regions control protein activity. Preprint at bioRxiv. https://doi.org/10.1101/2023.02.18.529068.
103. Hofman, C.R., and Corey, D.R. (2024). Targeting RNA with synthetic oligonucleotides: Clinical success invites new challenges. Cell Chem. Biol. *31*, 125–138. https://doi.org/10.1016/j.chembiol.2023.09.005.
104. Crooke, S.T., Baker, B.F., Crooke, R.M., and Liang, X.H. (2021). Antisense technology: an overview and prospectus. Nat. Rev. Drug Discov. *20*, 427–453. https://doi.org/10.1038/s41573-021-00162-z.
105. Leonetti, C., Biroccio, A., Benassi, B., Stringaro, A., Stoppacciaro, A., Semple, S.C., and Zupi, G. (2001). Encapsulation of c-myc antisense oligodeoxynucleotides in lipid particles improves antitumoral efficacy in vivo in a human melanoma line. Cancer Gene Ther. *8*, 459–468. https://doi.org/10.1038/sj.cgt.7700326.
106. Gill, T., Wang, H., Bandaru, R., Lawlor, M., Lu, C., Nieman, L.T., Tao, J., Zhang, Y., Anderson, D.G., Ting, D.T., et al. (2021). Selective targeting of MYC mRNA by stabilized antisense oligonucleotides. Oncogene *40*, 6527–6539. https://doi.org/10.1038/s41388-021-02053-4.
107. Shen, W., De Hoyos, C.L., Migawa, M.T., Vickers, T.A., Sun, H., Low, A., Bell, T.A., Rahdar, M., Mukhopadhyay, S., Hart, C.E., et al. (2019). Chemical modification of PS-ASO therapeutics reduces cellular protein-binding and improves the therapeutic index. Nat. Biotechnol. *37*, 640–650. https://doi.org/10.1038/s41587-019-0106-2.
108. Yoshida, T., Hagihara, T., Uchida, Y., Horiuchi, Y., Sasaki, K., Yamamoto, T., Yamashita, T., Goda, Y., Saito, Y., Yamaguchi, T., et al. (2024). Introduction of sugar-modified nucleotides into CpG-containing antisense oligonucleotides inhibits TLR9 activation. Sci. Rep. *14*, 11540. https://doi.org/10.1038/s41598-024-61666-3.
109. El Boujnouni, N., van der Bent, M.L., Willemse, M., 't Hoen, P.A.C., Brock, R., and Wansink, D.G. (2023). Block or degrade? Balancing on- and off-target effects of antisense strategies against transcripts with expanded

Please cite this article in press as: Shi et al., CRISPR mutagenesis of the *MYC* locus reveals a druggable ultraconserved RNA element, Cell (2027), https://doi.org/10.1016/j.cell.2026.10.002

triplet repeats in DM1. Mol. Ther. Nucleic Acids *32*, 622–636. https://doi.org/10.1016/j.omtn.2023.04.010.

110. Garralda, E., Beaulieu, M.-E., Moreno, V., Casacuberta-Serra, S., Martínez-Martín, S., Foradada, L., Alonso, G., Massó-Vallés, D., López-Estévez, S., Jauset, T., et al. (2024). MYC targeting by OMO-103 in solid tumors: a phase 1 trial. Nat. Med. *30*, 762–771. https://doi.org/10.1038/s41591-024-02805-1.

111. Nevzorova, Y.A., and Cubero, F.J. (2023). Obesity under the moonlight of c-MYC. Front. Cell Dev. Biol. *11*, 1293218. https://doi.org/10.3389/fcell.2023.1293218.

112. Wolfram, J.A., Lesnefsky, E.J., Hoit, B.D., Smith, M.A., and Lee, H.G. (2011). Therapeutic Potential of c-Myc Inhibition in the Treatment of Hypertrophic Cardiomyopathy. Ther. Adv. Chronic Dis. *2*, 133–144. https://doi.org/10.1177/2040622310393059.

113. Ahuja, P., Zhao, P., Angelis, E., Ruan, H., Korge, P., Olson, A., Wang, Y., Jin, E.S., Jeffrey, F.M., Portman, M., et al. (2010). Myc controls transcriptional regulation of cardiac metabolism and mitochondrial biogenesis in response to pathological stress in mice. J. Clin. Invest. *120*, 1494–1505. https://doi.org/10.1172/JCI38331.

114. Komuro, J., Hashimoto, H., Katsuki, T., Kusumoto, D., Katoh, M., Ko, T., Ito, M., Katagiri, M., Kubota, M., Yamada, S., et al. (2025). Heart failure-specific cardiac fibroblasts contribute to cardiac dysfunction via the MYC–CXCL1-CXCR2 axis. Nat. Cardiovasc. Res. *4*, 1135–1151. https://doi.org/10.1038/s44161-025-00698-y.

115. Colombo, E., Di Dario, M., Menon, R., Valente, M.M., Bassani, C., Sarno, N., Mazza, D., Montini, F., Moiola, L., Comi, G., et al. (2023). HNF4α, SP1 and c-myc are master regulators of CNS autoimmunity. J. Autoimmun. *138*, 103053. https://doi.org/10.1016/j.jaut.2023.103053.

116. Trop-Steinberg, S., and Azar, Y. (2018). Is Myc an Important Biomarker? Myc Expression in Immune Disorders and Cancer. Am. J. Med. Sci. *355*, 67–75. https://doi.org/10.1016/j.amjms.2017.06.007.

117. Marinkovic, T., and Marinkovic, D. (2021). Obscure Involvement of MYC in Neurodegenerative Diseases and Neuronal Repair. Mol. Neurobiol. *58*, 4169–4177. https://doi.org/10.1007/s12035-021-02406-w.

118. Zacarías-Fluck, M.F., Soucek, L., and Whitfield, J.R. (2024). MYC: there is more to it than cancer. Front. Cell Dev. Biol. *12*, 1342872. https://doi.org/10.3389/fcell.2024.1342872.

119. Zetsche, B., Gootenberg, J.S., Abudayyeh, O.O., Slaymaker, I.M., Makarova, K.S., Essletzbichler, P., Volz, S.E., Joung, J., van der Oost, J., Regev, A., et al. (2015). Cpf1 is a single RNA-guided endonuclease of a class 2 CRISPR-Cas system. Cell *163*, 759–771. https://doi.org/10.1016/j.cell.2015.09.038.

120. Tarumoto, Y., Lu, B., Somerville, T.D.D., Huang, Y.-H., Milazzo, J.P., Wu, X.S., Klingbeil, O., El Demerdash, O., Shi, J., and Vakoc, C.R. (2018). LKB1, Salt-Inducible Kinases, and MEF2C Are Linked Dependencies in Acute Myeloid Leukemia. Mol. Cell *69*, 1017–1027.e6. https://doi.org/10.1016/j.molcel.2018.02.011.

121. Huang, T.P., Heins, Z.J., Miller, S.M., Wong, B.G., Balivada, P.A., Wang, T., Khalil, A.S., and Liu, D.R. (2023). High-throughput continuous evolution of compact Cas9 variants targeting single-nucleotide-pyrimidine PAMs. Nat. Biotechnol. *41*, 96–107. https://doi.org/10.1038/s41587-022-01410-2.

122. Savell, K.E., Bach, S.V., Zipperly, M.E., Revanna, J.S., Goska, N.A., Tuscher, J.J., Duke, C.G., Sultan, F.A., Burke, J.N., Williams, D., et al. (2019). A Neuron-Optimized CRISPR/dCas9 Activation System for Robust and Specific Gene Regulation. eNeuro *6*. ENEURO.0495-18.2019. https://doi.org/10.1523/ENEURO.0495-18.2019.

123. Matsuda, T., and Cepko, C.L. (2004). Electroporation and RNA interference in the rodent retina in vivo and in vitro. Proc. Natl. Acad. Sci. USA *101*, 16–22. https://doi.org/10.1073/pnas.2235688100.

124. McLaren, W., Gil, L., Hunt, S.E., Riat, H.S., Ritchie, G.R.S., Thormann, A., Flicek, P., and Cunningham, F. (2016). The Ensembl Variant Effect Predictor. Genome Biol. *17*, 122. https://doi.org/10.1186/s13059-016-0974-4.

125. Langmead, B., Trapnell, C., Pop, M., and Salzberg, S.L. (2009). Ultrafast and memory-efficient alignment of short DNA sequences to the human genome. Genome Biol. *10*, R25. https://doi.org/10.1186/gb-2009-10-3-r25.

126. Chen, S., Zhou, Y., Chen, Y., and Gu, J. (2018). fastp: an ultra-fast all-in-one FASTQ preprocessor. Bioinformatics *34*, i884–i890. https://doi.org/10.1093/bioinformatics/bty560.

127. Dobin, A., Davis, C.A., Schlesinger, F., Drenkow, J., Zaleski, C., Jha, S., Batut, P., Chaisson, M., and Gingeras, T.R. (2013). STAR: ultrafast universal RNA-seq aligner. Bioinformatics *29*, 15–21. https://doi.org/10.1093/bioinformatics/bts635.

128. Liao, Y., Smyth, G.K., and Shi, W. (2014). featureCounts: an efficient general purpose program for assigning sequence reads to genomic features. Bioinformatics *30*, 923–930. https://doi.org/10.1093/bioinformatics/btt656.

129. Ramírez, F., Ryan, D.P., Grüning, B., Bhardwaj, V., Kilpert, F., Richter, A.S., Heyne, S., Dündar, F., and Manke, T. (2016). deepTools2: a next generation web server for deep-sequencing data analysis. Nucleic Acids Res. *44*, W160–W165. https://doi.org/10.1093/nar/gkw257.

130. Yu, G., Wang, L.-G., Han, Y., and He, Q.-Y. (2012). clusterProfiler: an R package for comparing biological themes among gene clusters. OMICS *16*, 284–287. https://doi.org/10.1089/omi.2011.0118.

131. Li, H. (2013). Aligning sequence reads, clone sequences and assembly contigs with BWA-MEM. Preprint at arXiv. https://doi.org/10.48550/arXiv.1303.3997.

132. Doherty, P., Hu, Q., Zhuang, Z., Zhang, H., Penikalapati, S.C., Liu, S., and Liu, T. (2026). MACS3: A Peak-calling Platform for Bulk and Single-cell Regulatory Genomics. Genomics Proteomics Bioinformatics, qzag097. Published online September 16, 2026. https://doi.org/10.1093/gpbjnl/qzag097.

133. Robinson, M.D., McCarthy, D.J., and Smyth, G.K. (2010). edgeR: a Bioconductor package for differential expression analysis of digital gene expression data. Bioinformatics *26*, 139–140. https://doi.org/10.1093/bioinformatics/btp616.

134. Clement, K., Rees, H., Canver, M.C., Gehrke, J.M., Farouni, R., Hsu, J.Y., Cole, M.A., Liu, D.R., Joung, J.K., Bauer, D.E., et al. (2019). CRISPResso2 provides accurate and rapid genome editing sequence analysis. Nat. Biotechnol. *37*, 224–226. https://doi.org/10.1038/s41587-019-0032-3.

135. FNU, T., Shi, P., Zhang, W., Fang, Y., Mitani, Y., Zhang, Y., Gabre, J., Ei-Rifai, W., Zaika, A., Chen, Q., et al. (2025). The SOX4-Semaphorin3C axis promotes esophageal adenocarcinoma progression. Cancer Lett. *633*, 218005. https://doi.org/10.1016/j.canlet.2025.218005.

136. McFarlane, G.R., Polanco, J.V.C., and Bogema, D. (2024). CRISPR-Cas guide RNA indel analysis using CRISPResso2 with Nanopore sequencing data. BMC Res. Notes *17*, 205. https://doi.org/10.1186/s13104-024-06861-1.

137. Schwanhäusser, B., Busse, D., Li, N., Dittmar, G., Schuchhardt, J., Wolf, J., Chen, W., and Selbach, M. (2011). Global quantification of mammalian gene expression control. Nature *473*, 337–342. https://doi.org/10.1038/nature10098.

138. Weyn-Vanhentenryck, S.M., Mele, A., Yan, Q., Sun, S., Farny, N., Zhang, Z., Xue, C., Herre, M., Silver, P.A., Zhang, M.Q., et al. (2014). HITS-CLIP and integrative modeling define the Rbfox splicing-regulatory network linked to brain development and autism. Cell Rep. *6*, 1139–1152. https://doi.org/10.1016/j.celrep.2014.02.005.

139. Smit, A., Hubley, R., and Green, P. (2013–2015). RepeatMasker Open-4.0. http://www.repeatmasker.org.

140. Siepel, A., Bejerano, G., Pedersen, J.S., Hinrichs, A.S., Hou, M., Rosenbloom, K., Clawson, H., Spieth, J., Hillier, L.W., Richards, S., et al. (2005). Evolutionarily conserved elements in vertebrate, insect, worm, and yeast genomes. Genome Res. *15*, 1034–1050. https://doi.org/10.1101/gr.3715005.

141. Morales, J., Pujar, S., Loveland, J.E., Astashyn, A., Bennett, R., Berry, A., Cox, E., Davidson, C., Ermolaeva, O., Farrell, C.M., et al. (2022). A joint NCBI and EMBL-EBI transcript set for clinical genomics and research. Nature *604*, 310–315. https://doi.org/10.1038/s41586-022-04558-8.

142. Agarwal, V., and Kelley, D.R. (2022). The genetic and biochemical determinants of mRNA degradation rates in mammals. Genome Biol. *23*, 245. https://doi.org/10.1186/s13059-022-02811-x.

143. Pollard, K.S., Hubisz, M.J., Rosenbloom, K.R., and Siepel, A. (2010). Detection of nonneutral substitution rates on mammalian phylogenies. Genome Res. *20*, 110–121. https://doi.org/10.1101/gr.097857.109.

144. Perez, G., Barber, G.P., Benet-Pages, A., Casper, J., Clawson, H., Diekhans, M., Fischer, C., Gonzalez, J.N., Hinrichs, A.S., Lee, C.M., et al. (2025). The UCSC Genome Browser database: 2025 update. Nucleic Acids Res. *53*, D1243–D1249. https://doi.org/10.1093/nar/gkae974.

145. Amemiya, H.M., Kundaje, A., and Boyle, A.P. (2019). The ENCODE Blacklist: Identification of Problematic Regions of the Genome. Sci. Rep. *9*, 9354. https://doi.org/10.1038/s41598-019-45839-z.

Please cite this article in press as: Shi et al., CRISPR mutagenesis of the *MYC* locus reveals a druggable ultraconserved RNA element, Cell (2027), https://doi.org/10.1016/j.cell.2026.10.002

STAR★METHODS

KEY RESOURCES TABLE

REAGENT or RESOURCE	SOURCE	IDENTIFIER
Antibodies		
Anti-MYC antibody	Santa Cruz Biotechnology	Cat#sc-40; RRID: AB_627268
Anti-MYC antibody	Cell Signaling Technology	Cat#5605T; RRID: AB_1903938
Anti-MYC antibody	Invitrogen	Cat#MA5-42675; RRID: AB_2911816
Anti-MYC antibody, HRP conjugate	Invitrogen	Cat#MA1-980-HRP; RRID: AB_2537628
Anti-MYC antibody	Abcam	Cat#ab32072; RRID: AB_731658
Anti-Vinculin antibody	Cell Signaling Technology	Cat#13901; RRID: AB_2728768
Anti-LC3 antibody	Proteintech	Cat#14600-1-AP; RRID: AB_2137737
Anti-STING antibody	Cell Signaling Technology	Cat#50494; RRID: AB_2799375
Anti-Phospho-STING (Ser366) antibody	Cell Signaling Technology	Cat#19781T; RRID: AB_2737062
Anti-TBK1 antibody	Cell Signaling Technology	Cat#3504T; RRID: AB_2255663
Anti-Phospho-TBK1 (Ser172) antibody	Cell Signaling Technology	Cat#5483T; RRID: AB_10693472
Anti-HA antibody	Thermo Fisher Scientific	Cat#26183; RRID: AB_10978021
Anti-hnRNP L antibody	Santa Cruz Biotechnology	Cat#sc-32317; RRID: AB_627736
Anti-BrdU antibody	MilliporeSigma	Cat# MAB3222; RRID: AB_94758
Anti-GAPDH antibody	Cell Signaling Technology	Cat#97166; RRID: AB_2756824
Anti-Vimentin antibody	Abcam	Cat#ab92547; RRID: AB_10562134
Anti-U1 snRNP 70 antibody	Santa Cruz Biotechnology	Cat#sc-390899; RRID: AB_2801569
Goat anti-rabbit IgG (H+L), Cy3 conjugate	Thermo Fisher Scientific	Cat#A10520; RRID: AB_10563288
Goat anti-mouse IgG (H+L), Cy3 conjugate	Thermo Fisher Scientific	Cat#M30010; RRID: AB_11181146
Goat anti-mouse IgG (H+L), Alexa Fluor 488 conjugate	Thermo Fisher Scientific	Cat#A28175; RRID: AB_2536161
Bacterial and virus strains		
NEB Stable Competent *E. coli*	New England Biolabs	Cat#C3040H
Endura electrocompetent cells	Lucigen	Cat#60242-1
HF1-SpRY-Cas9 lentivirus	This paper	N/A
lentiU6-sgRNA/EF1a-mCherry sgRNA-library lentivirus	This paper	N/A
HF1-SpRY-ABE8e lentivirus	This paper	N/A
lentiU6-sgRNA/EF1a-mCherry for individual sgRNA lentivirus	This paper	N/A
Biological samples		
Human esophageal adenocarcinoma patient-derived organoid: EACorg000	Columbia University Digestive & Liver Disease Research Core	N/A
Human head and neck cancer patient-derived organoid: HSC10	Columbia University Digestive & Liver Disease Research Core	N/A
Chemicals, peptides, and recombinant proteins		
Lipofectamine 3000 Transfection Reagent	Thermo Fisher Scientific	Cat#L3000015
Lipofectamine RNAiMAX Transfection Reagent	Invitrogen	Cat#13778
Opti-MEM I Reduced-Serum Medium	Gibco	Cat#31985062
Lenti-X Concentrator	Takara Bio	Cat#631231
WST-1 Cell Proliferation Reagent	Sigma-Aldrich	Cat#11644807001
RIPA Buffer	Sigma-Aldrich	Cat#R0278
Protease inhibitor cocktail	Roche	Cat#4693132001
NuPAGE LDS Sample Buffer (4×)	Invitrogen	Cat#NP0007

(*Continued on next page*)

Please cite this article in press as: Shi et al., CRISPR mutagenesis of the *MYC* locus reveals a druggable ultraconserved RNA element, Cell (2027), https://doi.org/10.1016/j.cell.2026.10.002

Continued

REAGENT or RESOURCE	SOURCE	IDENTIFIER
NuPAGE Reducing Agent (10×)	Invitrogen	Cat#NP0004
NuPAGE MOPS SDS Running Buffer	Invitrogen	Cat#NP0001
Tris-glycine transfer buffer	Invitrogen	Cat#LC3675
Ponceau S solution	Cell Signaling Technology	Cat#59803S
SuperSignal West Pico PLUS chemiluminescent substrate	Thermo Fisher Scientific	Cat#34580
10% neutral buffered formalin	Sigma-Aldrich	Cat#HT501128
Opal 690 fluorophore	Akoya Biosciences	Cat#FP1497001KT
Opal 650 fluorophore	Akoya Biosciences	Cat#FP1496001KT
Opal 570 fluorophore	Akoya Biosciences	Cat#FP1488001KT
Cell Staining Buffer	BioLegend	Cat#420201
Annexin V Binding Buffer	BioLegend	Cat#422201
APC Annexin V Apoptosis Detection Kit with 7-AAD	BioLegend	Cat#640930
RNase A	Thermo Fisher Scientific	Cat#EN0531
Calf Intestinal Alkaline Phosphatase	Promega	Cat#M2825
T4 RNA Ligase 2, truncated KQ	New England Biolabs	Cat#M0373L
RNasin Plus RNase Inhibitor	Promega	Cat#N2611
T4 Polynucleotide Kinase	New England Biolabs	Cat#M0201L
[γ-^{32}P]-ATP	PerkinElmer	Cat#BLU502A
Proteinase K	New England Biolabs	Cat#P8107S
Acid phenol	Sigma-Aldrich	Cat#P4682
Chloroform:isoamyl alcohol, 49:1	Sigma-Aldrich	Cat#25668
Glycogen	Invitrogen	Cat#AM9510
SuperScript III Reverse Transcriptase	Invitrogen	Cat#18080093
BrdUTP	Sigma-Aldrich	Cat#B0631
RNase H	Invitrogen	Cat#18021071
50× Denhardt's solution	MilliporeSigma	Cat#D2532
CircLigase II ssDNA Ligase	Fisher Scientific	Cat#NC9869616
KAPA HiFi HotStart DNA Polymerase	Roche	Cat#KK2501
SYBR Green I nucleic acid gel stain	Invitrogen	Cat#S7563
TrypLE™ Express	Thermo Fisher Scientific	Cat#12604013
Matrigel	Corning	Cat#356231
Critical commercial assays		
MycoAlert Mycoplasma Detection Kit	Lonza	Cat#LT07-418
Gibson Assembly Master Mix	New England Biolabs	Cat#E2611S
Phusion High-Fidelity DNA Polymerase Kit	New England Biolabs	Cat#E0553
Q5 Site-Directed Mutagenesis Kit	New England Biolabs	Cat#E0554S
BbsI-HF	New England Biolabs	Cat#R3539S
T4 DNA ligase	New England Biolabs	Cat#M0202T
Gel and PCR Clean-up Kit	Macherey-Nagel	Cat#740609
NucleoSpin Plasmid Transfection-grade Kit	Macherey-Nagel	Cat#740490
Platinum SuperFi II DNA Polymerase	Invitrogen	Cat#12361010
GeneArt Seamless Cloning and Assembly Enzyme Mix	Invitrogen	Cat#A14606
KAPA HiFi HotStart PCR Kit	Kapa Biosystems	Cat#KK2502
NEBuilder HiFi DNA Assembly Master Mix	New England Biolabs	Cat#E2621S
NucleoSpin Plasmid Maxi Kit	Macherey-Nagel	Cat#740414.50
NucleoSpin Tissue Kit	Macherey-Nagel	Cat#740952.50
KAPA Library Quantification Kit	Roche	Cat#07960336001

(*Continued on next page*)

Please cite this article in press as: Shi et al., CRISPR mutagenesis of the *MYC* locus reveals a druggable ultraconserved RNA element, Cell (2027), https://doi.org/10.1016/j.cell.2026.10.002

Continued

REAGENT or RESOURCE	SOURCE	IDENTIFIER
Q5 High-Fidelity 2× Master Mix	New England Biolabs	Cat#M0492S
NucleoSpin RNA Plus Kit	Macherey-Nagel	Cat#740984.250
SuperScript IV Reverse Transcriptase	Invitrogen	Cat#18090050
SYBR Green Master Mix	Applied Biosystems	Cat#A25741
BCA Protein Assay Kit	Thermo Fisher Scientific	Cat#23225
Image-iT Fixation/Permeabilization Kit	Thermo Fisher Scientific	Cat#A5818101
Direct-zol RNA Miniprep kit	Zymo Research	Cat#R2052
RNAscope Multiplex Fluorescent Reagent Kit v2	ACD Bio	Cat#323110
Subcellular Protein Fractionation Kit for Cultured Cells	Thermo Fisher Scientific	Cat#78840
Magna RIP RNA-Binding Protein Immunoprecipitation Kit	MilliporeSigma	Cat#17-700
Protein G Dynabeads	Thermo Fisher Scientific	Cat#10004D
NuPAGE 4%–12% Bis-Tris protein gels	Invitrogen	Cat#NP0321BOX
Nitrocellulose membrane	MilliporeSigma	Cat#GE10600013
NuPAGE Transfer Buffer	Invitrogen	Cat#NP0006
MicroSpin G-25 columns	Cytiva	Cat#27-5325-01
AMPure XP beads	Beckman Coulter	Cat#A63881
SimpleChIP Enzymatic Chromatin IP Kit	Cell Signaling Technology	Cat#9003
Drosophila chromatin	Active Motif	Cat#53083
Deposited data		
MYC SpRY-Cas9 screening data	This paper	GEO: GSE317040
MYC ASO RNA-Seq data	This paper	GEO: GSE317096
siHNRNPL RNA-Seq data	This paper	GEO: GSE317096
siMYC RNA-Seq data	This paper	GEO: GSE317096
MYC ASO and 8-nucleotide-deletion ChIP-Seq data	This paper	GEO: GSE317096
Analysis scripts	This paper	Github: https://github.com/FeiyueYang01/MYC-SpRY-Screening Zenodo DOI: 10.5281/zenodo.22943190
RPS19 SpRY-Cas9 screening data	Yao et al.[19]	NCBI SRA BioProject accessions: PRJNA1051298
STING1 re-expression RNA-Seq data	Lee et al.[71]	GEO: GSE196325
Experimental models: Cell lines		
Human: HEK293T cells	ATCC	Cat#CRL-3216
Human: MDA-MB-231 cells	ATCC	Cat#HTB-26
Human: NCI-H2171 cells	ATCC	Cat#CRL-5929
Human: JJN-3 cells	Jerry Pelletier laboratory	N/A
Human: D11 cells: JJN-3 derivative with one MYC allele carrying a C-terminal 2A-d2GFP knock-in	Jerry Pelletier laboratory	N/A
Human: U87MG cells	Peter A. Sims laboratory	N/A
Human: U2OS cells	ATCC	Cat#HTB-96
Human: D11 HF1-SpRY-Cas9 stable cells	This paper	N/A
Human: D11 HF1-SpRY-Cas9 cells expressing sg723 or sgCtrl	This paper	N/A
Human: MDA-MB-231 cells expressing sg723 or sgCtrl	This paper	N/A
Human: MYC-delta8 D11 clonal cell lines (clones 1 and 2)	This paper	N/A

(*Continued on next page*)

Please cite this article in press as: Shi et al., CRISPR mutagenesis of the *MYC* locus reveals a druggable ultraconserved RNA element, Cell (2027), https://doi.org/10.1016/j.cell.2026.10.002

Continued

REAGENT or RESOURCE	SOURCE	IDENTIFIER
Oligonucleotides		
MYC locus CRISPR tiling-mutagenesis sgRNA library (22,623 sgRNAs)	Twist Bioscience	See Table S1
Individual sgRNAs and cloning, genotyping, and amplicon-sequencing primers	Integrated DNA Technologies	See Table S2
sg723	Integrated DNA Technologies	See Table S2
Non-targeting control sgRNA (sgCtrl)	Integrated DNA Technologies	See Table S2
Fully 2′-MOE-modified steric-blocking MYC ASOs (ASO-1 to ASO-4)	Integrated DNA Technologies	See Table S5
Control ASOs (ASO-ctrl-1 to ASO-ctrl-3)	Integrated DNA Technologies	See Table S5
ON-TARGETplus Non-targeting Control siRNA Pool	Horizon Discovery	Cat#D-001810-10-05
ON-TARGETplus SMARTpool Human MYC siRNA	Horizon Discovery	Cat#L-003282-02-0005
ON-TARGETplus SMARTpool Human HNRNPL siRNA	Horizon Discovery	Cat#L-011293-01-0005
RNAscope human *MYC* probe	ACD Bio	Cat#311761-C3
RT-qPCR primers	Integrated DNA Technologies	See Table S2
Recombinant DNA		
LentiV_Cas9_puro	Tarumoto et al.[120]	Addgene plasmid #108100
pCMV-SpRY-HF1-ABE8e	Huang et al.[121]	Addgene plasmid #185670
LentiV-HF1-SpRY-ABE8e_puro	This paper	N/A
LentiV-HF1-SpRY-Cas9 WT	This paper	N/A
lentiU6-sgRNA/EF1a-mCherry	Savell et al.[122]	Addgene plasmid #114199
pCMV-GFP	Matsuda and Cepko[123]	Addgene plasmid #11153
pCMV-dR8.91	Jonathan Weissman laboratory	N/A
pMD2.G	Jonathan Weissman laboratory	N/A
pCMV-MYC	This paper	N/A
pCMV-MYC-2A-d2GFP	This paper	N/A
pCMV-MYC-2A-d2GFP-delta8	This paper	N/A
pCMV-MYC-2A-d2GFP-delta2	This paper	N/A
pCMV-MYC-2A-d2GFP-deltaAlu	This paper	N/A
pCMV-MYC-deltaAlu	This paper	N/A
2×HA-tagged pCMV-MYC-WT, pCMV-MYC-delta8, and pCMV-MYC-delta2	This paper	N/A
pcDNA3.1(+)-2×NLS-HA	This paper	N/A
pcDNA3.1(+)-2×NLS-HA-MYC	This paper	N/A
Software and algorithms		
MAGeCK	Li et al.[47]	https://github.com/liulab-dfci/MAGeCK
Variant Effect Predictor	McLaren et al.[124]	
bowtie	Langmead et al.[125]	https://bowtie-bio.sourceforge.net/index.shtm
CRISPROn	Anthon et al.[52]	https://rth.dk/resources/crispr/crispron/
DeepSpCas9	Kim et al.[51]	https://deepcrispr.info/workflows/DeepSpCas9
CRISPick	Doench et al.[50]	https://portals.broadinstitute.org/gppx/crispick/public
Cas-OFFinder	Bae et al.[68]	http://www.rgenome.net/cas-offinder/
fastp	Chen et al.[126]	https://github.com/OpenGene/fastp
STAR	Dobin et al.[127]	https://github.com/alexdobin/STAR

(*Continued on next page*)

Please cite this article in press as: Shi et al., CRISPR mutagenesis of the *MYC* locus reveals a druggable ultraconserved RNA element, Cell (2027), https://doi.org/10.1016/j.cell.2026.10.002

Continued

REAGENT or RESOURCE	SOURCE	IDENTIFIER
featureCounts	Liao et al.[128]	https://subread.sourceforge.net/featureCounts.html
deepTools	Ramírez et al.[129]	https://github.com/deeptools/deeptools
DESeq2	Love et al.[72]	http://www.bioconductor.org/packages/release/bioc/html/DESeq2.html
clusterProfiler	Yu et al.[130]	http://bioconductor.org/packages/release/bioc/html/clusterProfiler.html
BWA	Li[131]	https://bio-bwa.sourceforge.net/
MACS3	Doherty et al.[132]	https://github.com/macs3-project/MACS
csaw	Lun and Smyth[74]	https://bioconductor.org/packages//release/bioc/html/csaw.html
edgeR	Robinson et al.[133]	https://bioconductor.org/packages//release/bioc/html/edgeR.html
CRISPResso2	Clement et al.[134]	https://crispresso2.pinellolab.org/submission
FCS Express (Version 7.18.0015)	De Novo Software	https://denovosoftware.com
ImageJ	National Institutes of Health (NIH)	https://imagej.net/ij/
Prism (Version 10.4)	GraphPad Software	https://www.graphpad.com
Other		
QuantStudio 7 Flex Real-Time PCR System	Applied Biosystems	N/A
AVITI Sequencing System	Element Biosciences	N/A
Sony MA900 Cell Sorter	Sony Biotechnology	N/A
HybEZ II Hybridization System	ACD Bio	Cat#240200ACD
NanoDrop spectrophotometer	Thermo Scientific	Cat#ND-ONE-W
Qubit fluorometer	Thermo Scientific	Model: Qubit 4
Agilent TapeStation	Agilent Technologies	N/A
Stratalinker 2400 UV crosslinker	Stratagene	N/A
Full-length plasmid and amplicon sequencing services	Plasmidsaurus	https://app.plasmidsaurus.com

EXPERIMENTAL MODEL AND STUDY PARTICIPANT DETAILS

Cell culture

HEK293T (female), JJN-3 (female), D11 (female), MDA-MB-231 (female), U87MG (male), NCI-H2171 (male) and U2OS (female) cell lines were used in this research. HEK293T (ATCC, CRL-3216), MDA-MB-231 (ATCC, HTB-26), NCI-H2171 (ATCC, CRL-5929) and U2OS (ATCC, HTB-96) cells were purchased from ATCC. JJN-3 and D11 cells were gifts from Jerry Pelletier. U87MG cell line was a gift from Peter A. Sims. HEK293T, MDA-MB-231, U87MG and U2OS cells were cultured in DMEM with 4.5 g/L D-glucose (Gibco, 11995073) supplemented with 10% heat inactivated fetal bovine serum (FBS, Gibco, 10438026); no antibiotics were added. JJN-3, D11, and NCI-H2171 cells were cultured in RPMI 1640 Medium (Gibco, 11875119) supplemented with 10% heat inactivated FBS; no antibiotic was added. Low passage cells were used and passaged upon reaching 80-90% confluency. Cells were maintained at 5% CO2 and 37°C. All cells used in this study were confirmed to be negative for mycoplasma contamination and routinely tested using the MycoAlert Mycoplasma Detection Kit (Lonza, LT07-418).

Patient-derived organoids

Head and neck cancer patient-derived organoids (HSC10) and the esophageal adenocarcinoma (EAC) patient-derived organoids (EACorg000) were provided by the Columbia University Digestive & Liver Disease Research Core.

HSC10 was cultured in Matrigel using human organoid medium containing 50 ng/mL EGF (HOME50). HOME50 consisted of Advanced DMEM/F12 supplemented with 1 mM N-acetyl-L-cysteine, 2% R-spondin/Noggin-conditioned medium (provided by the Digestive & Liver Disease Research Core, Columbia University), 1× N2 supplement, 1× B27 supplement, 10 mM HEPES, 1× GlutaMAX, 1× antibiotic-antimycotic, 50 ng/mL recombinant human EGF, and 5 μM A83-01. EGF and A83-01 were freshly added to the culture medium immediately before use. Y-27632 was added at a final concentration of 10 μM on the day of plating only.

EACorg000 was maintained as previously described.[93,135] Briefly, organoids and L-WRN cell conditioned medium were provided by the Digestive & Liver Disease Research Core (Columbia University). Organoids were cultured in a 1:1 mixture of L-WRN cell

conditioned medium and basal medium consisting of Advanced DMEM/F12 supplemented with 1× GlutaMAX, 1% penicillin-streptomycin and 10 mM HEPES. The medium was further supplemented with 1× N-2, 1× B-27, 1 mM N-acetylcysteine, 0.5 μM CHIR99021, 250 ng/mL recombinant human EGF, 0.5 μM A83-01, 1 μM SB202190, 0.1 μM gastrin, 4 mM nicotinamide, 10 μM Y-27632, 5 μg/mL gentamicin and 1% antibiotic-antimycotic. Organoids were embedded in Matrigel and maintained with medium changes every 3 days.

Ethics statement

The research conforms to the ethical principles of the Declaration of Helsinki and the NIH Guidelines for Human Stem Cell Research. Human tissue specimens used in this study were collected with written informed consent from all participants, under protocols approved by the Institutional Review Boards of the University of Pennsylvania (protocol 813841) and Columbia University (protocols AAAS7031, AAAL5871). All procedures involving human subjects and biospecimens were performed in accordance with approved institutional guidelines and regulations.

METHOD DETAILS

Plasmid construction

The LentiV-HF1-SpRY-Cas9 WT plasmid was generated through a multi-step cloning strategy. First, the LentiV-HF1-SpRY-ABE8e_-puro plasmid was constructed by assembling fragments derived from LentiV_Cas9_puro[120] (Addgene, 108100) and pCMV-SpRY-HF1-ABE8e[121] (Addgene, 185670) using the Gibson Assembly® Master Mix (NEB, E2611S) according to the manufacturer's instructions. The resulting construct contained the HF1-SpRY-ABE8e cassette under the lentiviral backbone control. To generate the LentiV-HF1-SpRY-Cas9 WT plasmid, site-directed mutagenesis was performed to remove the ABE8e domain and revert the D10A nickase mutation in Cas9 to the wild-type catalytic residue. Mutagenic primers were designed using NEBaseChanger (New England Biolabs), and PCR amplification was initially carried out using the Phusion® High-Fidelity DNA Polymerase Kit (NEB, E0553). The resulting amplicons were then processed using the Q5® Site-Directed Mutagenesis Kit (NEB, E0554S) according to the manufacturer's instructions to introduce the desired mutations and generate the final construct. For sgRNA cloning, the lentiU6-sgRNA/EF1a-mCherry[122] (Addgene, 114199), which contains BbsI sites for spacer insertion, was used. For each target, two complementary oligonucleotides were synthesized: a forward oligo (5′-CACC-GN_{20}-3′) matching the sgRNA spacer sequence and a reverse oligo (5′-AAAC-reverse complement of N_{20}C-3′). The vector was digested with BbsI-HF (NEB, R3539S) and the correct band was purified using the Macherey-Nagel™ Gel and PCR Clean-up Kit (Macherey-Nagel, 740609). Oligo pairs were annealed (95°C for 5 min, ramped to 25°C at 5°C/min), and ligated into the digested backbone using T4 DNA ligase (NEB, M0202T). For plasmid transformation, all plasmids were transformed into NEB Stable Competent *E. coli* (C3040H) cells via heat shock at 42°C for 30 seconds. Cells were recovered in NEB Outgrowth Medium for 1 h at 30°C with shaking (250 rpm) and plated onto selective LB-agar plates containing the appropriate antibiotic. Plates were incubated at 30°C overnight to minimize potential recombination events in lentiviral backbones. Individual colonies were picked and cultured in 5 mL of LB broth containing the corresponding antibiotic at 30°C for 24 h with shaking. Plasmid DNA was purified using the Macherey-Nagel™ Nucleospin™ Plasmid Transfection-grade Kit (Macherey-Nagel, 740490) according to the manufacturer's protocol. Final construct verification was conducted through full-length plasmid sequencing performed by Plasmidsaurus to confirm each plasmid sequence.

Cloning the *MYC* locus on plasmids

A full-length *MYC* expression construct was generated to include the endogenous 5′ untranslated region (5′ UTR), all introns and exons, with or without a 2A-GFP cassette, the complete 3′ UTR, and an additional 150 bp downstream of the 3′ UTR in a pCMV-based backbone. Plasmids were assembled using a seamless Gibson-style cloning strategy. The pCMV-GFP backbone[123] (Addgene, 11153) and the full-length *MYC* genomic fragment were amplified by PCR using Platinum™ SuperFi™ II DNA Polymerase (Invitrogen, 12361010). During vector amplification, the GFP sequence in the pCMV-GFP backbone was excluded. Primers were designed using the GeneArt Seamless Cloning and Assembly online design tool and are listed in Table S2. PCR reactions (50 μL total volume) contained 1× SuperFi™ II Buffer, 0.2 μM each primer, 200 μM each dNTP, Platinum™ SuperFi™ II DNA Polymerase, template DNA, and nuclease-free water to volume. Templates included 20 ng pCMV-GFP plasmid DNA for vector amplification and 200 ng D11 genomic DNA for *MYC* amplification. PCR was performed for 30 cycles with extension times of 4 min for the vector backbone and 9 min for the full-length *MYC* insert. PCR products were resolved by agarose gel electrophoresis, and bands of the expected size were excised and purified using the Macherey-Nagel™ Gel and PCR Clean-up Kit (Macherey-Nagel, 740609) according to the manufacturer's instructions. Purified PCR products were assembled using the GeneArt® Seamless Cloning and Assembly Enzyme Mix (Invitrogen, A14606). Assembly reactions were set up at a molar ratio of *MYC* insert to vector of 2:1. Insert DNA and linearized vector were combined with nuclease-free water to a final volume of 5 μL, followed by the addition of 5 μL GeneArt 2× Enzyme Mix. Reactions were mixed gently, briefly centrifuged, and incubated at room temperature for 15-30 min. Following incubation, the same methods for bacterial transformation, plasmid purification, and full-length plasmid sequencing as described above were used.

For generation of the pCMV-MYC-2A-d2GFP-Δ8 and pCMV-MYC-2A-d2GFP-Δ2 plasmids, pCMV-MYC-2A-d2GFP was used as the parental backbone. Gibson-style seamless cloning was performed following the same procedures described above, using primers listed in Table S2.

For generation of the pCMV-MYC-2A-d2GFP-ΔAlu and pCMV-MYC-ΔAlu plasmids, pCMV-MYC-2A-d2GFP and pCMV-MYC were used as the parental backbone. PCR primers were designed using NEBaseChanger (New England Biolabs), and all primer sequences are listed in Table S2. Site-directed mutagenesis was performed by PCR using Platinum™ SuperFi™ II DNA Polymerase (Invitrogen, 12361010) with 10 ng of the corresponding parental plasmid as template in a 50 μL reaction containing 1× SuperFi™ II Buffer, 200 μM each dNTP, and 0.2 μM of each primer. PCR was performed for 30 cycles with a 12 min extension step. Following amplification, PCR products were subjected to kinase-ligase-DpnI (KLD) treatment using the Q5® Site-Directed Mutagenesis Kit (New England Biolabs, E0554S) by combining 1 μL PCR product with 5 μL 2× KLD Reaction Buffer, 1 μL 10× KLD Enzyme Mix, and 3 μL nuclease-free water, followed by incubation at room temperature for 5 min. Following incubation, the same methods for bacterial transformation, plasmid purification, and full-length plasmid sequencing as described above were used.

All oligonucleotides were synthesized by Integrated DNA Technologies (IDT).

sgRNA library design

The 10,055-bp genomic locus (chr8:127,734,053-127,744,107, hg38) containing the *MYC* gene was used for tiling mutagenesis. This region covers all annotated *MYC* transcript isoforms (GENCODE v49) and over 1-kb intergenic DNA on each end containing evolutionary conserved sequences across 100 vertebrate genomes (Figure 1A). All possible 20-nt sequences on both the plus and minus strands in this region were used as sgRNA spacers. In addition, genomic DNA amplicon sequencing identified three SNPs in the D11 cells used. All 20-nt sequences overlapping with these SNPs on either strand were also added to the library. In the D11 cell line, one of the *MYC* alleles contains P2A-GFP at the C-terminal end. All 20-nt sequences overlapping with this insert (both plus and minus strands) were also included in the library. A total of 565 negative control sgRNAs were included, comprising 404 targeting a 221-nt random sequence, 111 targeting the non-essential AAVS1 locus, and 50 non-targeting sgRNAs. In total, the library contained 22,623 sgRNAs.

sgRNA library cloning

A DNA oligo pool containing all 20-nt sgRNA spacer sequences and constant flanking sequences (5′-TAACTTGCTATTTCTAGCTCTAAAAC and CGGTGTTTCGTCCTTTCCACAAGATATATAAAGCCA-3′) was synthesized by Twist Bioscience. The oligo pool was resuspended in TE buffer (10 mM Tris-Cl pH 8.0, 1 mM EDTA) to 10 ng/μL and PCR-amplified (10 ng template, 10 cycles) using the KAPA HiFi HotStart PCR Kit (Kapa Biosystems, KK2502) and primers listed in Table S2. The PCR product was cleaned up using the Macherey-Nagel™ Gel and PCR Clean-up Kit (Macherey-Nagel, 740609). NEBuilder® HiFi DNA Assembly Master Mix (NEB, E2621S) was used to insert the sgRNA library into the sgRNA vector lentiU6-sgRNA/EF1a-mCherry via Gibson assembly. The product was cleaned up using isopropanol precipitation. 550 ng DNA was used in electroporation in Endura competent cells (Endura, 60242-1). Bacteria were plated in six 245 mm square dishes and cultured for 18 h. Bacterial colonies were scraped off in liquid LB, followed by maxiprep with MACHEREY-NAGEL kit (Macherey-Nagel, 740414.50).

CRISPR tiling mutagenesis screening

HF1-SpRY-Cas9 stable cell line generation

The HF1-SpRY-Cas9 lentivirus was generated using the packaging system consisting of pCMV-dR8.91 and pMD2.G (gifts from Jonathan Weissman). Plasmids were co-transfected into HEK293T cells in 10 cm dish using Lipofectamine 3000 (Thermo Fisher Scientific, L3000015) according to the manufacturer's instructions. The culture medium was replaced with fresh growth medium 6 h post-transfection. Viral supernatants were collected at 48 and 72 h post-transfection, followed by centrifugation at 800 × g for 5 min to remove cell debris. The clarified supernatant containing the lentivirus was filtered through a 0.45 μm PVDF membrane filter (Sigma, SLHV033RS), concentrated using Lenti-X™ Concentrator (Takara, 631231), resuspended in RPMI 1640 media, and used to infect 2.1×10^6 cells in the presence of polybrene (8 μg/mL). Media was changed 24 h after infection. At 3 days post-infection, cells were selected with puromycin (0.5 μg/mL) for 4 days. The expression of HF1-SpRY-Cas9 was confirmed by RT-qPCR at the end of the selection.

Lentivirus for sgRNA

sgRNA library lentivirus was prepared using the same method for the HF1-SpRY-Cas9 stable cells generation. 30.1 μg of plasmids was used.

Infection and screening

For functional interrogation, 5×10^6 cells were seeded per T75 flask, for a total of 2.5×10^8 cells for infection. Cells were transduced at a low multiplicity of infection (MOI < 0.3) to ensure that the majority of cells received only a single gRNA cassette. Lentivirus was added at 0.2 mL per 5×10^6 cells in 20 mL total culture media, supplemented with 16 μL polybrene (8 μg/mL). After 24 h, cells were washed three times with fresh growth media. At least 2.5×10^8 cells were maintained continuously for culture. After 48 h, the sgRNA positive ratio was tested by flow cytometry testing the mCherry. The time point 48 h post-infection was designated as Day 0. On Day 6, mCherry-positive cells were sorted and maintained at ~1,000× library coverage. Cells were collected every other day until Day 20.

Please cite this article in press as: Shi et al., CRISPR mutagenesis of the *MYC* locus reveals a druggable ultraconserved RNA element, Cell (2027), https://doi.org/10.1016/j.cell.2026.10.002

For high-MOI infection, 5×10^6 cells were seeded per T75 flask in 6 flasks (3×10^7 cells total) and infected at an MOI of 8.7 in the presence of polybrene (8 μg/mL). After 24 h, cells were washed three times with fresh growth media. After 48 h, the sgRNA positive ratio was measured by flow cytometry using mCherry as a marker. The time point 48 h post-infection was designated as Day 0. All cells were collected for DNA extraction.

Genomic DNA extraction

Samples were collected at day 0, day 8, and day 20, and genomic DNA was isolated using the Macherey-Nagel NucleoSpin Tissue kit (Macherey-Nagel, 740952.50) according to the manufacturer's protocol with modifications. Samples were treated with RNase A to eliminate RNA contamination. DNA was eluted using 50 μL elution buffer (EB) per column with a 3 min incubation at room temperature, followed by centrifugation for 1 min. To maximize DNA recovery, each column was eluted three times, and eluates were pooled. DNA concentration and purity were determined using a NanoDrop spectrophotometer (Thermo Scientific). Sample quality was assessed by spectrophotometric measurement of A260/A280 and A260/A230 ratios, which ranged from 1.86–1.90 and 2.41–2.43, respectively. DNA concentrations were verified using a Qubit fluorometer (Thermo Scientific) for accurate quantification.

PCR amplification and purification

Targeted genomic regions were amplified by PCR using extracted genomic DNA as template. PCR reactions were optimized for each sample type with template amounts of 4 μg per 100 μL reaction. Forward primer pools were prepared by combining equal volumes of individual forward primers (100 μM stock concentrations) and diluting the mixture to a final concentration of 10 μM for PCR use. PCR cycling conditions were optimized through preliminary experiments, and the number of amplification cycles was limited to a maximum of 19. Multiple parallel PCR reactions were performed to generate sufficient amplicon for high-throughput sequencing. PCR products from all parallel reactions were pooled and thoroughly mixed. Initial purification was performed using the MN NucleoSpin PCR Clean-up kit (Macherey-Nagel, 740609). Each column was eluted three times with nuclease-free water to maximize product recovery. Purified PCR products underwent gel purification using 1.5% agarose gel electrophoresis in 1× TAE buffer. Target bands were excised and purified using the MN NucleoSpin Gel and PCR Clean-up kit (Macherey-Nagel, 740609). Final purified products were eluted three times per column. Sample quality was assessed by NanoDrop spectrophotometry.

Library sequencing

Sequencing libraries were quantified using the KAPA Library Quantification Kit (Roche, 07960336001) according to the manufacturer's instructions. Libraries were sequenced on the AVITI sequencing platform (Element Biosciences). Library normalization and denaturation were performed using IDTE buffer (pH 8.0, Integrated DNA Technologies) as the low TE buffer. Sequencing was performed according to the AVITI System User Guide with paired-end 75 bp reads.

Competitive assay

To validate the growth-inhibitory effect of individual sgRNAs, a competitive growth assay was performed. Stable cell lines expressing HF1-SpRY-Cas9 or HF1-SpRY-ABE8e were first generated. The HF1-SpRY-ABE8e cell line was established using the procedure described above for HF1-SpRY-Cas9. These cell lines were then transduced with either a non-targeting control sgRNA (sgCtrl) or individual targeting sgRNAs to establish stable cell populations. The sgCtrl and individual targeting sgRNAs cells (1×10^6 each) were mixed, and 2×10^5 cells were collected on the same day as the initial time point (Day 0). The remaining mixed cells were cultured, and 1×10^6 cells were collected every other day for analysis. Genomic DNA was extracted from each sample, followed by PCR amplification of the sgRNA region and amplicon sequencing (Plasmidsaurus) to quantify the abundance of each sgRNA over time.

Cell proliferation assays

Cells were incubated with the 10% (v/v) WST-1 reagent (Sigma, 11644807001) for 2 h. The absorbance of the samples was measured using a microplate reader at 440 nm.

Amplicon sequencing for on-target and off-target mutation analysis

Following Cas9-sgRNA-mediated mutagenesis, genomic DNA was extracted and the target loci were amplified by PCR using Q5 High-Fidelity 2× Master Mix (New England Biolabs, M0492S) with primers listed in Table S2. PCR products were resolved by agarose gel electrophoresis and purified prior to sequencing using Plasmidsaurus amplicon sequencing service. Resulting FASTQ files were retrieved and analyzed using CRISPResso2 to quantify insertion-deletion (indel) frequencies and editing outcomes.[134,136] For sg723 off-target analysis, all top 15 predicted off-target sites with less than 3 mismatches were tested except three intergenic sites with two mismatches. These three sites share the same targeting sequence as another site we tested (LINC01145), which showed no mutations.

ASO transfection

Lyophilized ASOs were centrifuged briefly upon receipt and stored dry at −20°C until use. ASOs were resuspended in nuclease-free water to generate concentrated stock solutions (typically 100-200 μM), calculated based on the manufacturer-provided oligonucleotide amount. Resuspension was performed by gentle pipetting without vortexing, followed by 10 min incubation at room temperature to ensure complete dissolution. Resuspended ASOs were aliquoted into single-use volumes and stored at −80°C. For experimental use, aliquots were thawed on ice, mixed gently, and diluted to working concentrations. ASOs were transfected at a final concentration of 100 nM. Opti-MEM I Reduced-Serum Medium (Gibco, 31985062) was pre-warmed at 37 °C for 30 min before

use. Nuclease-free tubes were used for transfection. After incubation for 5 min at room temperature, the ASO-lipid complex was added to the cells. The culture medium was not changed post-transfection. Cells were harvested at indicated time for experiments. The ASO sequences are listed in Table S5.

siRNA transfection

Cells were transfected with a non-targeting control siRNA pool (Horizon Discovery, D-001810-10-05), siRNA pools targeting human *MYC* (Horizon Discovery, L-003282-02-0005), or siRNA pools targeting human *HNRNPL* (Horizon Discovery, L-011293-01-0005) using Lipofectamine™ RNAiMAX Transfection Reagent (Invitrogen, 13778) according to the manufacturer's instructions. siRNAs were transfected at a final concentration of 20 nM. Nuclease-free tubes were used for transfection. Opti-MEM I Reduced-Serum Medium (Gibco, 31985062) was pre-warmed at 37 °C for 30 min before use. After incubation for 5 min at room temperature, the siRNA-lipid complexes were added dropwise to the cells. The culture medium was not changed post-transfection. Cells were harvested at indicated time for RNA extraction and RT-qPCR analysis. For cell viability assays (WST-1), cells were transfected in 48-well plates using the same procedure and a final siRNA concentration of 20 nM. For Immunofluorescence and RNAscope assays, cells were transfected in 8-well Lab-Tek II CC2 chamber slides using the same procedure and a final siRNA concentration of 20 nM. For *MYC* mRNA RNAscope assay and MYC protein immunofluorescence assay following siHNRNPL treatment, cells were transfected with 20 nM siRNA for 5 days, with medium replacement and repeat siRNA transfection every 48 h to account for the prolonged half-life of hnRNP L protein (~138 h).[137]

Quantitative reverse transcription PCR

Total RNA was extracted using the MACHEREY-NAGEL NucleoSpin RNA Plus kit (Macherey-Nagel, 740984.250), and cDNA was synthesized using SuperScript™ IV Reverse Transcriptase (Invitrogen, 18090050). Quantitative RT-PCR was performed using SYBR Green Master Mix (Applied Biosystems, A25741) on a QuantStudio 7 Flex Real-Time PCR System (Applied Biosystems). Gene expression levels were normalized to samples transfected with control siRNA or control ASO. *ACTB* was used as internal control.

Western blot

Cells were lysed in ice-cold RIPA buffer (Sigma-Aldrich, R0278) supplemented with protease inhibitor cocktail (Roche, 4693132001). Briefly, culture dishes were placed on ice, cells were harvested and pelleted by centrifugation at 300 × g for 5 min at 4°C, washed twice with ice-cold PBS, and lysed in RIPA buffer for 30 min on ice with intermittent vortexing. Lysates were clarified by centrifugation at 15,000 × g for 15 min at 4°C, and supernatants were collected for downstream analysis. Protein concentrations were determined using the BCA Protein Assay Kit (Thermo Fisher Scientific, 23225) according to the manufacturer's instructions. Equal amounts of total protein were adjusted to the same final volume with lysis buffer, mixed with NuPAGE LDS Sample Buffer (4×; Invitrogen, NP0007) and NuPAGE Reducing Agent (10×; Invitrogen, NP0004), and heated at 70°C for 10 min prior to electrophoresis. Proteins were separated by SDS-PAGE using NuPAGE Bis-Tris gels with MOPS SDS Running Buffer (1×; Invitrogen, NP0001) at 100 - 200 V until the dye front reached the bottom of the gel. Pre-stained protein standards (Invitrogen, LC5800) were included for molecular weight estimation. Following electrophoresis, proteins were transferred onto PVDF membranes using Tris-glycine transfer buffer (1×; Invitrogen, LC3675) containing 20% methanol at 20 V for 2 h. Membranes were briefly washed with deionized water and stained with Ponceau S solution (Cell Signaling Technology, 59803S) to assess protein transfer and loading. After documentation, membranes were destained with TBST and blocked in 5% non-fat dry milk prepared in TBST for 1 h at room temperature with gentle agitation. Blocked membranes were incubated with primary antibodies diluted in blocking buffer for overnight at 4°C, including MYC (Santa Cruz Biotechnology, sc-40, 1:500; Cell Signaling Technology, 5605T, 1:1,000; Invitrogen, MA5-42675, 1:500; Invitrogen, MA1-980-HRP, 1:500; or Abcam, ab32072, 1:1,000), Vinculin (CST, 13901, 1:2,000), LC3 (Proteintech, 14600-1-AP, 1:2,000), STING (CST, 50494, 1:2,000), Phospho-STING (Ser366) (CST, 19781T, 1:2,000), TBK1 (CST, 3504T, 1:2,000), Phospho-TBK1 (Ser172) (CST, 5483T, 1:2,000), GAPDH (CST, 97166, 1:2,000), Vimentin (Abcam, ab92547, 1:2,000), U1 snRNP 70 (Santa Cruz Biotechnology, sc-390899, 1:1,000). Membranes were then washed three times with TBST and incubated with appropriate HRP-conjugated secondary antibodies diluted 1:10,000 - 1:20,000 in blocking buffer for 1 h at room temperature. After three additional washes, protein signals were detected using SuperSignal West Pico PLUS chemiluminescent substrate (Thermo Fisher Scientific, 34580) and visualized by chemiluminescence imaging. Band intensities were quantified using ImageJ (NIH). Ponceau S staining or housekeeping proteins were used as loading controls, as indicated.

Subcellular fractionation

Cells were treated with ASOs for 72 h and harvested with trypsin-EDTA. After neutralization with complete medium, cells were collected by centrifugation at 500 × g for 5 min at 4°C, washed with ice-cold PBS, and counted. Equal numbers of cells from each treatment condition were then pelleted and processed for subcellular protein fractionation using the Subcellular Protein Fractionation Kit for Cultured Cells (Thermo Fisher Scientific, 78840) according to the manufacturer's instructions. Briefly, cell pellets were sequentially extracted with cytoplasmic extraction buffer, membrane extraction buffer, nuclear extraction buffer, micrococcal

Please cite this article in press as: Shi et al., CRISPR mutagenesis of the *MYC* locus reveals a druggable ultraconserved RNA element, Cell (2027), https://doi.org/10.1016/j.cell.2026.10.002

nuclease-containing nuclear extraction buffer, and pellet extraction buffer to obtain cytoplasmic, membrane, soluble nuclear, chromatin-bound nuclear, and cytoskeletal fractions, respectively. Protease inhibitors were added freshly to all extraction buffers immediately before use.

For immunoblotting, protein fractions were mixed with reducing SDS sample buffer and heated before SDS-PAGE. To avoid saturation of the nuclear MYC signal and improve detection of low-abundance MYC in non-nuclear fractions, the soluble nuclear fraction was loaded at one-fifth of the cytoplasmic and cytoskeletal fractions.

Immunofluorescence

Cells were seeded in 8-well Lab-Tek II CC2 chamber slides (Thermo Scientific) in 250 μL of complete growth medium and allowed to adhere overnight. Cells were transiently transfected as indicated, and immunofluorescence staining was performed 48 h post-transfection. For MYC protein staining following siHNRNPL treatment, cells were transfected with 20 nM siRNA for 5 days, with medium replacement and repeat siRNA transfection every 48 h.

Cells were washed once with PBS and fixed with 4% paraformaldehyde in PBS for 15 min at room temperature. Following fixation, cells were washed three times with PBS and permeabilized using the permeabilization solution in the Image-iT Fixation/Permeabilization Kit (Thermo Fisher Scientific, A5818101) for 15 min at room temperature. Cells were then washed three times with PBS and blocked with the kit-provided blocking solution for 1 h at room temperature. Primary antibody incubation was performed using anti-MYC (Abcam, ab32072), anti-HA antibody (Thermo Fisher Scientific, 26183), or anti-hnRNP L (Santa Cruz Biotechnology, sc-32317) diluted 1:500 in blocking solution, followed by overnight incubation at 4°C. Cells were washed three times with PBS and incubated with Cy3-conjugated goat anti-rabbit IgG (H+L) secondary antibody (Thermo Fisher Scientific, A10520), Cy3-conjugated goat anti-mouse IgG (H+L) secondary antibody (Thermo Fisher Scientific, M30010), or Alexa Fluor 488-conjugated goat anti-mouse IgG (H+L) secondary antibody (Thermo Fisher Scientific, A28175) diluted 1:500 in PBS, for 1 h at room temperature in the dark. After five additional washes with PBS, nuclei were counterstained with DAPI (1 μg/mL in PBS) for 5 min at room temperature in the dark. Following final washes, chambers were mounted with coverslips prior to imaging. Images were acquired at randomly selected fields of view using confocal fluorescence microscope under identical acquisition settings for all conditions.

Immunofluorescence signals were quantified using ImageJ (NIH). For each cell, nuclear regions of interest (ROIs) were manually delineated based on DAPI staining, while cytoplasmic ROIs were defined as the total cell area minus the nuclear region. Integrated fluorescence intensity and area were measured for each ROI. Background fluorescence was determined from an adjacent cell-free region and subtracted using the corrected total cell fluorescence (CTCF) formula: CTCF = Integrated Density − (Area × Mean Background Fluorescence).

2×NLS-MYC rescue assay

U87MG cells were seeded at 7.0×10^4 cells per well in 48-well plates and transfected with empty vector, 2×NLS-HA, or 2×NLS-HA-MYC expression plasmids using Lipofectamine 3000. The 2×NLS-HA-MYC construct contained the MYC coding sequence (CDS) with a 2×NLS-HA tag added to the N terminus of MYC and lacked the endogenous MYC 3′ UTR, rendering it resistant to ASO-1 and ASO-2. At 24 h after plasmid transfection, cells were transfected with control ASO (ASO-ctrl), ASO-1, or ASO-2 at a final concentration of 100 nM using Lipofectamine RNAiMAX. Cell viability was measured 24 h after ASO transfection using the WST-1 assay as described above.

For subcellular localization analysis, cells were fixed 48 h after plasmid transfection and subjected to immunofluorescence staining with an anti-HA antibody and DAPI as described in the Immunofluorescence subsection.

RNAscope

Cells were seeded one day prior to transfection in 8-well Lab-Tek II CC2 chamber slides at a density sufficient to achieve 70-80% confluence at the time of fixation. Cells were transfected using the same procedure as described above and a final ASO concentration of 100 nM. For *MYC* mRNA staining following siHNRNPL treatment, cells were transfected with 20 nM siRNA for 5 days, with medium replacement and repeat siRNA transfection every 48 h.

After treatment, cells were washed twice with PBS and fixed with 10% neutral buffered formalin (Sigma-Aldrich, HT501128) for 30 min at room temperature. Following fixation, cells were rinsed three times with PBS and processed immediately for RNAscope analysis. RNAscope multiplex fluorescent in situ hybridization was performed using the RNAscope Multiplex Fluorescent Reagent Kit v2 (ACD Bio, 323110) according to the manufacturer's instructions with minor modifications. All hybridization steps were carried out using the HybEZ II Hybridization System at 40°C unless otherwise specified. Wash buffer was prepared by diluting the 10× RNAscope wash buffer to 1× with distilled water. Fixed cells were treated with RNAscope hydrogen peroxide for 10 min at room temperature to quench endogenous peroxidase activity, followed by two washes with distilled water. Cells were then permeabilized by incubation with diluted Protease III (1:15 in PBS) for 10 min at room temperature. Cells were washed three times with PBS prior to probe hybridization. Target probe hybridization was performed using the human *MYC* probe (ACD Bio, 311761-C3), diluted according to the manufacturer's recommendations, and incubated for 2 h at 40°C. Excess probe was removed, and cells were washed three times with 1× RNAscope wash buffer. Signal amplification was carried out sequentially using RNAscope Multiplex FL v2 Amp 1 and Amp 2 reagents for 30 min each, followed by Amp 3 for 15 min, with two washes in wash buffer between each amplification step. For signal detection, HRP-C3 was applied for 15 min at 40°C, followed by washing and development with Opal 690 fluorophore (Akoya

Please cite this article in press as: Shi et al., CRISPR mutagenesis of the *MYC* locus reveals a druggable ultraconserved RNA element, Cell (2027), https://doi.org/10.1016/j.cell.2026.10.002

Biosciences, FP1497001KT), which substitutes for TSA Plus Cyanine 5. Opal 690 was diluted 1:250 in RNAscope Multiplex TSA buffer and incubated for 30 min at 40°C. Following fluorophore development, HRP activity was quenched using the RNAscope HRP blocker for 15 min at 40°C, followed by washing. Nuclei were counterstained with DAPI for 30 s at room temperature. Cells were washed with PBS and chambers were mounted with coverslips prior to imaging. Fluorescence images were acquired at randomly selected fields of view using a confocal fluorescence microscope under identical acquisition settings across conditions.

RNAscope signals were quantified using ImageJ (NIH). For each field of view, individual RNA puncta located in the cytoplasm were identified, and nuclear boundaries were manually or semi-automatically delineated based on DAPI staining. Only RNA puncta outside the nuclear boundary were included for analysis. The distance from each cytoplasmic RNA punctum to the nearest nuclear boundary was measured using ImageJ measurement tools.

Super-resolution analysis of *MYC* mRNA and hnRNP L colocalization

For super-resolution colocalization experiments, cells were transfected with the indicated ASOs at a final concentration of 30 nM for 48 h. RNAscope was performed first following the standard protocol, with the exception that after hydrogen peroxide treatment, Protease III digestion was replaced with PretreatPro (ACD Bio, 323770). The assay was carried through the blocking step, omitting DAPI staining. For signal detection, HRP-C3 was applied for 15 min at 40°C, followed by washing and development with Opal 570 fluorophore (Akoya Biosciences, FP1488001KT). Opal 570 was diluted 1:250 in RNAscope Multiplex TSA buffer and incubated for 30 min at 40°C. Following fluorophore development, HRP activity was quenched using the RNAscope HRP blocker for 15 min at 40°C, followed by washing. Subsequently, immunofluorescence staining was performed starting from the blocking step. Cells were incubated with anti-hnRNP L (Santa Cruz Biotechnology, sc-32317) diluted overnight at 4°C, followed by incubation with Alexa Fluor 488-conjugated goat anti-mouse IgG (H+L) secondary antibody (Thermo Fisher Scientific, A28175). After secondary antibody incubation, cells were incubated with DAPI for 5 min at room temperature in the dark. Following final washes, chamber slides were mounted with coverslips prior to imaging.

Super-resolution images were acquired from randomly selected fields of view using a Zeiss LSM microscope equipped with Airyscan 2 and a Plan-Apochromat 63×/1.4 NA Oil DIC M27 objective. Images were collected in Airyscan SR mode using identical acquisition settings across all experimental conditions. Raw Airyscan data were automatically processed using ZEN Blue software with identical processing parameters applied to all images.

Apoptosis analysis by Annexin V/7-AAD staining

Cells were seeded in 6-well plates at a density of 1.0×10^5 cells per well and transiently transfected as indicated above. 72 h after transfection, cells were harvested for apoptosis analysis. Cells were washed twice with ice-cold Cell Staining Buffer (BioLegend, 420201) and resuspended in Annexin V Binding Buffer (BioLegend, 422201). A total of 100 μL of the cell suspension was transferred to 1.5 mL tubes for staining. APC-conjugated Annexin V (BioLegend, 640930), diluted 1:10 in Annexin V Binding Buffer, was added at 5 μL per sample, followed by the addition of 7-aminoactinomycin D (7-AAD) according to the manufacturer's instructions. Samples were gently mixed and incubated for 15 min at room temperature in the dark. Following incubation, 400 μL of Annexin V Binding Buffer was added to each sample, and cells were analyzed immediately by flow cytometry. Data were analyzed using standard flow cytometry analysis software (De Novo Software, FCS Express).

Single-cell cloning and genotyping

D11-SpRY-Cas9 cells were seeded at 2.0×10^6 cells per T25 non-tissue-culture-treated flask in 5 mL complete growth medium. Lentiviral particles encoding sg723 or sgCtrl, packaged as described above, were added directly to the cultures (20 μL virus per flask) together with polybrene (8 μg/mL). Culture medium was replaced 24 h post-infection. Cells were collected by centrifugation at 200 × g for 5 min, washed twice with fresh medium (200 × g for 5 min each wash), resuspended in complete medium, and subsequently expanded and passaged as needed. To assess infection efficiency and ensure appropriate conditions for single-cell cloning, the percentage of mCherry-positive (sgRNA-positive) cells was quantified by flow cytometry. mCherry-positive cells infected with sgCtrl were collected and expanded as polyclonal control populations. For clonal isolation, cells infected with sg723 were single-cell sorted into 96-well plates (one cell per well) using a Sony MA900 cell sorter and cultured under standard conditions. Individual clones were expanded, and genomic DNA was isolated using the Macherey-Nagel NucleoSpin Tissue kit (Macherey-Nagel, 740952.50) according to the manufacturer's instructions. The targeted genomic locus was amplified using Q5 High-Fidelity 2× Master Mix (New England Biolabs, M0492S) with primers listed in Table S2. PCR reactions (50 μL total volume) contained 25 μL Q5 High-Fidelity 2× Master Mix, 2.5 μL of each primer (final concentration 0.5 μM), template genomic DNA (< 1,000 ng), and nuclease-free water to volume. Thermocycling conditions were as follows: initial denaturation at 98°C for 30 s; 40 cycles of 98°C for 10 s, 68°C for 30 s, and 72°C for 90 s; followed by a final extension at 72°C for 2 min and a hold at 4-10°C. PCR products were resolved by agarose gel electrophoresis, purified, and subjected to amplicon sequencing using the Plasmidsaurus sequencing service. Sequencing data were analyzed as described above.

RNA-seq

For ASO related RNA-seq experiments, MDA-MB-231 cells were seeded in 6-well plates at 1.0×10^5 cells per well for the non-targeting negative control conditions (ASO-ctrl, ASO-ctrl-2, and ASO-ctrl-3) and at 3.0×10^5 cells per well for the ASO-treated conditions

Please cite this article in press as: Shi et al., CRISPR mutagenesis of the *MYC* locus reveals a druggable ultraconserved RNA element, Cell (2027), https://doi.org/10.1016/j.cell.2026.10.002

(ASO-1, ASO-2, and ASO-3). Cells were transfected with the indicated ASOs at a final concentration of 100 nM. Culture medium was refreshed 48 h post-transfection. Cells were collected at < 80% confluency. MDA-MB-231 treated cells were harvested at 48 h and 72 h post-transfection. At each time point, cells were lysed directly in 350 μL lysis buffer (LBP), and lysates were immediately stored at −80°C until RNA isolation.

MDA-MB-231 parental cells and D11-SpRY-Cas9 cells were collected without any treatment. Cells were lysed directly in 350 μL lysis buffer (LBP), and lysates were immediately stored at −80°C until RNA isolation.

For plasmids related RNA-seq experiments, HEK293T cells were seeded in 6-well plates at 1.0×10^5 cells per well. Cells were transfected with 2,500 ng of the indicated plasmid DNA. Culture medium was refreshed 48 h post-transfection. Cells were harvested at 72 h post-transfection. Cells were lysed directly in 350 μL lysis buffer (LBP), and lysates were immediately stored at −80°C until RNA isolation.

Total RNA was extracted using the MACHEREY-NAGEL NucleoSpin RNA Plus kit (Macherey-Nagel, 740984.250) according to the manufacturer's instructions. RNA purity was assessed by NanoDrop spectrophotometry, only samples with A_{260}/A_{280} ratios of approximately 2.0 and A_{260}/A_{230} ratios greater than 2.0 were used. RNA integrity was evaluated using the Agilent TapeStation, and only samples with RNA integrity number equivalent (RINe) value greater than 9.5 were used for RNA sequencing. RNA-sequencing libraries were prepared from quality-controlled total RNA using poly(A) selection to enrich for mRNA. Libraries were constructed following standard bulk RNA-sequencing protocols and sequenced on the AVITI sequencing platform to generate transcriptomic data.

For siRNA related RNA-seq experiments, MDA-MB-231 cells were transfected with a non-targeting control siRNA pool (Horizon Discovery, D-001810-10-05), siRNA pools targeting human *MYC* (Horizon Discovery, L-003282-02-0005), or siRNA pools targeting human *HNRNPL* (Horizon Discovery, L-011293-01-0005) using Lipofectamine™ RNAiMAX Transfection Reagent (Invitrogen, 13778) according to the manufacturer's instructions. siRNAs were transfected at a final concentration of 20 nM. *MYC* siRNA treated cells were collected at 48 or 72 h after transfection. HNRNPL siRNA treated cells were cultured for 6 days, with medium replacement and repeat siRNA transfection every 48 h.

Total RNA was extracted using the MACHEREY-NAGEL NucleoSpin RNA Plus kit (Macherey-Nagel, 740984.250) according to the manufacturer's instructions. RNA-seq libraries were prepared by Plasmidsaurus using a poly(A)-selected, 3′-end counting workflow. Polyadenylated mRNA was captured and reverse-transcribed using a poly(dT) primer containing a sample-specific barcode, a unique molecular identifier (UMI), and the Read 1 sequence. Following second-strand synthesis, the resulting double-stranded cDNA was fragmented by tagmentation, which simultaneously incorporated the Read 2 sequence. Libraries were subsequently amplified by PCR to introduce unique dual indices (i5 and i7) and the P5 and P7 Illumina flow-cell adapter sequences.

ChIP-seq

MDA-MB-231 cells were transfected with the indicated ASOs at a final concentration of 100 nM using Lipofectamine RNAiMAX. The culture medium was replaced 24 h after transfection, and cells were collected at 48 h. D11 suspension cells were collected without ASO treatment.

Cells were crosslinked directly in culture medium with 1% methanol-free formaldehyde for 10 min at room temperature with continuous gentle agitation. Crosslinking was quenched with glycine for 5 min at room temperature. Adherent MDA-MB-231 cells were washed with ice-cold PBS supplemented with cOmplete Protease Inhibitor Cocktail, scraped from the dishes, and collected by centrifugation at 500 × g for 5 min at 4°C. D11 cells were collected by centrifugation under the same conditions immediately after quenching. Cell pellets were washed twice with ice-cold PBS containing protease inhibitors. Residual PBS was removed by an additional brief centrifugation, and the resulting pellets were snap-frozen in liquid nitrogen and stored at −80°C.

Frozen cell pellets were shipped on dry ice to Epigenome Technologies for ChIP-seq. Chromatin was prepared using the SimpleChIP Enzymatic Chromatin IP Kit (Cell Signaling Technology, 9003), with minor modification. Briefly, cells were lysed with Buffer A for 10 min, washed once with Buffer B, and quantified. MNase digestion was performed with reactions scaled to the nuclei number (1.5×10^6 nuclei and 2 μL of 10-fold-diluted MNase per 100 μL). After digestion at 37°C for 20 min, the reaction was terminated by the addition of EDTA. 10× ChIP Buffer and water were used to bring each sample to 500 μL in 1× ChIP Buffer, samples were then incubated for 10 min at room temperature to allow digested chromatin to diffuse into the supernatant. Solutions were clarified by centrifugation at 18,000 × g for 10 min, and the supernatant containing digested chromatin was transferred to new tubes. An aliquot was taken for reverse-crosslinking, DNA purification, and quantification to determine the amount of chromatin recovered. 15 ng of Drosophila chromatin (Active Motif, 53083) were added to each sample before taking an aliquot for input library preparation. The remaining chromatin (3-13 μg depending on sample) was used for immunoprecipitation with 0.8 μg anti-c-MYC antibody (Abcam, ab32072) following the SimpleChIP kit without modifications. Finally, libraries were prepared from reverse-cross linked IP and input DNA using the associated NEBNext Ultra II library preparation module. Libraries were sequenced to an average depth of 20-30 million paired-end read pairs using an Element AVITI in the 2×75 format.

UV-crosslinked RNA immunoprecipitation followed by RT-qPCR

RNA immunoprecipitation (RIP) was performed using the Magna RIP RNA-Binding Protein Immunoprecipitation Kit (MilliporeSigma, 17-700) according to the manufacturer's instructions, with UV crosslinking before cell lysis. Approximately 7×10^6 cells were collected

Please cite this article in press as: Shi et al., CRISPR mutagenesis of the *MYC* locus reveals a druggable ultraconserved RNA element, Cell (2027), https://doi.org/10.1016/j.cell.2026.10.002

by centrifugation, washed once with ice-cold PBS, and resuspended in 5 mL ice-cold PBS. Cells were transferred to an uncovered 10-cm dish, placed on ice, and irradiated with 254-nm UV light at 250 mJ/cm^2. Cells were collected immediately after irradiation.

Cell pellets were lysed in 700 μL complete RIP lysis buffer containing 700 μL RIP lysis buffer, 3.5 μL protease inhibitor cocktail, and 1.75 μL RNase inhibitor. Lysates were mixed by pipetting, incubated on ice for 5 min, and aliquoted. Lysates were clarified by centrifugation at 14,000 rpm for 10 min at 4°C.

For each immunoprecipitation, 50 μL protein A/G magnetic bead suspension was washed twice with 500 μL RIP wash buffer and resuspended in 100 μL RIP wash buffer. Beads were incubated with 5 μg anti-hnRNP L antibody or 5 μg species-matched control IgG for 30 min at room temperature with rotation. Antibody-bound beads were collected using a magnetic separator, washed twice with 500 μL RIP wash buffer, and resuspended in 900 μL RIP immunoprecipitation buffer containing 860 μL RIP wash buffer, 35 μL 0.5 M EDTA, and 5 μL RNase inhibitor.

Clarified lysate (100 μL) was added to each antibody-bound bead preparation, resulting in a final immunoprecipitation volume of 1 mL. Immunoprecipitation reactions were incubated overnight at 4°C with continuous rotation. Beads were subsequently collected using a magnetic separator and washed six times with 500 μL ice-cold RIP wash buffer.

For protein digestion, beads were resuspended in 150 μL proteinase K buffer containing 117 μL RIP wash buffer, 15 μL 10% SDS, and 18 μL proteinase K at 10 mg/mL. Input samples were supplemented with 107 μL RIP wash buffer, 15 μL 10% SDS, and 18 μL proteinase K to a final volume of 150 μL. Samples were incubated for 30 min at 55°C with shaking. Beads were collected magnetically, and the supernatants were transferred to new tubes and adjusted to 400 μL with 250 μL RIP wash buffer.

RNA was extracted by adding 400 μL phenol/chloroform/isoamyl alcohol (125:24:1), followed by vortexing for 15 s and centrifugation at 14,000 rpm for 10 min at room temperature. Approximately 350 μL of the aqueous phase was transferred to a new tube, mixed with 400 μL chloroform, vortexed for 15 s, and centrifuged at 14,000 rpm for 10 min at room temperature. Approximately 300 μL of the resulting aqueous phase was recovered.

RNA was precipitated by adding 50 μL Salt Solution I, 15 μL Salt Solution II, 5 μL precipitate enhancer, and 850 μL absolute ethanol. Samples were incubated at −80°C overnight and centrifuged at 14,000 rpm for 30 min at 4°C. RNA pellets were washed once with 1 mL 80% ethanol, centrifuged at 14,000 rpm for 15 min at 4°C, briefly air-dried, and resuspended in 11 μL RNase-free water.

The entire immunoprecipitated RNA sample was reverse transcribed using random hexamers and SuperScript reverse transcriptase. Quantitative PCR was performed using primers targeting the indicated MYC RNA regions. Enrichment was calculated relative to the corresponding species-matched IgG immunoprecipitation.

hnRNP L CLIP-qPCR

BrdU-CLIP was performed as described[138] with the following specifications. MDA-MB-231 and D11 cells (~5 × 10^6 per 10 cm plate) were UV-crosslinked at 400 mJ/cm2 (first dose) and then 200 mJ/cm^2 (second dose) in a Stratalinker 2400, lysed in 1× PXL buffer with cOmplete Protease Inhibitor Cocktail (Roche, 4693132001), and partially digested with RNase A (Thermo Fisher Scientific, EN0531) at 1:20,000 (mild) or 1:200 (over-digestion control) for 5 min at 37°C. Immunoprecipitation was performed with 100 μL Protein G Dynabeads (Thermo Fisher Scientific, 10004D) and 10 μg of anti-hnRNP L antibody (Santa Cruz, sc-32317). On-bead CIP treatment with Calf Intestinal Alkaline Phosphatase (Promega, M2825), 3′ linker ligation with pre-adenylated L32 DNA linker using T4 RNA Ligase 2 truncated KQ (NEB, M0373L) and RNasin Plus (Promega, N2611), T4 PNK (NEB, M0201L) ^{32}P labeling using [γ-^{32}P]-ATP (PerkinElmer, BLU502A), SDS-PAGE on 4–12% NuPAGE Bis-Tris gels (Invitrogen, NP0321BOX) in MOPS-SDS running buffer (Invitrogen, NP0001) with NuPAGE LDS Sample Buffer (Invitrogen, NP0007), and wet transfer to nitrocellulose membranes (Millipore Sigma, GE10600013) in NuPAGE Transfer Buffer (Invitrogen, NP0006) with 10% methanol were performed as described. Bands corresponding to 10–25 kDa above the predicted hnRNP L molecular weight were excised. RNA was released by Proteinase K (NEB, P8107S)/urea digestion, extracted with acid phenol (Sigma, P4682) and chloroform: isoamyl alcohol 49:1 (Sigma, 25668), precipitated with glycogen (Invitrogen, AM9510), and reverse transcribed with SuperScript III Reverse Transcriptase (Invitrogen, 18080093) in the presence of BrdUTP (Sigma, B0631) using barcoded RT primers. Following RNase H (Invitrogen, 18021071) treatment, free nucleotides were removed using MicroSpin G-25 columns (Cytiva, 27-5325-01). cDNA was purified by two rounds of anti-BrdU immunoprecipitation (Millipore Sigma, MAB3222) on Protein G Dynabeads pre-blocked with 50× Denhardt's solution (Millipore Sigma, D2532), circularized on-bead with CircLigase II ssDNA Ligase (Fisher Scientific, NC9869616), PCR-amplified with KAPA HiFi HotStart DNA Polymerase (Roche, KK2501) using real-time SYBR Green I (Invitrogen, S7563) monitoring (reactions terminated at RFU 250–500), purified with AMPure XP beads (Beckman Coulter, A63881; 1.8× v/v ratio).

Target-site qPCR was performed using a primer targeting the MYC RNA region surrounding the CA-rich element, paired with a universal library-adapter primer. Total amplifiable library was measured in parallel using universal library primers and used for normalization. For target-site qPCR, 30 pg library DNA was used per reaction. For universal-library qPCR, libraries were diluted 1:10,000 from the original library stock before amplification.

Digitonin-based RNA fractionation and RT-qPCR

Cells were treated with control ASO (ASO-ctrl) or MYC-targeting ASO (ASO-1) under the indicated conditions. All fractionation steps were performed on ice using pre-chilled buffers. Cells were washed twice with ice-cold PBS and incubated for 5 min with cytosol extraction buffer containing 110 mM KCl, 25 mM HEPES-KOH pH 7.4, 2.5 mM $MgCl_2$, 1 mM EGTA, 0.015% digitonin, 1 mM DTT, and RNase inhibitor. The released supernatant was collected as fraction 1 (F1). The remaining semi-intact cells were then washed

Please cite this article in press as: Shi et al., CRISPR mutagenesis of the *MYC* locus reveals a druggable ultraconserved RNA element, Cell (2027), https://doi.org/10.1016/j.cell.2026.10.002

for 1–2 min with low-digitonin wash buffer containing the same components except 0.004% digitonin, and the wash was collected as fraction 2 (F2). F1 and F2 were combined and analyzed as the soluble cytosolic RNA fraction.

After removal of the wash buffer, the remaining cell material was extracted for 5 min on ice with membrane extraction buffer containing 400 mM KCl, 25 mM HEPES-KOH pH 7.4, 15 mM $MgCl_2$, 1% NP-40, 0.1% sodium deoxycholate, 1 mM DTT, and RNase inhibitor. Cells were gently scraped, and the lysate was collected as the membrane/perinuclear-associated fraction. Cytosolic and membrane-associated fractions were clarified by centrifugation at 1,000 × g for 5 min at 4°C and 7,500 × g for 5 min at 4°C, respectively. Cleared supernatants were immediately mixed with three volumes of TRIzol LS reagent.

RNA was purified from TRIzol LS lysates using the Direct-zol RNA Miniprep kit (Zymo Research, R2052) according to the manufacturer's protocol. Briefly, one volume of ethanol was added to each TRIzol LS lysate, and samples were loaded onto Direct-zol columns in sequential loading steps. On-column DNase I treatment was performed using the DNase I supplied with the kit. Columns were washed according to the manufacturer's instructions, and RNA was eluted in RNase-free water. cDNA was synthesized using random primers, and RT-qPCR was performed using gene-specific primers. *MYC* mRNA abundance in the cytosolic fraction was normalized to *ACTB*, whereas *MYC* mRNA abundance in the membrane/perinuclear-associated fraction was normalized to *HSP90B1*.

ASO transfection in patient-derived organoid

HSC10 organoids were dissociated into single-cell suspensions using TrypLE Express (Gibco, 12604013) for 10 min at 37°C. Cells were resuspended in Matrigel (Corning, 356231) at a density of 2×10^4 cells per 50 μL and plated in a 24-well plate. The plate was inverted and incubated at 37°C for 30 min to allow Matrigel polymerization. After polymerization, 500 μL pre-warmed organoid culture medium was added. For sustained ASO treatment, organoids were treated every 3 days with ASO at a final concentration of 1 μM using 3 μL RNAiMAX per well. Bright-field images were acquired using a Leica DMi8 inverted microscope at 9 days post-culture. Organoids were defined as structures with a clearly delineated boundary and a diameter greater than 30 μm. Organoid numbers and diameters were quantified using ImageJ software.

EACorg000 organoids were dissociated into single-cell suspensions using TrypLE Express (Gibco) for 10 min at 37°C. Cells were then incubated with ASO-Lipofectamine RNAiMAX (Thermo Fisher Scientific) complexes for 6 h, prepared according to the manufacturer's instructions, at a final ASO concentration of 200 nM. Following transfection, the medium was removed, cells were resuspended in Matrigel at a density of 2×10^4 cells per 50 μL. The cell-Matrigel mixture was plated in 24-well plates (50 μL per well) and allowed to polymerize by incubating the inverted plate at 37°C for 30 min. After polymerization, 500 μL pre-warmed EAC culture medium was added. For sustained ASO treatment, organoids were re-treated every 3 days with ASO at a final concentration of 1 μM using 3 μL RNAiMAX per well. Bright-field images were acquired using a Leica DMi8 inverted microscope at 10 days post-culture. Organoids were defined as structures with a clearly delineated boundary and a diameter greater than 30 μm. Organoid numbers were quantified using ImageJ software.

QUANTIFICATION AND STATISTICAL ANALYSIS

sgRNA phenotype score calculation

The number of reads per sgRNA was computed with MAGeCK[47] (version 0.5.9.5) *count* subcommand and normalized with negative control sgRNAs (i.e. targeting AAVS1, non-targeting, or random). sgRNA-level log2 fold change for each sample was computed with MAGeCK's *test* subcommand using normalized count as input with parameters *–norm-method none –adjust-method fdr –control-gene control_gene_list.txt*. Day 8 and day 20 samples were compared to day 0 to calculate log2 fold changes. The two day 0 samples generated using high- and low-MOI infections produced highly similar results. We therefore used the high-MOI day 0 sample for all subsequent analyses, as higher MOI is expected to better preserve library complexity. Log2 fold change was further normalized for each sample by the number of days in culture to allow comparison. sgRNA-level phenotype score was calculated as the average of sgRNA-level per day log2 fold change across four samples.

Base-pair phenotype score calculation

To mitigate phenotype-independent variations across sgRNAs, base-pair-level log2 fold change was calculated by averaging the sgRNA-level log2 fold change of the eight sgRNAs (four per strand) predicted to cut within ±1 bp of each base pair. We leveraged MAGeCK gene-level summarization to achieve this. First, a pseudo MAGeCK count table was generated from normalized sgRNA count table with a customized script so that each sgRNA was duplicated four times and each duplicate's "Gene" column was mapped to a base pair coordinate within ±1 bp of its cutting site. Next, base-pair-level log2 fold change was computed with MAGeCK test subcommand using pseudo count table as input and high MOI day 0 sample as baseline with parameters –norm-method none –gene-test-fdr-threshold 0.01 –adjust-method fdr –gene-lfc-method mean –sort-criteria neg –control-sgrna control_sgrna_list.txt. With the modified pseudo count table, base-pair-level log2 fold change as the average of eight sgRNAs would be outputted as gene-level log2 fold change by MAGeCK test. One advantage of leveraging MAGeCK is that it uses robust ranking aggregation (RRA) algorithm to identify significantly regulated genes (base pairs in our scenario) by comparing the skew in sgRNA rankings of a gene to the uniform null model and prioritizing genes whose sgRNA rankings are consistently higher than expected. In our case, base pairs whose eight sgRNAs are consistently showing stronger phenotypes than negative control sgRNAs would be prioritized.

Please cite this article in press as: Shi et al., CRISPR mutagenesis of the *MYC* locus reveals a druggable ultraconserved RNA element, Cell (2027), https://doi.org/10.1016/j.cell.2026.10.002

Base-pair-level log2 fold change was further normalized for each sample by the number of days in culture to allow comparison. Base-pair-level phenotype score was calculated as the average base-pair-level per day log2 fold change across four samples. The median score of control sgRNAs with no off-targets in human genome when allowing at most one mismatch (474 control sgRNAs), which were randomly grouped for 1000 iterations with eight sgRNAs in a group to match base-pair-level averaging strategy, was subtracted from base-pair-level phenotype scores. A base pair was considered significant if it showed an FDR < 0.05 in at least two samples with at least two strong sgRNAs in each and exhibited a consistent log2 fold change directional trend in the remaining samples. Only 13 out of 22,058 MYC locus targeting sgRNAs and no negative control sgRNAs have low sequencing coverage in baseline sample (raw read count lower than 100). They were not removed given their low proportion in the entire sgRNA library and that their effects were mitigated as the base-pair-level phenotype score was calculated as the average of eight sgRNAs. Base pairs within the GFP region were not considered when calculating the base-pair phenotype score.

Gene and feature annotations

Human reference genome assembly hg38 was used throughout all analyses, except for the analysis presented in Figure S17B, which used hg19. *MYC* transcript ENST00000377970.6 was used throughout all analyses since it is the main *MYC* isoform expressed in the D11 screening cell line as shown by D11 RNA-Seq data. The possible mutation outcomes of a given base pair were predicted by Variant Effect Predictor (Ensembl version 112)[124] using ENST00000377970.6 as the reference *MYC* transcript. Since the category (i.e. coding, UTRs, etc.) of mutation outcomes in mutagenesis screening largely depends on the position of the cutting site instead of the exact indels, which are unknown at each position, it was assumed that an A was inserted for every cutting site when submitting to Variant Effect Predictor. Base pairs were further categorized into ''upstream_flanking'', ''5′ UTR", ''intron'', ''intron_splice'', ''coding'', ''3′ UTR'', and ''downstream_flanking'' based on their most damaging mutation outcomes (e.g. base pairs around splice sites were categorized as ''intron_splice'' instead of ''intron'', unless otherwise specified. Variant Effect Predictor defines variant within 1-8 bases at the 5′ end of an intron or 1-17 bases at the 3′ end of an intron as splice variant). Base pairs within 1-kb region upstream of the transcription start site of transcript ENST00000377970.6 were further categorized as ''promoter'' unless otherwise specified. Repeat annotation was retrieved from RepeatMasker.[139] A sgRNA was considered to fall within repeat regions if the 20-nt sgRNA entirely overlapped with repeats regardless of the strand. A base pair would be labeled as repeats if it was within repeat regions regardless of the strand. All base pairs within repeats were labeled or removed in analyses unless otherwise noted. ENCODE3 candidate cis-regulatory elements (cCREs) annotation combined from all cell types[56] were downloaded from UCSC Genome Browser. Base pairs were categorized into falling within elements with promoter-like signature (prom), proximal enhancer-like signature (enhP), distal enhancer-like signature (enhD), or no cCRE signature.

Off-target and target efficiency prediction

Potential off-targets of sg723 were searched by CasOFFinder[68] web server with parameters PAM type ''SpRY Cas9 from Streptococcus pyogenes: 5′-NNN-3′'' and target genome ''Homo sapiens (GRCh38/hg38)''. Off-target sites with mismatch numbers no more than two and no DNA bulges or RNA bulges were further mapped to genes according to GENCODE human release 47 annotations. Off-target indels at these sites were experimentally measured by amplicon sequencing using cells expressing corresponding sgRNA. Potential off-targets of all *MYC*-targeting and negative control sgRNAs were searched by mapping sgRNA sequences to human genome GRCh38.p14 with bowtie[125] (version 1.2.3) allowing one mismatch (-v 1 -all). Bam outputs from bowtie were processed with pysam (version 0.21.0) to obtain sgRNA-level off-target counts. Off-target predictions allowing two or three mismatches were done in a similar way using bowtie.

On-target efficiency of sgRNA was predicted with CRISPROn[52] (version 1.0), DeepSpCas9,[51] and CRISPick.[50] Given the PAM motif constraints of all three prediction tools, only sgRNAs with NGG PAM motif were considered for on-target efficiency prediction. To ensure that the observed growth phenotype differences reflected on-target efficiency rather than variation in sgRNA target regions, only sgRNAs with NGG PAM motif and targeting at the coding region in exon 2 were considered in the comparison between predicted on-target efficiency and sgRNA phenotype score.

Potential off-targets of ASOs were identified using RNAhybrid[70] with parameters *-u 5 -v 5*, scanning all human exons, including ±200 nucleotide flanking sequences, based on GENCODE human release 47.

Conservation-function correlation

Whole-genome phastCons scores[140] derived from multiple alignments of 99 vertebrate genomes to the human genome were downloaded from UCSC Genome Browser. Coding regions on the whole genome level were defined as CDS regions of MANE Select transcripts[141] (MANE release 1.4). *MYC* coding regions were specifically defined as the coding regions in transcript ENST00000377970.6. Per-base-pair JARVIS[64] score on 10-kb *MYC* locus in hg38 was downloaded from UCSC Genome Browser. UK Biobank depletion rank score with 500-bp window size and a 50-bp step size was downloaded from Halldorsson et al.[63] GC content for 5-bp window was downloaded from UCSC Genome Browser. To match the averaging strategy of the base-pair phenotype score, per-base-pair phastCons scores were smoothed using a 5-bp sliding window, in which the score at each base pair was replaced by the average of scores within ±2 bp of that position. JARVIS scores were smoothed in the same way. Base-pair phenotype scores were averaged within each 500-bp window when compared with UK Biobank depletion rank score to match the window size. 500-bp windows with more than 100 repeat base-pairs or containing any CDS base-pairs were removed. A 500-bp window was

Please cite this article in press as: Shi et al., CRISPR mutagenesis of the *MYC* locus reveals a druggable ultraconserved RNA element, Cell (2027), https://doi.org/10.1016/j.cell.2026.10.002

considered significant if it contained a higher proportion of significant base-pairs than the non-repeat background (i.e. at least 19 significant base-pairs within a 500-bp window). Unsmoothed per-base-pair phastCons scores and base-pair phenotype scores were averaged within each 5-bp window when compared with GC content to match the window size. Average sgRNA on-target score of a base-pair was calculated as the mean efficiency predicted by CRISPRon for all sgRNAs with NGG PAM motif and cutting within two base-pairs of the base-pair of interest. Base-pairs without any sgRNAs available for CRISPRon prediction were removed in conservation-sgRNA-efficiency analysis. *RPS19* SpRY-mediated screening data was retrieved from Tables S2 and S3 in Yao et al.[19] Two supplementary tables were merged together, and average log2(CRISPR score)2 as provided in tables was taken as phenotype score. Since the provided CRISPR score was calculated by averaging the sgRNA scores of five consecutive sgRNAs centered at the indicated sgRNA, *RPS19* phastCons scores were smoothed in the same manner as *MYC* phastCons scores.

3′ UTR conservation and mRNA half-life

The aggregated half-life data of human genes were downloaded from Agarwal and Kelley.[142] 3′ UTR coordinates of MANE Select protein-coding transcripts were retrieved from UCSC Genome Browser Table Browser (MANE release 1.4). Whole-genome per-base-pair phyloP[143] score for multiple alignments of 99 vertebrate genomes to the human genome was downloaded from UCSC Genome Browser. Highly conserved base pairs in 3′ UTR were defined with the method from Luo et al.[80] A base pair was considered highly conserved if its phyloP score is no less than 2 and at least four consecutive base pairs had phyloP scores above this cutoff.

Visualization with UCSC Genome Browser

Screening signal along *MYC* locus was visualized using customized plotting scripts in combination with UCSC Genome Browser.[144] Standard tracks were provided directly by UCSC Genome Browser, including GENCODE v49 annotation, phastCons conservation score, GC percent in 5-base windows, DNase signals, ENCODE3 candidate cis-regulatory elements (cCREs) annotation, JARVIS score, and UK Biobank Depletion Rank score (DR). RNA-Seq coverage track was generated from the screening cell line D11 RNA-Seq data (method specified in RNA-Seq analysis).

Covariation

The multiple sequence alignment of 100 vertebrate genome was downloaded from UCSC Genome Browser. We excluded 18 species that have large deletions or poor alignments in the hairpin region (lizard, megabat, and 16 fish genomes): chr8:127,741,056-127,741,087.

RNA-seq analysis

For RNA-Seq data of ASOs treated samples, RNA-Seq fastq files were processed with fastp[126] (version 0.23.2) using default parameters to filter out low-quality reads, trim low-quality bases and remove adapters if needed. Reads were mapped to genome assembly hg38 (GRCh38.p14) with STAR[127] (version 2.7.10b) using parameter –outFilterMultimapNmax 1 (unique mappers only). Reads were quantified with featureCounts[128] (version 2.0.1) using parameters -s 2 -p and GENCODE human release 47 annotations. Transcripts Per Million (TPM) was calculated for each gene based on the raw count table and gene length. Coverage track was generated from mapping bam files with deepTools[129] bamCoverage (version 3.5.4) using parameters –binSize 5 –normalizeUsing None –centerReads. Differential expression analysis was carried out with DESeq2 (version 1.46.0).[72] Samples 48-hour and 72-hour post ASO treatment were compared to control samples of corresponding time points. Genes were ranked according to DESeq2 "stat" column output and gene set enrichment analysis (GSEA) was carried out with clusterProfiler (version 4.14.6).[130] Gene sets were retrieved from the Molecular Signatures Database (MSigDB).

RNA-Seq data of siHNRNPL and control siRNA (siCtrl) treated samples, siMYC and control siRNA treated samples were processed by the Plasmidsaurus RNA-seq analysis pipeline.

ChIP-seq analysis

Read pairs were adaptor trimmed and aligned to combined human and Drosophila genome (GRCh38 + GCF_000001215.4_Release_6_plus_ISO1_MT_genomic) using bwa mem (version 0.7.19-r1273),[131] with seed size (-k) of 17. Bam files were deduplicated and filtered with samtools to retain properly-paired read pairs with MAPQ $\geq$30. Because the proportion of Drosophila-derived reads varied across samples and remained very low after alignment and filtering (< 0.5%), spike-in Drosophila reads were discarded in the downstream analysis. Reads overlapping with ENCODE hg38 blacklist regions[145] were removed from bam files. To avoid sequencing depth bias in the downstream pooled peak calling, bam files were down-sampled to the smallest library depth for IP and input samples respectively. Peaks were first called at condition-level using MACS3[132] callpeak (–format BAMPE –qvalue 0.05), by using the down-sampled IP and input bams of both replicates for each condition. Down-sampled IP bam files for two replicates of the same condition were merged together. Bigwigs were generated from merged IP bam files with deepTools bamCoverage (–normalizeUsing CPM). Metagene plots were generated with deepTools computeMatrix and plotProfile, using reference-point mode with the center of peaks called in control condition in each cell line. Next, peaks were called with MACS3 callpeak (–format BAMPE –pvalue 0.05) using all down-sampled IP and input bam files to generate a union set of peaks across all samples. Statistical threshold in peak calling was set to be permissive to retain more differential binding events. Original IP bam files for each sample (without down-sampling) were converted to positionally-deduplicated fragment bed files with bedtools bamtobed. Peaks were quantified within sample

by counting the number of overlapping (>5bp) fragments for each IP with each peak in the union peak set. Peak count table was read into R for differential binding analysis. Normalization factors were calculated using the trimmed mean of M-values (TMM) method[74] on binned counts generated from the original IP bam files as stated by csaw. This method removes composition biases by assuming that most large genomic bins represent non-differential-binding background regions and systematic differences at high abundances represent genuine differential binding events. This background-based normalization is therefore able to pick up systematic binding differences between conditions even without spike-in data. Downstream peak-level differential binding analysis was carried out with edgeR[133] using the normalization factors and library sizes calculated by csaw. Peaks with total fragment count fewer than 15 were discarded in differential binding analysis.

Statistics and reproducibility

In general, all experiments were performed with at least three independent biological replicates, except for the HF1-SpRY-Cas9 screen and ChIP-seq experiments. The screen was performed twice starting from independent HF1-SpRY-Cas9 stable cell line generations, and ChIP-seq used two replicates per condition. Statistical analyses were conducted using GraphPad Prism software (version 10.4), except where specific statistical methods are indicated in the figure legends or described above. Comparisons between two groups were analyzed using a two-tailed Student's t-test, while one-way ANOVA was used for comparisons involving more than two groups. Representative data were derived from at least three independent replicates, except where otherwise specified. Data are presented as mean ± standard deviation (SD). Statistical significance is indicated as follows: ns: not significant, *: $P < 0.05$, **: $P < 0.01$, ***: $P < 0.001$, ****: $P < 0.0001$.